学位論文

Simulation studies of bilayer membranes: morphological changes induced by chemical reactions and pressure profile calculation method

(数値シミュレーションによる二重膜の研究: 化学反応下での形態変化と圧力分布計算手法)

平成２９年１２月博士（理学）申請

東京大学大学院理学系研究科
物理学専攻
中川　恒

Abstract

A bilayer membrane is a fundamental component of living cells. It has been extensively studied from the perspective of not only biology but also soft matter physics. Due to the soft nature of the bilayer membranes, they exhibit various shape transformations by external stimuli. These shape transformations are well described in the theory of elasticity, and to examine the mechanical properties of the bilayer membrane is essential. In this dissertation, we focus on the two aspects of bilayer membranes: morphologies and mechanical properties. Specifically, we examined morphological changes induced by chemical reactions and pressure profile within the bilayer membrane.

First, we investigated shape transformations of bilayer membranes induced by hydrolysis and condensation reactions of amphiphilic molecules using coarse-grained molecular simulations. Asymmetric chemical conditions between inside and outside the vesicles are widely observed both *in vitro* and *in vivo*. Thus, we investigate the shape transformations of vesicles under such an asymmetric chemical condition. The asymmetric chemical condition causes the asymmetric chemical reactions between the inner and outer leaflets of a vesicle, leading to the transport of amphiphilic molecules between two leaflets. It is found that the resulting area difference between the two leaflets induces the two types of shape transformations: bilayer sheet protrusion (BP) and budding. Both BP and budding occurs at low reduced volume, whereas only BP occurs at high reduced volume. The probabilities of these two types of transformations depend on the shear viscosity of the surrounding fluids compared to the membrane as well as the reaction rates. A higher surrounding fluid viscosity leads to more BP formation. The inhomogeneous spatial distribution of the hydrophobic reaction products embedded in the bilayer forms the nuclei of BP formation in the bilayer, and faster diffusion of the products enhances BP formation.

Next, we studied the pressure profile calculation method in molecular simulations. The pressure profile within the bilayer membrane has been calculated for understanding the mechanical properties of the bilayer membrane in molecular simulations. We point out the severe problem of conventional methods regarding the force decomposition from multibody forces to pairwise forces. The conventional method to calculate the stress fields containing the multibody forces is based on the central force decomposition, in which the multibody forces are decomposed into the pairwise forces, and Irving-Kirkwood-Noll procedure is applied to these decomposed pairwise forces. We introduce a force center of a three-body potential and propose different force decompositions that also satisfy the conservation of translational and angular momentum. The position of force center can be arbitrarily chosen, and the change of force center position modifies the force decomposition. Thus, we need to select physically plausible force center position. We propose a candidate criterion, stress-distribution magnitude (SDM) and compare the force decompositions by the SDM. We discuss their difference in the stress profile of a bilayer membrane by using coarse-grained and atomistic molecular dynamics simulations.

List of Abbreviations

ADE	Area difference elasticity
BP	Bilayer protrusion
CFD	Central-force decomposition
CG	Coarse-grained
DPD	Dissipative particle dynamics
EO	Embedded oil
ER	Endoplasmic reticulum
FCD	Force-center decomposition
GLD	Goetz-Lipowsky decomposition
HD	Hybrid decomposition
HS	Hydrophilic solute
IKN	Irving-Kirkwood-Noll
MD	Molecular dynamics
SDM	Stress distribution magnitude
SIMD	Single instruction multiple data

List of Symbols

a^*	Dimensionless quantity of a
a_{ij}	Repulsive strength between ith and jth particles
A_{mb}	Area of a bilayer membrane
α_{sp}	Asphericity
c_{in} (c_{out})	Concentration of hydrophilic solute of inside (outside) a vesicle
D_{EO}	Diffusion constant of embedded oil
δd	Standard deviation of bilayer thickness
Δc	Concentration difference of hydrophilic solute between inside and outside a vesicle
δn_{EO}	Surface density inhomogeneity of embedded oils
Δt	Simulation time step for conservative forces
δt	Simulation time step for dissipative and random forces
η_{mb} (η_{sol})	Shear viscosity of membrane (solvent)
Γ	Surface tension of a bilayer membrane
Γ_{in} (Γ_{out})	Surface tension of an inner (an outer) leaflet
Γ_{SDM}	Stress distribution magnitude
γ_{ij}	Dissipative strength between ith and jth particles
K_A	Area expansion modulus of a bilayer membrane
k_{bond}	Harmonic bond strength for adjacent particles
κ	Bending rigidity
$\bar{\kappa}$	Gaussian curvature modulus
k_{bend}	Chain stiffness for adjacent bonds
$k_{\mathrm{B}}T$	Thermal energy
l_0	Equilibrium length of a bond
$\boldsymbol{\sigma}(\mathbf{x})$	Local stress tensor at position $\mathbf{x}$
L_x, L_y, L_z	Simulation box side lengths
m	Mass of a particle
h	Membrane height
$h_{\max}$	Maximum membrane height

N_{amp}	Number of amphiphiles
$N_{\mathrm{amp,out}}$ ($N_{\mathrm{amp,in}}$)	Number of amphiphiles in an outer (an inner) leaflet of a bilayer membrane
$N_{\mathrm{amp,up}}$ ($N_{\mathrm{amp,low}}$)	Number of amphiphiles in an upper (a lower) leaflet of a bilayer membrane
N_{BP}	Number of bilayer protrusions
N_{EO}	Number of embedded oils
$N_{\mathrm{sol,in}}$ ($N_{\mathrm{sol,out}}$)	Number of solvent particles inside (outside) a vesicle
ρ	Number density
ΔN_{amp}	Number difference of amphiphiles between outer and inner leaflets
$\mathbf{r}_{c0}$	Original force center
p_{bind}	Transition probability of bond binding
p_{diss}	Transition probability of bond dissociation
p_{f}	Transition rate of bond dissociation
$P_{\mathrm{L}}(z)$ ($P_{\mathrm{N}}(z)$)	Lateral (Normal) component of pressure at z
p_{r}	Transition rate of bond binding
U	Potential energy
$\mathbf{r}_c$	Force center
r_{cut}	Potential cutoff length
$\mathbf{r}_i$	Position of ith particle
R_{ves}	Radius of a vesicle
T	System temperature
τ	Unit of time
Θ	Unit step function
U_{rep}	Repulsive potential
V	Simulation box volume
v	Reduced volume of a vesicle
$\mathbf{v}_i$	Velocity of ith particle
V_{ves}	Vesicle volume
$w(r_{ij})$	Weighting function of dissipative and random forces
ξ_{ij}	Gaussian white noise

Contents

Chapter 1

Introduction

1.1 Background

1.1.1 Bilayer membrane

A biomembrane is a fundamental component of a living cell. Its primary function is the boundary between two regions, but the biomembrane is not a simple wall. It also acts as the transporter of several ions and sensor of external stimuli [10]. The biomembrane consists of several membrane proteins and lipids as schematically shown in Fig. 1.1. Although the composition ratio of these biomolecules depends on the organs [81], the main component is the lipid in many organs. The lipid is loosely defined as the biomolecule that is not dissolved in water but dissolved in organic solvents such as benzene. Typically, the lipid has two segments: hydrophilic and hydrophobic segments. To avoid the contact with water molecules, the lipids in water self-assemble and form clusters such as micelle and bilayer sheet depending on the packing parameter [50]. The membrane composed of only lipids (more generally amphiphilic molecules) is referred to as the bilayer membrane, and the closed bilayer membrane is referred to as the vesicle.

The vesicles have been examined as a simple model of the biomembrane [93]. Although its composition is simple, they exhibit various shape transformations. Figure 1.2 shows an example of shape transformations: shape transformations by the constant osmotic pressure difference [124]. The decrease of the volume of vesicle by the osmotic pressure difference induces the various shape transformations from a spherical shape. The biconcave shape, which is a typical shape of red blood cell, is also found for the simple vesicle.

Helfrich theory can describe the various shape transformations of vesicles observed in the experiments [39]. In Helfrich theory, the bilayer membrane is treated as the thin elastic sheet (this is justified by the large-scale gap between the radius of vesicle and bilayer thickness). The free energy of the bilayer membrane is

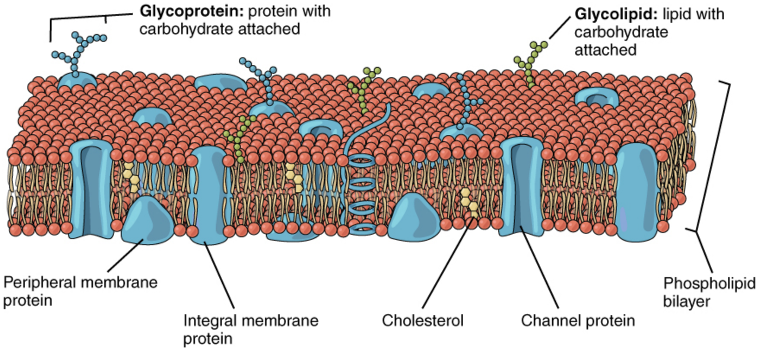

Fig. 1.1: Schematic picture of a biomembrane. The figure is adapted from [1].

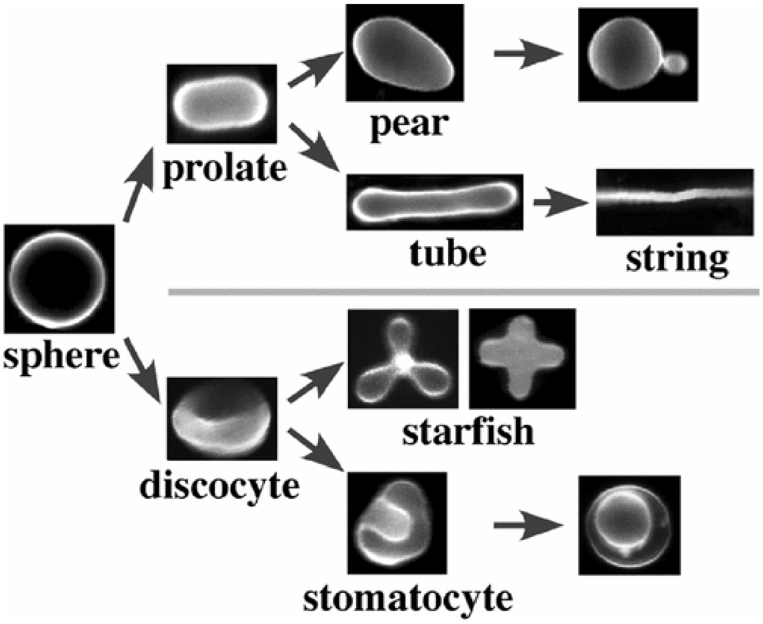

Fig. 1.2: Various shape transformations of vesicles by the constant osmotic pressure difference. The figure is adapted from Fig. 1 in [124]

written as

$$F_{\mathrm{cv}} = \oint \frac{\kappa}{2}(2H - c_0)^2 dA + \oint \bar{\kappa} K_{\mathrm{G}} dA, \tag{1.1}$$

where κ, $\bar{\kappa}$, H, K_{G}, and c_0 are the bending rigidity, Gaussian curvature modulus, mean curvature, Gaussian curvature, and spontaneous curvature of the membrane, respectively. The integral in Eq. (1.1) is performed on the membrane surface. The predicted shapes, which are obtained by the minimization problem of Eq. (1.1), agree well with experimental observations. However, pear, peal-neckless, and branched starfish-like shapes were also found in the experiments [44, 59, 93]; these shapes are not obtained by the minimization problem of Eq. (1.1). As an extension of Helfrich theory, area difference elasticity (ADE) model was proposed [93, 125]. In ADE model, the spontaneous curvature caused by the mismatch between the geometric area difference ΔA and intrinsic area difference ΔA_0 is considered. ΔA and ΔA_0 are defined as

$$\Delta A = d_{\mathrm{neut}} \oint 2H dA, \tag{1.2}$$

$$\Delta A_0 = (N_{\mathrm{amp,out}} - N_{\mathrm{amp,in}}) a_0, \tag{1.3}$$

where, $N_{\mathrm{amp,out}}$ and $N_{\mathrm{amp,in}}$ represent the number of amphiphilic molecules in the outer and inner leaflets, respectively. d_{neut} is the distance between inner and outer leaflets, and a_0 is an area per amphiphilic molecule. The free energy caused by the mismatch ΔA and ΔA_0 is written as

$$F_{\mathrm{ADE}} = \frac{\pi k_{\mathrm{ADE}}}{2A_{\mathrm{mb}} d_{\mathrm{neut}}^2} (\Delta A - \Delta A_0)^2, \tag{1.4}$$

where k_{ADE} is the elastic constant of ADE, and A_{mb} is the area of the bilayer membrane. The total free energy of bilayer membrane is $F = F_{\mathrm{cv}} + F_{\mathrm{ADE}}$. The theoretical predictions by ADE model agree well with experimental observations quantitatively [91].

1.1.2 Molecular simulations of bilayer membranes

The elastic theory described in the previous section is suitable for investigating the shape transformations of vesicles on μm scale. However, for investigating more microscopic length scale phenomena, in which the effect of thermal fluctuation plays an important role, molecular simulation is a suitable tool [67, 73, 120]. In this method, amphiphilic molecules are modeled by atomistic or coarse-grained (CG) molecules (see Fig. 1.3); the particles, which represent the atoms or blobs of several atoms, are moved based on Newton's equations of motion. When using the atomistic model of lipid molecules, nm length scale motion of lipid molecules can be examined during ∼100 ns.

The use of CG models broadens the accessible length and time scale compared with the atomistic model. The CG models are roughly classified into two types: implicit and explicit solvent model. In the implicit solvent model, we integrate only the motion of lipid molecules. The hydrophobic interaction is taken into account phenomenologically using local density-dependent multibody potential [42, 78] or wide range attractive potential [17, 18]. The implicit solvent models are widely used to examine the fusion pathway of lipid vesicles [77], phase separation dynamics of two-component lipid vesicles [18], and self-assembly process of lipid molecules [78]. In the explicit solvent model [32, 34, 98], we integrate both solvents and lipid molecules. The accessible length and time scale decreases compared with the implicit solvent models, but the explicit models are suitable for investigating the effect of hydrodynamic interactions [29, 102].

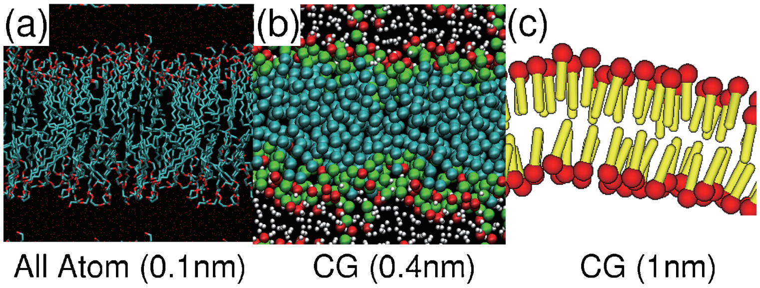

Fig. 1.3: Snapshots of various types of membrane models. (a) Atomistic model. (b) Explicit solvent coarse-grained model. (c) Implicit solvent coarse-grained model. The image is adapted from Fig. 1 in [73].

In this dissertation, we use both atomistic and explicit solvent CG bilayer membrane models. In the explicit solvent CG bilayer membrane model, we employed the dissipative particle dynamics (DPD) simulation technique, which is widely used in the simulations of bilayer membranes. Since we use the DPD method in the studies of both Chapter 3 and Chapter 4, we explain the details of the DPD simulation in Chapter 2.

1.2 Overview of the dissertation

In this dissertation, we show two independent studies regarding the bilayer membranes:

- Shape transformations of the bilayer membranes induced by the hydrolysis and condensation reactions (in Chapter 3).

- Pressure profile calculation method in molecular simulations (in Chapter 4).

We briefly overview these two contents in the following.

1.2.1 Shape transformations of the bilayer membranes induced by the hydrolysis and condensation reactions

Chemical reactions occur ubiquitously in the biological cells. For example, in the cells, the lipid molecules are synthesized and degraded by the chemical reactions such as condensation and hydrolysis reactions via several enzyme activities. These processes are called lipid metabolism; its main function is the storage of fats for energy. When the glucose level gets low, the triacylglycerols stored in fat droplets are hydrolyzed into fatty acids, which are used for the energy production in mitochondria [10].

The lipid molecules consisting of the biomembranes (*e.g.*, phospholipids) are synthesized in the ER (endoplasmic reticulum). Interestingly, the synthesis occurs only in the cytosolic leaflet of the ER membrane (see Fig. 1.4). Thus, the densities of phospholipids become asymmetric between the cytosolic leaflet and ER lumen leaflet by this synthesis of lipids [15]. Since the trans-bilayer diffusion of phospholipids, *i.e.*, the flip-flop is slow, the phospholipids newly synthesized in the cytosolic leaflet is transferred via phospholipid scramblase activities. Other lipids, such as cholesterol and ceramide are also synthesized in the ER membranes. The synthesized lipids are transported to other organelles via vesicle transport mechanisms.

Several *in vitro* experiments show that the synthesis and degradation of lipids induce the shape transformations of the membranes. For example, the experiments of hydrolase enzymes injection to lipid vesicles and red blood cells show the invagination [8,41] and rupture [88] of membranes. A possible explanation of these morphological changes was proposed in terms of elastic theory [8]. The effects of chemical reactions are taken into account by the change in the amphiphilic molecular densities of the inner and outer leaflets. However, other experiment reports that the hydrophobic reaction products of hydrolysis reaction, which are embedded in the bilayer, reduce the spontaneous curvature of the membrane leading to the continuous morphological changes from the micelles to vesicles [107, 114] (see Fig. 1.5). This experiment demonstrates that the effects of the chemical reactions on the morphological changes cannot be simply explained by the change in the amphiphilic molecular densities in terms of the elastic theory.

In Chapter 3, we discuss the shape transformations of the bilayer membranes induced by the hydrolysis and condensation reactions of amphiphilic molecules. We use CG simulation technique and investigate the shape transformations of the bilayer membranes and the effects of the reaction products on the membrane

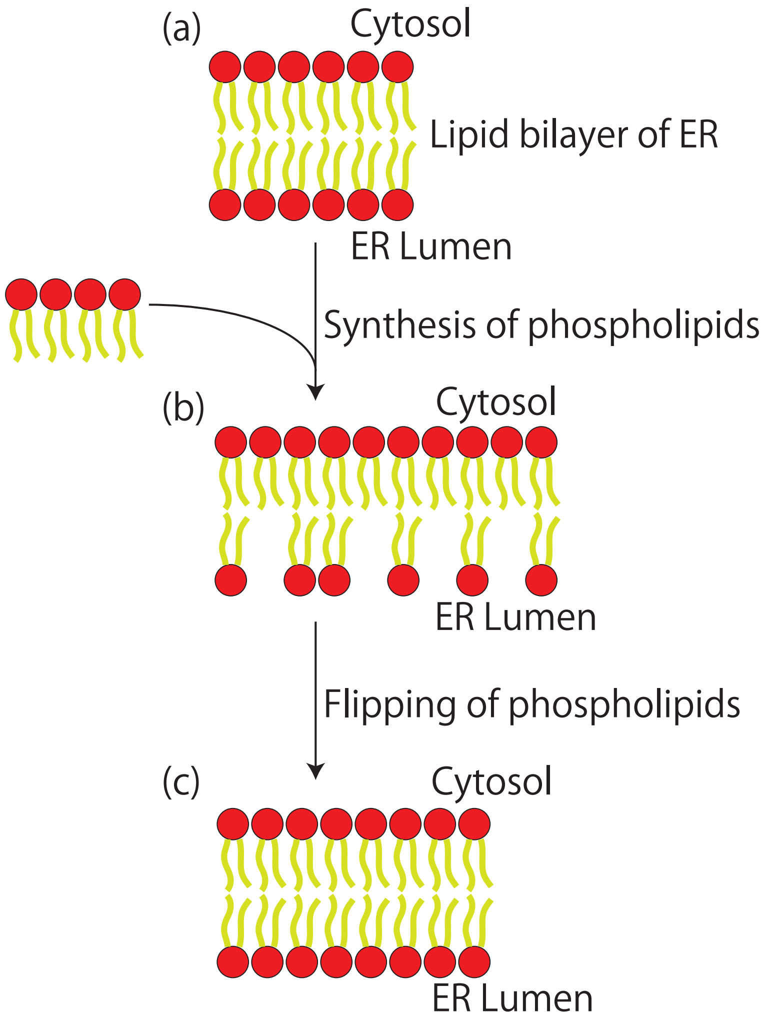

Fig. 1.4: The process of phospholipid synthesis in ER membrane. Phospholipids are synthesized on the cytosolic leaflet of the ER membrane (from (a) to (b)). Phospholipid scramblase causes the flipping of phospholipids (from (b) to (c)) to transfer newly synthesized phospholipids to the ER lumen leaflet.

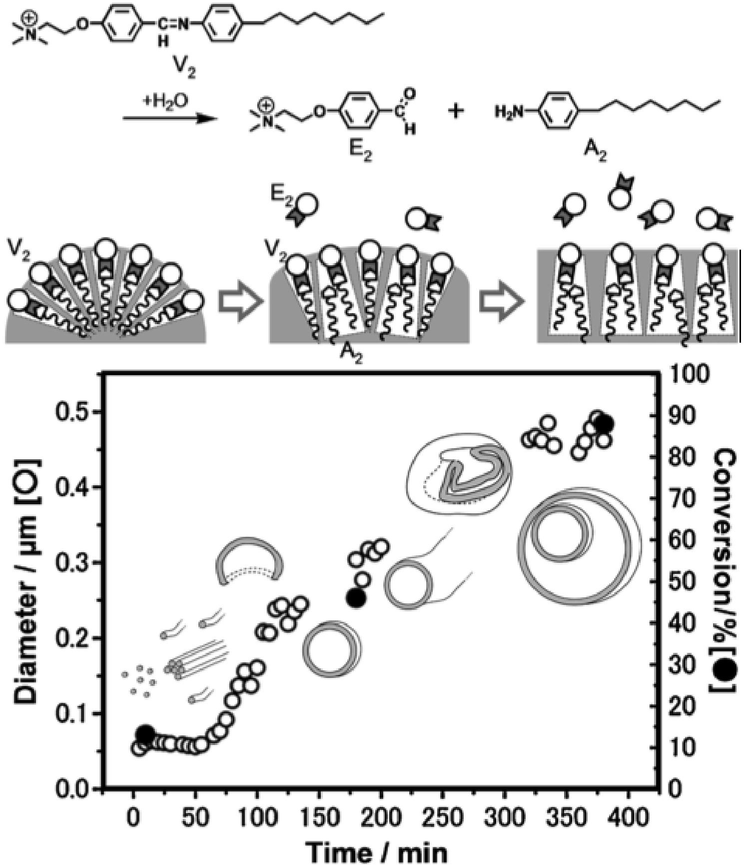

Fig. 1.5: Spontaneous morphological changes from spherical micelles to nested vesicles induced by the hydrolysis of amphiphilic molecules. The figure is adapted from Fig. 4 in [107].

morphologies.

1.2.2 Pressure profile calculation method in molecular simulations

In the elastic theory described in Sec. 1.1.1, the bilayers are treated as the thin elastic sheets; the internal bilayer structures are not considered. However, the real membranes have the finite thickness, which is ∼10 nm. When we regard the bilayer as the three-dimensional elastic object, we can define the pressure profile within the bilayer. Especially, the lateral component of the pressure within the bilayer has been discussed since Tanford proposed the two opposing forces concept [50]. Figure 1.6 shows the schematic picture of a bilayer membrane and lateral pressure profile within the bilayer. At the interface between the hydrophobic core and the water, the interfacial tension γ exerts to minimize the interfacial area due to the hydrophobic interaction. On the other hand, steric repulsion also exerts to expand the area at the hydrophobic core and the head-segment region. Therefore, the lateral pressure profile within the bilayer membrane is inhomogeneous as shown in the right panel of Fig. 1.6.

The balance between these two opposing forces, interfacial tension, and steric repulsion determines the area per amphiphilic molecule. The free energy per an amphiphile due to the interfacial tension is written as γa, where a is the area occupied by an amphiphile. The free energy term due to the steric repulsion is roughly estimated as C_A/a to first order. Thus the free energy per an amphiphile is written as

$$\mu = \gamma a + C_A/a. \tag{1.5}$$

The optimal area a_0 of an amphiphile is determined by the minimum of μ as $\sqrt{C_A/\gamma}$.

The lateral component P_{L} and normal component P_{N} of the pressure within the bilayer membrane give the two dimensional elastic properties of bilayer membrane. For example, the relationship between P_{L}, P_{N}, and $\bar{\kappa}$ is written as [40, 46, 90]

$$\bar{\kappa} = \int \left[P_{\mathrm{N}}(z) - P_{\mathrm{L}}(z)\right] z^2 dz. \tag{1.6}$$

$\bar{\kappa}$ is an important elastic property of the bilayer membrane; $\bar{\kappa}$ plays a key role in the shape transformation with topological changes, such as fusion and fission of vesicles [10] and bicelle to vesicle transformation [26, 45].

The attempts to capture the inhomogeneous pressure profile within the bilayer membrane and the estimation of $\bar{\kappa}$ via P_{N} and P_{L} have been carried out using molecular simulations [120] since the landmark paper by Goetz and Lipowsky [32].

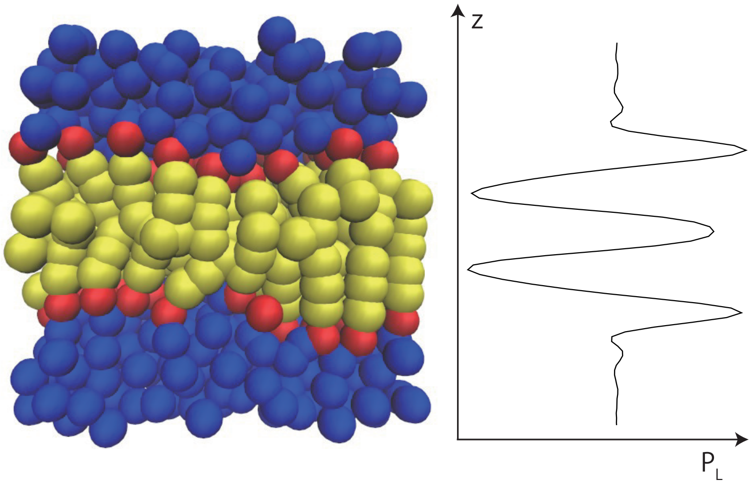

Fig. 1.6: Schematic picture of a lateral pressure profile of bilayer membrane. The left panel shows the simulation snapshot of CG bilayer membrane that is used in this dissertation. Water, hydrophilic, and hydrophobic particles are colored by blue, red, and yellow, respectively. The right panel shows the schematic representation of lateral pressure within the bilayer membrane. At the interface between the hydrophobic core and hydrophilic head region, a negative pressure is exerted due to the hydrophobic interaction leading to the decrease of the area per amphiphilic molecule. On the other hand, a positive pressure is exerted in the hydrophobic cores and head-segment region due to the steric repulsion and chain disorder.

The lateral pressure profile within the bilayer membrane qualitatively is similar to the theoretical prediction [32].

In the pressure profile calculation in molecular simulations, the Irving-Kirkwood-Noll (IKN) procedure is applied for the pairwise forces [49]. For the multibody forces, there are two steps to calculate the pressure profile: the decomposition of multibody forces to the pairwise forces and the application of IKN procedure to each decomposed pairwise forces. Conventionally, the force decomposition is performed using Goetz-Lipowsky decomposition (GLD) [32], which does not satisfy the strong law of action and reaction for decomposed pairwise forces. The central force decomposition (CFD) proposed by Admal and Tadmor overcomes this problem [6]. The calculations of the pressure profile within the bilayer membrane using CFD have been carried out [112, 118].

However, the pressure profile calculation method has been still debated for the systems containing multibody interactions. In Chapter 4, we revisit the force decomposition of the multibody forces to the pairwise forces. We discuss the nonuniqueness caused by the nonunique force decomposition from multibody forces to pairwise forces.

Chapter 2

Simulation techniques

In this chapter, we introduce the simulation techniques used throughout in this dissertation. First, we introduce the dissipative particle dynamics (DPD) simulation technique which is commonly used as a CG molecular simulation method. We introduce the basic concepts, discretizations, and choices of interaction parameters and describe the CG bilayer membrane model used in this dissertation.

Next, we introduce an acceleration technique of molecular simulations. Here we focus on a SIMD (single instruction multiple data) acceleration technique of molecular simulations. SIMD instructions are widely used to explore data-level parallelism in modern CPUs. For example, for x86 architecture, SSE (128-bit SIMD), AVX (256-bit SIMD), and AVX-512 (512-bit SIMD) are added as the SIMD instructions. Without the use of SIMD instructions, achievable performance decreases by 1/2–1/8. Therefore, the optimization with the use of SIMD instructions is crucial to maximizing the application performance. We first introduce the basic algorithms of molecular simulations then discuss the performance improvement of molecular simulations with the use of SIMD instructions.

2.1 Dissipative particle dynamics

2.1.1 Basic concepts

The dissipative particle dynamics (DPD) method is one of the meso-scale hydrodynamics simulation techniques. The DPD method was first proposed by Hoogerbrugge and Koelman [43] and has been used to investigate several soft matter systems such as polymers [106], colloids [54], and bilayer membranes [34]. In the DPD method, one particle is regarded as a blob of several atoms. The motion of this particle is given by the following Newton's equations of motions with a thermostat:

$$m\frac{d\mathbf{v}_i}{dt} = -\frac{\partial U}{\partial \mathbf{r}_i} + \sum_{j\neq i} \mathbf{f}_{\text{fd}}(\mathbf{v}_{ij}, \mathbf{r}_{ij}), \tag{2.1}$$

$$\mathbf{f}_{\text{fd}}(\mathbf{v}_{ij}, \mathbf{r}_{ij}) = \left(-w(r_{ij})\mathbf{v}_{ij} \cdot \hat{\mathbf{r}}_{ij} + \sqrt{w(r_{ij})}\xi_{ij}(t)\right)\hat{\mathbf{r}}_{ij},$$

$$w(r_{ij}) = \gamma_{ij}\left(1 - \frac{r_{ij}}{r_{\text{cut}}}\right)^p \Theta\left(1 - \frac{r_{ij}}{r_{\text{cut}}}\right), \tag{2.2}$$

where $\mathbf{v}_{ij} = \mathbf{v}_i - \mathbf{v}_j, \mathbf{r}_{ij} = \mathbf{r}_i - \mathbf{r}_j, r_{ij} = |\mathbf{r}_{ij}|, \hat{\mathbf{r}}_{ij} = \mathbf{r}_{ij}/r_{ij}$, and Θ is the unit step function. The Gaussian white noise $\xi_{ij}(t)$ in Eq. (2.1) satisfies the fluctuation and dissipation theorem, *i.e.*, $\langle \xi_{ij}(t) \rangle = 0, \langle \xi_{ij}(t)\xi_{kl}(t')\rangle = 2k_{\text{B}}T(\delta_{ik}\delta_{jl} + \delta_{il}\delta_{jk})\delta(t - t')$, where $k_{\text{B}}T$ is the thermal energy. The exponent p of weighting function $w(r_{ij})$ is typically set to 2 [35]. Since one DPD particle represents the blob of several atoms, the position overlap between particles is permitted. A harmonic potential

$$U_{\text{rep}}(r_{ij}) = a_{ij}(1 - r_{ij}/r_{\text{cut}})^2/2, \tag{2.3}$$

which vanishes at finite cutoff r_{cut} is used as the repulsive potential between particles. The cutoff length r_{cut} has the same value for any particle pair.

Typically, three types of DPD particles are considered in a bilayer membrane model: water, hydrophilic, and hydrophobic particle. Three water molecules are treated as one DPD particle [35]. Coarse-grained amphiphilic molecule is modeled as several DPD particles that are connected via bonded potentials such as harmonic bond U_{bond} and bend potentials U_{bend} [30, 101]. In this dissertation, an amphiphilic molecule consists of hydrophilic head and hydrophobic tail segments that are represented by one and three particles, respectively (see Fig. 2.1). These four particles are connected via the bond potential $U_{\text{bond}} = (k_{\text{bond}}/2)(1 - r_{ij}/l_0)^2$ and bend potential $U_{\text{bend}} = k_{\text{bend}}(1 - \hat{\mathbf{r}}_{ij} \cdot \hat{\mathbf{r}}_{jk})$. In the following, the particle types are represented as W for water particle, H for hydrophilic particle and T for hydrophobic particle, respectively.

The thermostat of DPD is a pairwise Langevin thermostat, *i.e.*, Langevin thermostat is applied to every particle pair within cutoff r_{cut}. The strong law of action and reaction is satisfied for all pair forces (even for dissipative and random forces); thus the momentum and angular momentum conservation law are satisfied.

2.1.2 Discretizations

Several discretizations of Eq. (2.1) have been proposed [35, 86, 96]. The most famous one is the modified velocity Verlet method [35]. In modified velocity Verlet

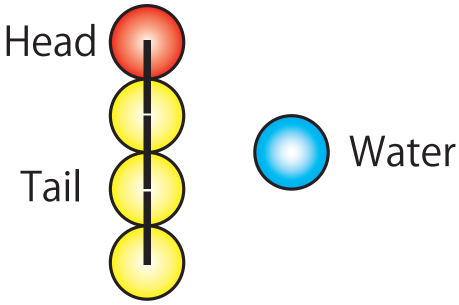

Fig. 2.1: Schematic picture of coarse-grained amphiphile and water.

method, Eq. (2.1) is discretized as

$$\begin{aligned}
\mathbf{r}_i(t+\Delta t) &= \mathbf{r}_i(t) + \Delta t \mathbf{v}_i(t) + \frac{\Delta t^2}{2m}\mathbf{f}_{i,\mathrm{sum}}(t), \\
\tilde{\mathbf{v}}_i(t+\Delta t) &= \mathbf{v}_i(t) + \frac{\lambda_{\mathrm{VV}}\Delta t}{m}\mathbf{f}_{i,\mathrm{sum}}(t), \\
\mathbf{f}_{i,\mathrm{sum}}(t+\Delta t) &= \mathbf{f}_{i,\mathrm{sum}}(\mathbf{r}_i(t+\Delta t), \tilde{\mathbf{v}}_i(t+\Delta t)), \\
\mathbf{v}_i(t+\Delta t) &= \mathbf{v}_i(t) + \frac{\Delta t}{2m}(\mathbf{f}_{i,\mathrm{sum}}(t) + \mathbf{f}_{i,\mathrm{sum}}(t+\Delta t)),
\end{aligned} \tag{2.4}$$

where $\mathbf{f}_{i,\mathrm{sum}} = -\partial U/\partial \mathbf{r}_i + \sum_{i \neq j} \mathbf{f}_{\mathrm{fd}}(\mathbf{v}_{ij}, \mathbf{r}_{ij})$ and Δt is the simulation timestep. When λ_{VV} is set to 0.5, Eq. (2.4) corresponds to the original velocity Verlet method. In modified velocity Verlet method, $\lambda_{\mathrm{VV}} = 0.65$ is usually used because better temperature control is achieved with larger timestep Δt compared with $\lambda_{\mathrm{VV}} = 0.5$ [35].

Other choice of the discretization of Eq. (2.1) is the Shardlow's S1 (the first order sympletic) splitting algorithm [96]. In this method, the conservative forces $-\partial U/\partial \mathbf{r}_i$, and dissipative and random forces $\mathbf{f}_{\mathrm{fd}}(\mathbf{v}_{ij}, \mathbf{r}_{ij})$ are integrated differently. For the integration of the conservative forces, the original velocity Verlet method is used. For the integration of the dissipative and random forces, ij pair is integrated as

$$\begin{aligned}
\mathbf{v}_i^{\mathrm{new}} &= \mathbf{v}_i^{\mathrm{old}} + \left[-A(r_{ij})\mathbf{v}_{ij}\cdot\hat{\mathbf{r}}_{ij} + B(r_{ij})\xi_{ij,n}\right]\hat{\mathbf{r}}_{ij}, \\
\mathbf{v}_j^{\mathrm{new}} &= \mathbf{v}_j^{\mathrm{old}} - \left[-A(r_{ij})\mathbf{v}_{ij}\cdot\hat{\mathbf{r}}_{ij} + B(r_{ij})\xi_{ij,n}\right]\hat{\mathbf{r}}_{ij},
\end{aligned} \tag{2.5}$$

with

$$A(r_{ij}) = \frac{w(r_{ij})\delta t/m}{1 + w(r_{ij})\delta t/m}, \; B(r_{ij}) = \frac{\sqrt{w(r_{ij})\delta t/m}}{1 + w(r_{ij})\delta t/m}. \tag{2.6}$$

The updates of velocities using Eq. (2.5) are performed for all interacting pairs. The multi-time-step algorithm is often used, *i.e.*, the integration timestep δt for

$\mathbf{f}_{\mathrm{fd}}$ is different from the integration timestep Δt for $-\partial U/\partial \mathbf{r}_i$. In this dissertation, we discretize Eq. (2.1) using Shardlow's S1 splitting and use multi-time-step algorithm.

2.1.3 Choices of interaction parameters

The repulsive parameters a_{ij} for same types of particles are typically set to $25k_{\mathrm{B}}T$ with the number density $\rho = 3r_{\mathrm{cut}}^{-3}$ to match the compressibility of liquid water at room temperature [35]. There exist several parameter choices of a_{ij} for different types of particle pairs. For simulations of polymers, a_{ij} for different types of particle pairs are set to match the χ-parameters [35]. For simulations of amphiphiles, $a_{\mathrm{T}\alpha}$, $\alpha = \mathrm{H}, \mathrm{W}$ is set to satisfy $a_{\mathrm{T}\alpha} > a_{\mathrm{TT}}, a_{\mathrm{WW}}, a_{\mathrm{HH}}$ for simulating the hydrophilicity of head segments and hydrophobicity of tail segments.

The choice of dissipative parameters γ_{ij} affects the shear viscosity η and diffusion constant D of DPD fluids. The analytical relationships between η, D and γ_{ij} in the small timestep limit are written as [76]

$$\eta = \frac{3mk_{\mathrm{B}}T}{2\int g_{\mathrm{RDF}}(r)w(r)dV} + \frac{\rho^2}{30}\int r^2 g_{\mathrm{RDF}}(r)w(r)dV, \tag{2.7}$$

$$D = \frac{3k_{\mathrm{B}}T}{\rho\int g_{\mathrm{RDF}}(r)w(r)dV}, \tag{2.8}$$

where $g_{\mathrm{RDF}}(r)$ is the radial distribution function. Both η and D are controlled by γ_{ij} via the weighting function $w(r)$ in Eq. (2.2). According to Eqs. (2.2), (2.7), and (2.8), p and ρ also affect the viscosity of DPD fluids. p is set to 2 in most of DPD simulations to reduce the computational costs (by setting p to 2, we do not need to calculate the square root of $w(r)$), but a liquid phase (Schmidt number $Sc \gtrsim 10$) is not obtained without increasing γ_{ij} up to $50\sqrt{mk_{\mathrm{B}}T}/r_{\mathrm{cut}}$ [76]. To simulate the liquid phase, other choices of p have been proposed: $p = 1$ [100] or $p = 1/2$ [23]. There exist several parameter choices of γ_{ij} for different types of particle pairs [30, 101, 122]. To ensure the correct hydrodynamic behavior for the multi-viscosity system, γ_{ij} are chosen to satisfy a harmonic mean rule, *i.e.*, $\gamma_{ij} = 2/(1/\gamma_{ii} + \gamma_{jj})$ [122].

2.2 SIMD acceleration of molecular simulations

The most time-consuming part of molecular simulations is the non-bonded force calculation. Thus, the acceleration technique of the non-bonded force calculation is essential. In this section, only non-bonded short-range interactions are considered; bonded interactions and long-range electrostatic interactions are not considered.

2.2.1 Basic algorithms of molecular simulations

Verlet neighbor list and bookkeeping method

Verlet neighbor list is widely used to reduce the computational cost of finding pairs that interact each other within cutoff length r_{cut} [9,121]. In the Verlet neighbor list, indices of particle pairs whose distance are less than search length r_s are registered. In the computation of non-bonded forces, we calculate the distances only for the pairs in the Verlet neighbor list. Since the computational cost of Verlet neighbor list construction is high, bookkeeping method is used by setting $r_s = r_{\mathrm{cut}} + \Delta r$ (see Fig. 2.2). r_s is greater than r_{cut}, so same Verlet neighbor list is reusable during several time steps.

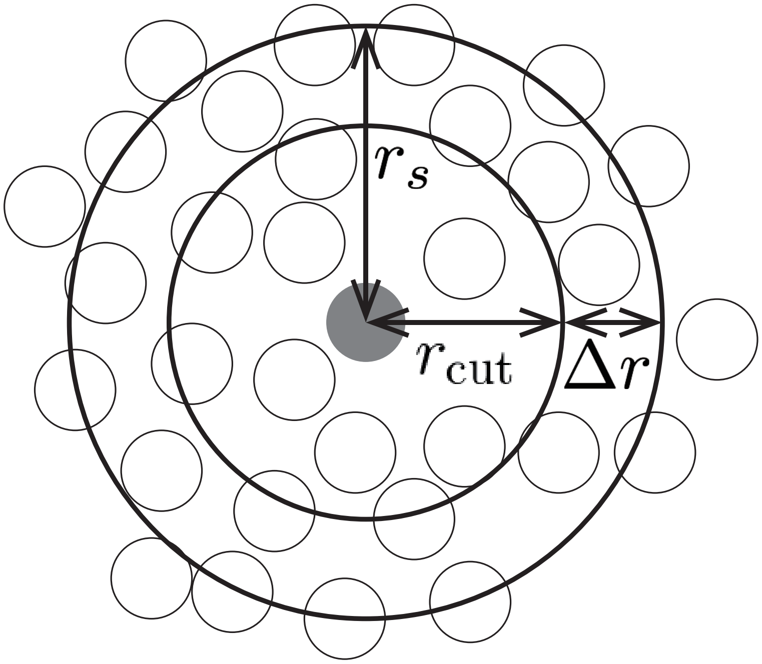

Fig. 2.2: Cutoff length r_{cut} and search length $r_s = r_{\mathrm{cut}} + \Delta r$.

A naive way to construct Verlet neighbor list is to calculate the distances between all particle pairs (Fig. 2.3 (a)), but this approach has an $O(N^2)$ time complexity [121]. To reduce the computational cost, grid search method [123] (also known as the cell linked-list method [9,87]) is often used (Fig. 2.3 (b)). The grid search method has an $O(N)$ time complexity [123], so this method is much faster than $O(N^2)$ naive way.

After the grid search, particle pairs (i, j) such that $i < j, |\mathbf{r}_{ij}| < r_s$ are obtained (Fig. 2.4 (a)). We call the particles whose indices are i (j) key (partner) particles. We sort the partner particles by key particles and store these indices as one dimensional array `SortedList` (Fig. 2.4 (b)). The beginning of neighbor

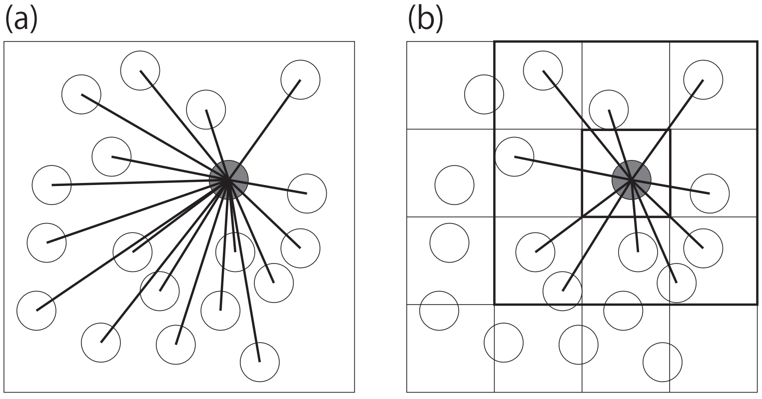

Naive

Grid search method

Fig. 2.3: Two types of Verlet neighbor list construction method. (a) naive $O(N^2)$ method (b) grid search method.

list of kth key particle are stored in `KeyPointer[k]` (Fig. 2.4 (b)). The use of `SortedList` and `KeyPointer` as a Verlet neighbor list is efficient from the viewpoint of cache utilization [123].

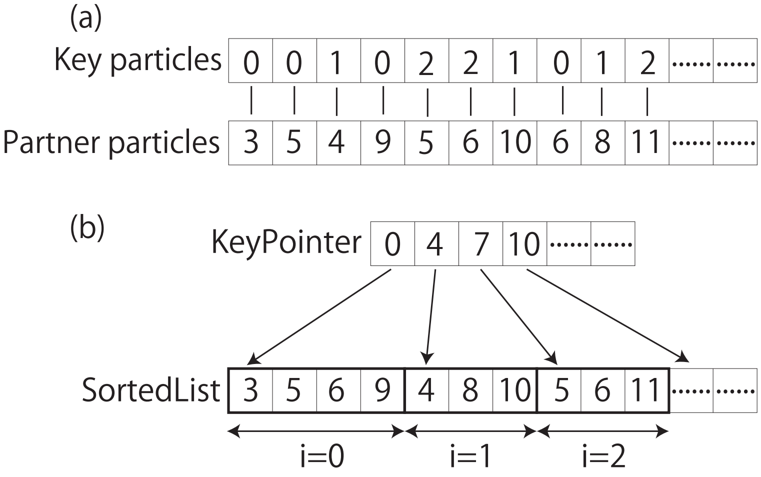

Key particles	0	0	1	0	2	2	1	0	1	2	......	......
Partner particles	3	5	4	9	5	6	10	6	8	11	......	......

KeyPointer	0	4	7	10	......	......

SortedList	3	5	6	9	4	8	10	5	6	11	......	......

Fig. 2.4: (a) Indices of key (partner) particles stored as a one-dimensional array. (b) Indices of partner particles sorted by the indices of key particles.

Force calculation

After building the Verlet neighbor list, we calculate the non-bonded forces using this list. Algorithm 1 shows the pseudo code of non-bonded force calculation. The innermost loop is iterated over the Verlet neighbor list of ith particle.

Algorithm 1 Reference scalar implementation of non-bonded force calculation. $\mathbf{q}[i]$ and $\mathbf{p}[i]$ represent the position and momentum of ith particle, respectively. U, $\mathbf{f}$, and dt are the non-bonded potential, force, and timestep, respectively. NumberOfPartners[i] represents the number of particles included in the Verlet neighbor list of ith particle.

```
for $i = 0$ to NumberOfParticles - 1 do
    $\mathbf{q}_i \leftarrow \mathbf{q}[i]$
    $np \leftarrow$ NumberOfPartners[$i$]
    $kp \leftarrow$ KeyPointer[$i$]
    $\mathbf{f}_i dt \leftarrow \mathbf{0}$
    for $k = 0$ to $np - 1$ do
        $j \leftarrow$ SortedList[$k + kp$]
        $\mathbf{r} \leftarrow \mathbf{q}[j] - \mathbf{q}_i$
        if $r^2 < r_{\mathrm{cut}}^2$ then
            $fdt \leftarrow -U'(|\mathbf{r}|) \times dt/|\mathbf{r}|$
            $\mathbf{f}_i dt \leftarrow \mathbf{f}_i dt + fdt \times \mathbf{r}$
            $\mathbf{p}[j] \leftarrow \mathbf{p}[j] - fdt \times \mathbf{r}$
        end if
    end for
    $\mathbf{p}[i] \leftarrow \mathbf{p}[i] + \mathbf{f}_i dt$
end for
```

2.2.2 Benchmark conditions

We consider Lennard-Jones potential with finite cutoff r_{cut} as the non-bonded interaction, which is written as

$$U_{\mathrm{LJt}}(r) = \begin{cases} 4\epsilon \left[\left(\dfrac{\sigma}{r}\right)^{12} - \left(\dfrac{\sigma}{r}\right)^{6} \right] & (r < r_{\mathrm{cut}}), \\ 0 & (\text{otherwise}), \end{cases} \tag{2.9}$$

where ϵ is well depth, and σ is a diameter of particle. In this section, we use $U_{\mathrm{LJt}}(r)$ as the non-bonded interaction potential.

We use reduced units with σ as the unit of length, ϵ as the unit of energy, m as the unit of mass. Dimensionless quantities are denoted as *, *e.g.* r^* is the dimensionless quantity of distance.

The benchmark conditions are as follows:

- The simulation domain size is set to $50\sigma \times 50\sigma \times 50\sigma$.
- The number of particles is set to 119164.

- As an initial configuration, particles are placed randomly with the avoidance of particle position overlapping.
- Boundary condition is rigid for all axes.
- Cutoff length $r^*_{\mathrm{cut}} = 3$.
- Search length $r^*_s = 3.3$.
- The elapsed time for force calculation 100 steps is measured.

2.2.3 SIMD optimization

There exist three ways to use SIMD instructions. We briefly introduce these ways in the following.

Inline assembly

The use of inline assembly is difficult and low-productivity because the by-hand register mapping of variables is required. Additionally, the inline assembly style depends on compilers, thus the code-portability decreases.

Intrinsics

Intrinsics are the functions corresponding to SIMD instructions. The simdization of scalar codes is performed by calling these functions. The register mapping of variables is performed automatically by the compilers. Therefore, the productivity is higher compared with the use of inline assembly. However, the code-portability decreases because there are the processor-specific instructions.

Auto-vectorization

Recent compilers detect the parallelism of code (*e.g.*, for-loops) and auto-vectorize it if possible. The compilers cannot always auto-vectorize the for-loops due to the data-dependency. The addition of compiler directives such as `#pragma ivdep` or `#pragma simd` enable the auto-vectorization in some cases. This way does not require any processor-specific functions; thus code-portability does not decrease.

We focus on the simdization of Algorithm 1 and resulting performance improvement. We carry out the simdization of the code for two different SIMD widths: 256-bit and 512-bit. The benchmarks are performed on the two different platforms: SGI Altix ICE XA at ISSP Supercomputer Center, University of

System	CPU
SGI Altix ICE X	Intel® Xeon® E5-2680v3 (2.50 GHz)
FUJITSU Server PRIMERGY CX1640 M1	Intel® Xeon Phi™ 7250 (1.40 GHz)

Table 2.1: Summary of system configurations.

Tokyo and FUJITSU Server PRIMERGY CX1640 M1 at the Information Technology Center (ITC), the University of Tokyo. For the performance evaluation of 256-bit simdization, a single node of SGI Altix ICE XA is used. We used Intel C++ Compiler Ver. 16.0.4 with the compiler options `-O3 -xCORE-AVX2`. For the performance evaluation of 512-bit simdization, a single node of FUJITSU Server PRIMERGY CX1640 M1 is used. We used Intel C++ Compiler Ver. 17.0.4 with the compiler options `-O3 -qopt-prefetch=4 -xMIC-AVX512`. System configurations are summarized in Table 2.1. All calculations are performed with double precision. We compare three different implementations for each CPU: simdized implementation by auto-vectorization, simdized implementation by intrinsics, and scalar implementation.

2.2.4 Performance evaluation of 256-bit SIMD

The compiler cannot auto-vectorize the code without any directives. The failure of auto-vectorization is because the compiler cannot recognize that there is no duplication in Verlet neighbor list of the same key particle. Thus, compiler directives are added to the innermost loop as follows:

```
  const auto np = number_of_partners[i];
  double pfx = 0, pfy = 0, pfz = 0;
#pragma vector aligned
#pragma simd reduction(+:pfx, pfy, pfz)
  for (int k = 0; k < np; k++) {
    // calculate forces
  }
```

to auto-vectorize the code.

The simdization of Algorithm 1 is performed using intrinsics following Ref. [85] As pointed out by Pennycook *et al.* [85], gather-scatter operations of positions become the performance bottlenecks. Although gather instructions are included in AVX2, their latencies are relatively high. Therefore, gather-scatter operations of positions are performed using `vmovupd` instruction and several swizzle instructions, such as `vunpckhpd` and `vpermpd`. Moreover, the software pipelining are applied to increase IPC (instructions per cycle). The software pipelining increases the application performance by 1.2 times.

Implementation	Scalar	Auto-vectorization	Intrinsics
Elapsed time [s]	7.138	8.226	2.984

Table 2.2: Results of the benchmark simulation on a single node of SGI Altix ICE X.

Implementation	Scalar	Auto-vectorization	Intrinsics
Elapsed time [s]	33.344	9.794	7.926

Table 2.3: Results of the benchmark simulation on a single node of FUJITSU Server PRIMERGY CX1640 M1.

Table 2.2 shows the performance comparison of three different implementations. The by-hand simdization code using intrinsics gives the best performance. Although the compiler can auto-vectorize the code, the achieved performance is lower than the scalar code. To analyze the performance loss, we look into the assembly of the auto-vectorized code. In the assembly, `vgatherdpd` is used to load positions into YMM registers. Since the latencies of gather instructions are high, auto-vectorized code become slower than the scalar code.

2.2.5 Performance evaluation of 512-bit SIMD

The same compiler directives as Haswell auto-vectorization code are added to the innermost loop. With these compiler directives, the compiler successfully auto-vectorize the code.

For the simdization using intrinsics, there is a minor change from Haswell implementation in the gather-scatter operations of positions. Since the latencies of the gather-scatter instructions in AVX-512 are low, we perform the gather-scatter operations of positions via these instructions. We also apply software pipelining technique to increase IPC. Additionally, we add data prefetch instructions, such as `vgatherpf0dpd` and `vgatherpf1dpd`.

Table 2.3 shows the performance comparison of three implementations. The performance of the auto-vectorized code is nearly equal to the performance of by-hand simdization code using intrinsics unlike the case in Haswell. The low-latency gather-scatter instructions introduced in AVX-512 significantly improve the performance of the auto-vectorized code.

2.3 Summary

In this section, we first overview the DPD method. In the following two chapters, we use the DPD method for the simulation of bilayer membranes. Next, we discuss the SIMD acceleration technique of molecular simulations. We simdized the force calculation code in molecular simulations with two different ways and compare these two implementations with the scalar implementation for two different combinations of hardware and SIMD width. We show that the simdized code using intrinsics gives the best performance for Haswell and Knights Landing processors. The performance of simdized code by the compiler auto-vectorizer is significantly improved by the low latency gather-scatter instructions introduced in AVX-512.

Chapter 3

Shape transformations of bilayer membranes induced by the hydrolysis and condensation reactions

In this chapter, we report the CG simulation study of shape transformations of bilayer membrane induced by the hydrolysis and condensation reactions.

3.1 Introduction

A lipid vesicle, which is one of the basic self-assembled structures of lipid molecules, has been studied as a minimum model of living cells. Although vesicles are composed of only lipid molecules, they exhibit various shape transformations such as discocyte, stomatocyte, and starfish depending on reduced volumes and spontaneous curvatures [93]. These various shape transformations can be well described using the elastic theory proposed by Helfrich [39, 93]. The theoretical prediction agrees well with experiments quantitatively [91].

For the above-mentioned studies on vesicle morphology, it is assumed that the membrane composition is constant. However, in living cells, synthesis and decomposition of lipids continually occur by lipid metabolism so that the membrane composition changes. For example, phospholipids are synthesized from fatty acids on endoplasmic reticulum (ER) membrane [15], after which these molecules are transported to other organelles via vesicle transport mechanisms. Another example is hydrolysis of phospholipids [71, 72]. The reaction products, diacylglycerols (DAGs), play the key role in protein kinase C activation [14].

The effects of non-constant membrane composition on shape transformations of cells have been studied by several groups [7, 8, 41, 48, 88]. The nature of non-constant membrane composition is often mimicked by hydrolysis and condensation reactions. For example, an injection of a hydrolase enzyme to red blood cells (RBCs) [7, 8] and lipid vesicles [41, 48] hydrolyzes amphiphilic molecules into hydrophilic and hydrophobic molecules. In these chemical reactions, amphiphilic molecules, which are composed of hydrophilic (A) and hydrophobic (B) parts, change as follows:

$$\mathrm{AB} + \mathrm{H_2O} \rightleftharpoons \mathrm{A{-}H} + \mathrm{B{-}OH}, \tag{3.1}$$

where the right and left arrows represent the hydrolysis and condensation reactions, respectively. The experiments demonstrate that vesicles show the various shape transformations under these chemical reactions [7, 8, 41, 48]. The injection of hydrolase enzyme to RBCs and liposomes induces membrane invagination and rupture. Toyota *et al.* [114] reported that discocytes transform into tubular and invaginated shapes under the hydrolysis reaction of amphiphilic molecules.

A possible explanation of these morphological changes was proposed in terms of the ADE model [8]. The hydrolase enzyme is injected from the outer solution so that the density of the amphiphilic molecules in the outer leaflet of a vesicle decreases, whereas the density of the inner leaflet is nearly constant. Therefore, the amphiphilic molecular densities in the inner and outer leaflets become different. To reduce the ADE energy [93, 97] of this area difference, liposomes and RBCs form an invagination. A similar asymmetry in amphiphilic molecules that is induced by chemical reactions is widely observed *in vitro* [107] and *in vivo* [15].

However, in the previous works, the effects of the resulting products (A–H and B–OH molecules in Eq. (3.1)) are not taken into account explicitly. Instead, the effect of these chemical reactions is taken into account implicitly by the change in the amphiphilic molecular densities of the inner and outer leaflets in the ADE model. However, the chemical reaction products, hydrophobic molecules (B–OH) are included in the bilayer membrane, and such inclusions modify the elastic properties of the bilayer [63]. We have previously examined how such inclusions affect shape transformations of a bilayer membrane induced by a binding reaction of hydrophobic and hydrophilic molecules [68]. The inclusions are concentrated in the branches of the membranes. The stabilization of branched structures by these inclusions was also reported in Refs. [12, 20]. Thus, shape transformations of membranes occur due to the presence of the resulting hydrophobic molecules, but these shape transformations are not fully understood.

The aim of this chapter is to clarify the effect of embedded hydrophobic products on shape transformations under the hydrolysis and condensation reactions. We use the coarse-grained molecular dynamics simulation technique, in which the hydrolysis and condensation reaction processes of amphiphilic molecules are taken into account explicitly. We will show that the shape transformation strongly de-

	W	H	T
W	25	25	200
H	25	25	200
T	200	200	25

Table 3.1: Repulsive interaction parameters a_{ij} with units $k_{\mathrm{B}}T$. W, H, and T represent water, hydrophilic and hydrophobic particles, respectively.

pends on the distribution of the resulting products (B–OH) included in the bilayer. We will also show that not only membrane invagination but also bilayer sheet formation occur depending on the reduced volume. The shape transformation pathway is also affected by the transport coefficients of the surrounding fluids and membrane.

In Sec. 3.2, the simulation model, method, and simulation settings are described. The results are presented in Sec. 3.3, and discussions and conclusions are given in Sec. 3.4.

3.2 Simulation methods

3.2.1 Model and method

We use the dissipative particle dynamics (DPD) simulation technique [34, 35, 43]. Since we describe the essence of DPD method and CG model of amphiphile in Chapter 2, we only show the choices of parameters in this section. Four particles constituting an amphiphile are connected via the bond potential $U_{\mathrm{bond}} = k_{\mathrm{bond}}(1 - r_{ij}/l_0)^2/2$ and the bend potential $U_{\mathrm{bend}} = k_{\mathrm{bend}}(1 - \hat{\mathbf{r}}_{ij} \cdot \hat{\mathbf{r}}_{jk})$ with $k_{\mathrm{bond}} = 272k_{\mathrm{B}}T$, $k_{\mathrm{bend}} = 60k_{\mathrm{B}}T$, and $l_0 = 0.8r_{\mathrm{cut}}$. We choose $p = 1/2$ to increase the shear viscosity of the DPD fluids [23]. The multi-time-step algorithm [76, 86, 115] is employed with the integration time step $\Delta t = 0.005r_{\mathrm{cut}}\sqrt{m/k_{\mathrm{B}}T}$ for the conservative forces and $\delta t = 0.05r_{\mathrm{cut}}\sqrt{m/k_{\mathrm{B}}T}$ for dissipative and random forces.

The repulsive parameters a_{ij} are listed in Table 3.1. The dissipative parameters γ_{ij} for the same type of particle pairs are shown in Sec. 3.3. For different types of particle pairs, a harmonic mean rule is employed, *i.e.*, $\gamma_{ij} = 2/(1/\gamma_{ii} + 1/\gamma_{jj})$, to ensure the correct hydrodynamic behavior for the multi-viscosity system [122]. A stable bilayer structure forms with bending rigidity $\kappa = 18.1 \pm 0.4k_{\mathrm{B}}T$ and area expansion modulus $K_A = 18.9 \pm 1.1k_{\mathrm{B}}T/r_{\mathrm{cut}}^2$. These elastic properties agree well with the experimental results at room temperature [16, 93].

We use reduced units with r_{cut} as the unit of length, $k_{\mathrm{B}}T$ as the unit of energy, and m as the unit of mass. r_{cut} is the length scale of the molecule, $r_{\mathrm{cut}} \sim 1$ nm, and $\tau = r_{\rm cut}\sqrt{m/k_{\rm B}T}$ is estimated to be ∼1 ns at room temperature $T \sim 300$ K. Dimensionless quantities are denoted by *, *e.g.*, $t^* = t/\tau$.

Several chemical reaction models combined with the DPD method have been proposed [47,60,61,68]. In this work, we use the chemical reaction model, in which hydrolysis and condensation reactions of amphiphilic molecules are represented by a bond dissociation and bond binding as shown in Fig. 3.1. Because the dissociated hydrophilic and hydrophobic molecules are typically dissolved in surrounding fluids and embedded in the bilayer, we refer to them as the hydrophilic solute (HS) and embedded oil (EO), respectively. The HS can have a binding reaction to only the one end particle of the EO ($j_{\rm am} = 2$ shown in Fig. 3.1). Both binding and dissociation processes are treated as stochastic processes, as in the polymerization model [47]. Probabilities for the bond binding and dissociation during Δt are given by

$$p_{\rm diss} = \begin{cases} p_{\rm f}\Delta t & (n_{\rm water} > 0) \\ 0 & (\text{otherwise}) \end{cases}, \tag{3.2}$$

$$p_{\rm bind} = p_{\rm r}\Delta t \Theta\left(1 - \frac{r_{\rm min}}{r_{\rm bind}}\right), \tag{3.3}$$

where $p_{\rm f}$ and $p_{\rm r}$ denote the transition rates of the dissociation and binding reactions, respectively. $n_{\rm water}$ is the number of water particles that exist in a sphere with a radius of $0.69r_{\rm cut}$ around a hydrophobic particle of $j_{\rm am} = 2$ connecting with a hydrophilic particle. The hydrophobic particles of $j_{\rm am} = 2$ in the EO bind with the closest HS by the reaction rate $p_{\rm r}$ when the distances $r_{\rm min}$ between the two particles are less than the cutoff length $r_{\rm bind}$. In this study, $r_{\rm bind} = r_{\rm cut}$ is used. The bond dissociation probability increases when the HS concentration is low. When the bond binding rate is equal to the bond dissociation rate, the system reaches chemical equilibrium.

We investigate the effects of the viscosity $\eta_{\rm sol}$ of the surrounding solutions and the effective viscosity $\eta_{\rm mb}$ in the membrane. The viscosity of the surrounding fluids can be controlled by $\gamma_{\rm sol} = \gamma_{\rm HH} = \gamma_{\rm WW}$. The shear viscosity of the DPD fluids increases with increasing γ. The shear viscosity $\eta_{\rm sol}$ is estimated from a simple shear flow for the DPD fluid consisting of only W particles [76]: $\eta^*_{\rm sol} = 1.119 \pm 0.004$ and 5.262 ± 0.007 for $\gamma^*_{\rm sol} = 2$ and 24.5, respectively. The diffusion constants D of the DPD fluids are estimated from the mean square displacement: $D^* = 1.326$ and 0.301 for $\gamma^*_{\rm sol} = 2$ and 24.5, respectively. To change the effective viscosity $\eta_{\rm mb}$ in the membrane, we vary $\gamma_{\rm TT}$ of the tail and EO particles: $\gamma^*_{\rm TT} = 2$ and $\gamma^*_{\rm TT} = 24.5$. Thus, the DPD fluids consisting of nonbonded tail particles have $\eta^*_{\rm mb} = 1.119$ and 5.262. However, the bond and angle potentials in the amphiphilic molecules modify this simple linear viscosity. In the bilayer membranes, the amphiphilic molecules in the membrane have two types of hydrodynamic interactions: lateral

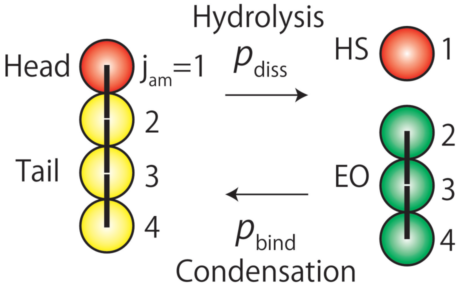

Fig. 3.1: Schematic picture of hydrolysis and condensation reactions. For clarity, the hydrophobic particles in amphiphilic molecules and in the EOs are colored yellow and green, respectively. Both hydrophilic and hydrophobic particles have their own ids: $j_{\text{am}} = 1$ for the hydrophilic particles, and $j_{\text{am}} = 2, 3, 4$ for the hydrophobic particles. The figure is adapted from Fig. 1 in [70].

interactions that give rise to 2D membrane viscosity and the friction between two leaflets [21,93,104]. A greater value of γ_{TT} yields a higher 2D viscosity and stronger friction. However, because the EOs in the bilayer modify both the interactions, it is difficult to quantitatively estimate them. Therefore, we consider only the qualitative effects of the membrane viscosity using the viscosity η_{mb} of the DPD fluid, in this study.

3.2.2 Simulation settings

All simulations are carried out in an NVT ensemble (constant number N of particles, volume V, and temperature T) at the particle density $N/V = 3/r_{\text{cut}}^3$. The cubic simulation boxes with $L_x = L_y = L_z = 36r_{\text{cut}}$ and $48r_{\text{cut}}$ are used for a flat membrane and vesicle, respectively.

We prepare a flat bilayer membrane with $N_{\text{amp}} = 4950$ and $N_{\text{EO}} = 0$. The bounce-back rule is employed at the boundary of the simulation box along the normal (z) direction to the bilayer, and periodic boundary conditions are employed in the lateral (x, y) directions. Initially, the HS concentrations of the fluids above and below the membrane are $c^*_{\text{up}} = 3$ and $c^*_{\text{low}} = 0$, respectively. The solvent particles are distributed in the above and below the membrane; the number of solvent particles in the above and below the membrane are $N_{\text{sol,up}} = 60084$ and $N_{\text{sol,low}} = 60084$, respectively. The initial parameter settings are summarized in Table 3.2. Since these two fluids do not contact each other directly, their HS concentrations are changed only by the reactions on the membrane.

To investigate the spatial distribution of the EOs in the membrane in the absence of the chemical reactions, a flat membrane with $N_{\text{EO}} = 1000$ and $N_{\text{amp}} = 3950$ is used. The EOs are distributed uniformly in the bilayer membrane as

	N_{amp}	$N_{\mathrm{sol,up}}$	$N_{\mathrm{sol,low}}$	c^*_{up}	c^*_{low}	N_{EO}	L^*_x	L^*_y	L^*_z
flat bilayer	4950	60084	60084	3	0	0	36	36	36

Table 3.2: Initial simulation settings for investigating morphological changes of flat bilayer membranes induced by chemical reactions.

	N_{amp}	$N_{\mathrm{sol,in}}$	$N_{\mathrm{sol,out}}$	N_{EO}	L^*_x	L^*_y	L^*_z
spherical vesicle	17730	52670	208186	0	48	48	48
disk vesicle	19338	35679	218745	0	48	48	48

Table 3.3: Initial simulation settings for investigating morphological changes of vesicles induced by chemical reactions. HS concentration of inside and outside the vesicle are described in the main text.

initial conformations, and the positions of the EOs are fixed for the first 500τ to make the amphiphilic molecules relax first. The position constraint of the EOs is removed at $t = 500\tau$. The surface density is calculated with a spatial mesh size of $r_{\mathrm{mesh}} = 4r_{\mathrm{cut}}$.

We consider initially a nearly spherical vesicle and a discocyte-shaped vesicle under periodic boundary conditions in all three directions. The spherical vesicle is formed by $N_{\mathrm{amp}} = 17730$ of amphiphilic molecules, and $N_{\mathrm{sol,in}} = 52670$ ($N_{\mathrm{sol,out}} = 208186$) particles are inside (outside) the vesicle. The discocyte has $N_{\mathrm{amp}} = 19338$ and $N_{\mathrm{sol,in}} = 35679$. The reduced volumes $v = V_{\mathrm{ves}}/(4/3\pi(A_{\mathrm{mb}}/4\pi)^{3/2})$ for the spherical vesicle and discocyte are nearly equal to 1 and 0.5, respectively, where V_{ves} and A_{mb} are the volume and surface area of the vesicle. Initial vesicles are prepared using the methods described in Appendix 3.A. The simulation time t is set to zero when the chemical reactions start. The initial parameter settings are summarized in Table 3.3.

In the experimental studies [7, 8, 41, 48] shown in Sec. 1, the chemical environment is different inside and outside a vesicle. As a model of such asymmetric situations, we consider the vesicle whose inner and outer solutions have different concentrations of HSs. One may consider that the asymmetric concentration along the bilayer membrane causes the osmotic pressure difference. However, the time scale of the volume change due to the osmotic pressure difference is much longer than the shape transformation timescale. We will show how the shape transformation of vesicles under the hydrolysis and condensation reactions is changed by the concentration difference of HSs. The initial concentration c_{out} of HSs outside the vesicle is set to 0. The initial concentration c_{in} of HSs inside the vesicle is varied to control the concentration difference.

3.3 Simulation results

3.3.1 Bilayer sheet protrusion from flat membrane

First, we consider the shape transformations of the flat membrane by chemical reactions (see Fig. 3.2). The HS concentration difference causes different time developments of the number of amphiphilic molecules between the upper and lower leaflets as shown in Fig. 3.2(d): the number of amphiphilic molecules $N_{\mathrm{amp,up}}$ ($N_{\mathrm{amp,low}}$) of the upper (lower) leaflet increases (decreases). On the lower leaflet, the condensation reaction is very slow owing to the low HS concentration of the lower solution, with the result that the hydrolysis reaction largely proceeds. The EOs are then generated at the lower leaflet and embedded in the bilayer membrane, as indicated by the green color in Fig. 3.2(a). On the other hand, the condensation reaction largely proceeds on the upper leaflet owing to the high HS concentration of the upper solution, with the result that amphiphilic molecules are synthesized in the upper leaflet.

The resulting asymmetric distribution of amphiphilic molecules produces a negative surface tension in the upper leaflet and a positive surface tension in the lower leaflet, so that the upper (lower) leaflet is compressed (expanded). This compression induces a large undulation of the upper leaflet. Figures 3.2(e) and (f) show the time development of the surface tension Γ of the bilayer and maximum height h_{max} of the membrane. The surface tension (mechanical frame tension) is estimated as $\Gamma = (P_{zz} - (P_{xx} + P_{yy})/2)L_z$ from the stress tensor [120]. Note that Γ is the sum of two surface tensions: the surface tension Γ_{up} of the upper leaflet and the surface tension Γ_{low} of the lower leaflet. Since the hydrolysis reaction is faster than the condensation reaction, $\langle N_{\mathrm{amp,low}} \rangle$ has a greater slope than $\langle N_{\mathrm{amp,up}} \rangle$, and the total surface tension Γ then increases (see the data at $0 < t^* < 2000$ in Figs. 3.2(d) and (e)). A further increase in the surface tension induces the buckling of the upper leaflet into the protrusion of a bilayer sheet (indicated by arrows in Fig. 3.2(b)). We hereafter refer to this deformation as bilayer protrusion (BP) formation. The edge of the BP is tongue-shaped owing to the edge line tension. Because the line tension of the branching junction between the BP and the bilayer is low in the high-EO-density area, the BP grows in the high-EO-density area as shown in Figs. 3.2(b') and (b"). The surface tension Γ and maximum membrane height h_{max} rapidly increase during BP formation at $t^* \simeq 2000$ (see Figs. 3.2(e) and (f)). The BP releases the compressive (negative) surface tension Γ_{up} in the upper leaflet, which increases Γ.

To investigate the effects of the viscosities of the surrounding fluids and membrane on the stress relaxation timescales of BP formation, we started simulations with different γ_{sol} and γ_{TT} values from membranes equilibrated at the EO ratio $N_{\mathrm{EO}}/N_{\mathrm{amp}} \simeq 0.06$ by stopping the chemical reactions. When the viscosity η_{sol}

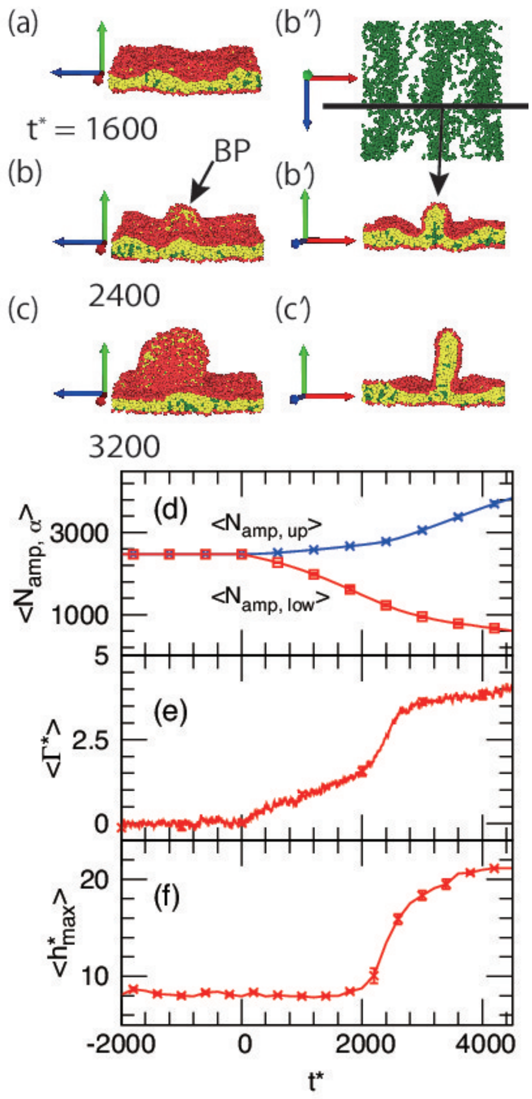

Fig. 3.2: (a–c') Sequential snapshots of a bilayer sheet protrusion (BP) from a flat membrane at $p_{\mathrm{f}}^* = 20$, $p_{\mathrm{r}}^* = 180$, $\gamma_{\mathrm{sol}}^* = 2$, and $\gamma_{\mathrm{TT}}^* = 2$. The number presents the simulation time t^*. (a), (b), (c) Bird's-eye view. (b'), (c') Cross sections of (b), (c) in front view. (b") Only EOs of (b) are shown from the z direction. Bold line of (b") represents the cross section of (b'). Time development of (d) $\langle N_{\mathrm{amp,up}} \rangle$ and $\langle N_{\mathrm{amp,low}} \rangle$, (e) surface tension Γ , and (f) maximum height h_{max} of the membrane. The error bars are calculated from eight independent runs. Symbols are shown for several data points. Smoothed data are shown for Γ. The figure is adapted from Fig. 2 in [70].

of the surrounding fluids and the effective membrane viscosity η_{mb} are increased roughly fivefold by changing γ_{sol} and γ_{TT}, BP formation is delayed by 400τ and 800τ, respectively (see Fig. 3.3). This larger delay shows that the viscosity in the membrane has a stronger influence on BP formation.

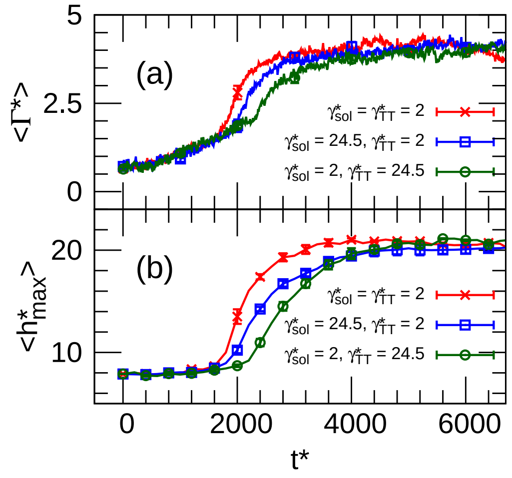

Fig. 3.3: Time development of (a) the surface tension Γ and (b) maximum height h_{max} of membrane for different viscosities. The error bars are calculated from eight independent runs. Symbols are shown for several data points. Smoothed data are shown for Γ. The figure is adapted from Fig. 3 in [70].

In our simulation, the EOs are inhomogeneously distributed in the membrane. To clarify whether this EO inhomogeneity is generated thermodynamically or kinetically, we simulate the equilibrium flat membrane in the absence of chemical reactions. Figure 3.4 shows the time development of the surface density inhomogeneity δn_{EO} of the EOs. The distribution of the EOs becomes inhomogeneous even if their initial distribution is uniform. The EOs self-assemble into several clusters in the bilayer membrane (see Fig. 3.4(b)). Thus, this inhomogeneity exists in thermal equilibrium. The relaxation time τ_{inhomo} from uniform to nonuniform spatial EO distributions depends on the diffusion constant D_{EO} of the EOs. Under faster EO diffusion, δn_{EO} reaches equilibrium more rapidly (see Fig. 3.4(c)). This inhomogeneous nature is related to the orientational order of the bilayer membranes [68]. The orientational order of amphiphilic molecules is disturbed by the contacted EOs.

3.3.2 Morphological changes at $v \simeq 1$

Next, we consider the shape transformations of a vesicle at $v \simeq 1$ and the initial HS concentration difference $\Delta c^* = 3$ (see Fig. 3.5). This concentration difference

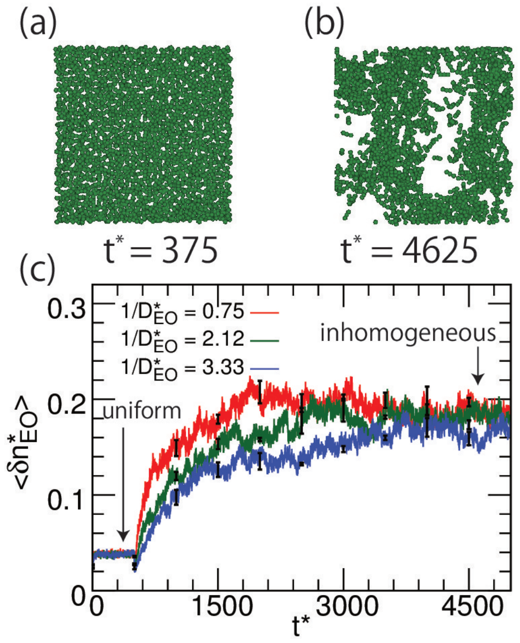

Fig. 3.4: Time development of δn_{EO} of flat membrane for different D_{EO} values. Position restraints of EOs are removed at $t = 500\tau$. Two snapshots represent only EOs in the bilayer membrane for $\gamma^*_{\mathrm{TT}} = 2$. The left snapshot shows that EOs are uniformly distributed in the bilayer membrane. The right snapshot shows the inhomogeneous distribution of EOs. Symbols are shown for several data points. The error bars are calculated from three independent runs. The figure is adapted from Fig. 4 in [70].

causes the transport of amphiphilic molecules from the outer leaflet to the inner leaflet as in the flat membrane (see Fig. 3.5(e)).

We estimate the surface tension Γ_{in} of the inner leaflet in the following manner. Since vesicles before shape transformations are nearly spherical because $v \simeq 1$, the surface tension Γ_{in} of the inner leaflet is approximately estimated as

$$\Gamma_{\mathrm{in}} = K_A \frac{4\pi(R_{\mathrm{ves}} - h_{\mathrm{neut}})^2 - N_{\mathrm{amp,in}} a_0}{N_{\mathrm{amp,in}} a_0}, \tag{3.4}$$

where $a_0 = 0.52 r_{\mathrm{cut}}^2$ is the area per lipid molecule in the tensionless membrane, R_{ves} is the radius of the vesicle, and $h_{\mathrm{neut}} = 0.9 r_{\mathrm{cut}}$ is the distance between the inner leaflet neutral surface and the bilayer mid-plane. The negative surface tension of Γ_{in} induces the buckling of the inner leaflet, leading to the formation of multiple BPs; these BPs are indicated by the arrows in Fig. 3.5(c) and the right panel of Fig. 3.6. This BP formation process can be captured by the time development of the standard deviation of the bilayer thickness δd (the calculation method is described in Appendix 3.B) as shown in Fig. 3.5(g). During the undulation, δd gradually increases, and after the buckling starts, δd rapidly increases at $t^* > 1500$.

BP formation depends on the initial HS concentration difference Δc as shown in Fig. 3.7. As Δc increase, the reaction rates $dN_{\mathrm{amp,in}}/dt$ increase, whereas $dN_{\mathrm{amp,out}}/dt$ shows little dependence. BP formation becomes faster with increasing Δc as a result of the increase in $dN_{\mathrm{amp,in}}/dt$. BP formation occurs everywhere except at $\Delta c^* = 0$. Thus, the synthesis of amphiphilic molecules and the resulting negative surface tension of the inner leaflet are necessary for BP formation.

As shown in the flat membrane simulation in Sec. 3.3.1, the BPs protrude from the EO clusters (Figs. 3.2 (b') and (b")). Thus, these clusters accelerate BP formation. Hence, we next examine the spatial inhomogeneity of the EOs in the bilayer membrane and its relation with BP formation. The spatial inhomogeneity of the EOs is determined by two processes: the synthesis and diffusion of the EOs. The synthesis of the EOs occurs uniformly on the outer leaflet, leading to a homogeneous EO distribution. The characteristic timescale τ_{homo} of this process is the reciprocal of the EO synthesis speed. On the other hand, the EOs in the bilayer membrane self-assemble into several clusters, and thus the spatial distribution of the EOs becomes inhomogeneous as discussed in the case of the flat membrane. This characteristic timescale τ_{inhomo} of the EO assembly into clusters decreases (increases) for faster (slower) diffusion of the EOs. The relationship between these two timescales τ_{homo} and τ_{inhomo} affects the inhomogeneity of the EOs. When $\tau_{\mathrm{homo}} > \tau_{\mathrm{inhomo}}$, the EOs self-assemble into clusters rapidly, but otherwise they remain close to the uniform distribution. We confirm this tendency by simulations in which τ_{inhomo} is varied by changing the diffusion constant D_{EO} of the EOs. Figures 3.8(a) and (b) show the time development of the mean surface density of the EOs n_{EO} and its inhomogeneity $\delta n_{\mathrm{EO}}(t)$, which is defined as the standard devia-

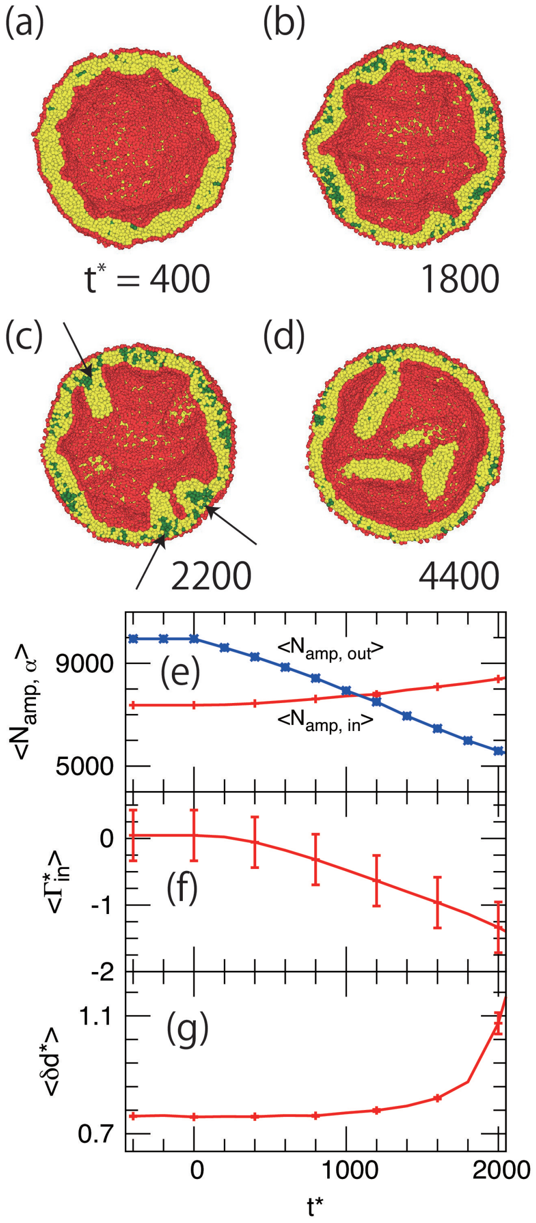

Fig. 3.5: (a–d) Sequential snapshots of vesicle at $v \simeq 1$, $p_{\mathrm{f}}^* = 80$, $p_{\mathrm{r}}^* = 160$, $\Delta c^* = 3$, $\gamma_{\mathrm{sol}}^* = 2$, and $\gamma_{\mathrm{TT}}^* = 18$. The numbers present the simulation time t^*. The front halves of the vesicles are not displayed to show the inner structures of the vesicle. (e–g) Time development of (e) $\langle N_{\mathrm{amp,in}} \rangle$ and $\langle N_{\mathrm{amp,out}} \rangle$, (f) surface tension $\langle \Gamma_{\mathrm{in}} \rangle$ of inside monolayer calculated by Eq. (3.4), and (g) thickness inhomogeneity $\langle \delta d \rangle$. Symbols are shown for several data points. The error bars are calculated from eight independent runs. The figure is adapted from Fig. 5 in [70].

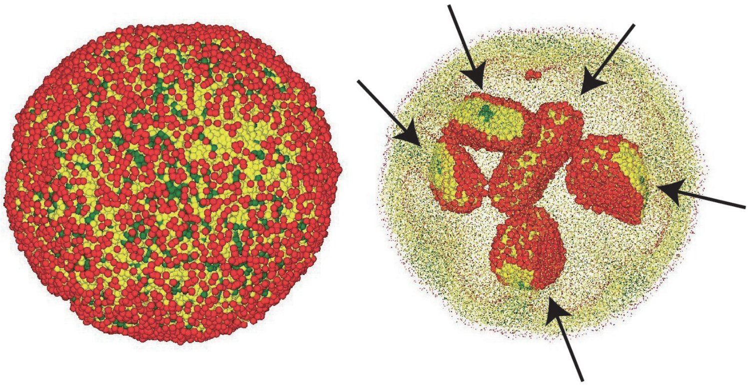

Fig. 3.6: Snapshots of BP formation. The right panel shows the internal structure of the left panel. There exist five BPs in the inner leaflet as shown in the arrows of the right panel. The same simulation settings as Fig. 3.5 are employed.

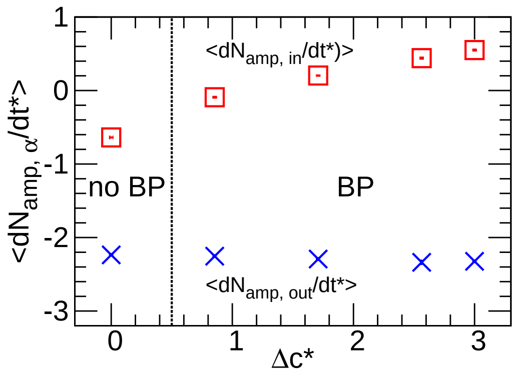

Fig. 3.7: Reaction rates of amphiphilic molecules in each leaflet as a function of the initial concentration difference Δc^* at $\gamma^*_{\mathrm{sol}} = \gamma^*_{\mathrm{TT}}$=2. BPs form at $c^* = 0.854, 1.71, 2.56,$ and 3. The vertical dotted line serves as a guide for the eye for the threshold of BP formation. The figure is adapted from Fig. 6 in [70].

tion of the surface density of the EOs, for different D_{EO} values. The EO density is calculated by using a bin of solid angle $\omega = 16a_0/(4\pi R_{\mathrm{ves}}^2)$ in the spherical vesicle. The time development of $n_{\mathrm{EO}}(t)$ is not affected by the change in D_{EO}, as shown in Fig. 3.8(a), so that τ_{homo} does not depend on D_{EO}. On the other hand, the time development of δn_{EO} clearly depends on D_{EO} at the late stage $t^* \in [1000, 1400]$. In the beginning of the chemical reaction (at $t^* < 1000$ in Fig. 3.8(b)), the spatial inhomogeneity, δn_{EO}, decreases as the EOs are synthesized. For fast diffusion $1/D_{\mathrm{EO}}^* = 0.75$, the EOs form clusters, and δn_{EO} becomes larger compared to slow diffusion case at $t^* \in [1000, 1400]$. Thus, $\tau_{\mathrm{homo}} > \tau_{\mathrm{inhomo}}$ is satisfied. However, for slow diffusion, $1/D_{\mathrm{EO}}^* = 2.12$ and 3.33, the EOs are uniformly distributed even at $t^* \in [1000, 1400]$, and the cluster formation occurs at later stages.

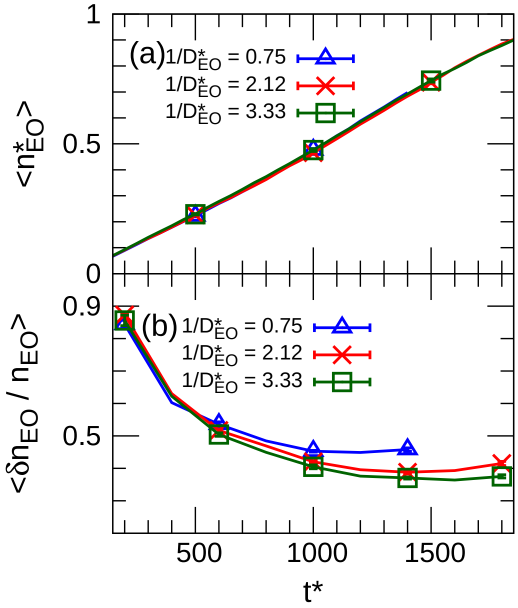

Fig. 3.8: Time development of (a) the average $\langle n_{\mathrm{EO}} \rangle$ and (b) standard deviation $\langle \delta n_{\mathrm{EO}}/n_{\mathrm{EO}} \rangle$ of the surface density of EOs for various D_{EO} values at $p_{\mathrm{f}}^* = 80$, $p_{\mathrm{r}}^* = 160$, and $\gamma_{\mathrm{sol}}^* = 2$. γ_{TT}^* is varied from 2 to 24.5 to change D_{EO}. Symbols are shown for several data points. The error bars are calculated from eight independent runs. The figure is adapted from Fig. 7 in [70].

More BPs form at slower diffusion and faster reactions as shown in Fig. 3.9. At small values of the diffusion constant D_{EO}, slower EO cluster formation delays BP formation. Since the synthesis rate of EOs does not depend on the D_{EO} as shown in Fig. 3.8 (a), the number of EOs at the BP formation increases at lower D_{EO}. At high reaction rates p_{f}^* and p_{r}^*, the surface tension increases more rapidly. In both cases, at BP formation, the larger number of EO clusters exist in the bilayer membrane, and the membrane is under a greater compressive tension at

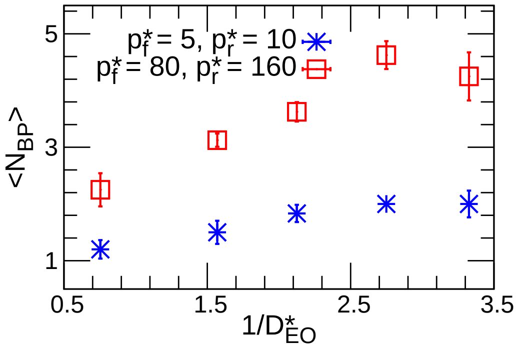

Fig. 3.9: Number $N_{\rm BP}$ of BPs as a function of $1/D_{\rm EO}$ for two reaction rate settings of $p_{\rm f}$ and $p_{\rm r}$ at $\gamma^*_{\rm sol} = 2$. The error bars are calculated from six independent runs. The figure is adapted from Fig. 8 in [70].

BP formation. This leads to the formation of more BPs at the same time instead of a single large BP.

At low number $N_{\rm BP}$ of BPs, the BP bends and finally transforms into the spherical vesicle as shown in Fig. 3.10. Since the initial shape of the BP is a nearly flat disk, this shape transformation can be regarded to as the shape transformation from flat bilayer disk to spherical vesicle. This type of shape transformation is roughly described by the theory by Fromherz [26]; the excess energy ΔE relative to the flat bilayer disk is written as

$$\begin{gathered}\frac{\Delta E(x,\zeta)}{4\pi(2\kappa+\bar{\kappa})} = x^2 + \zeta\left[\sqrt{1-x^2}-1\right], \\ \zeta = \frac{\Gamma_{\rm edge}R_{\rm mb0}}{2\kappa+\bar{\kappa}},\ x = \frac{R_{\rm mb0}}{R_{\rm mb}},\ \text{and}\ R_{\rm mb0} = \sqrt{\frac{A_{\rm mb}}{4\pi}},\end{gathered} \tag{3.5}$$

where $\Gamma_{\rm edge}$, $A_{\rm mb}$ and $1/R_{\rm mb}$ are the edge line tension, area, and curvature of the membrane, respectively. The intermediate shape of bilayer disk is assumed to be the spherical cap. Equation 3.5 shows that the flat bilayer disk is energetically unstable at $\zeta > 2$; a flat bilayer disk that has a large $A_{\rm mb}$ tends to shrink its edge-line and transforms into the sphere to reduce the high edge-line energy. The growth of flat BP caused by the synthesis of amphiphilic molecules in the inner leaflet leads to the shape transformation from the flat BP to the spherical vesicle. At high number $N_{\rm BP}$ of BPs, there is not enough space inside the vesicle for the shape transformation from the flat BP to spherical vesicle; thus the BP remains flat.

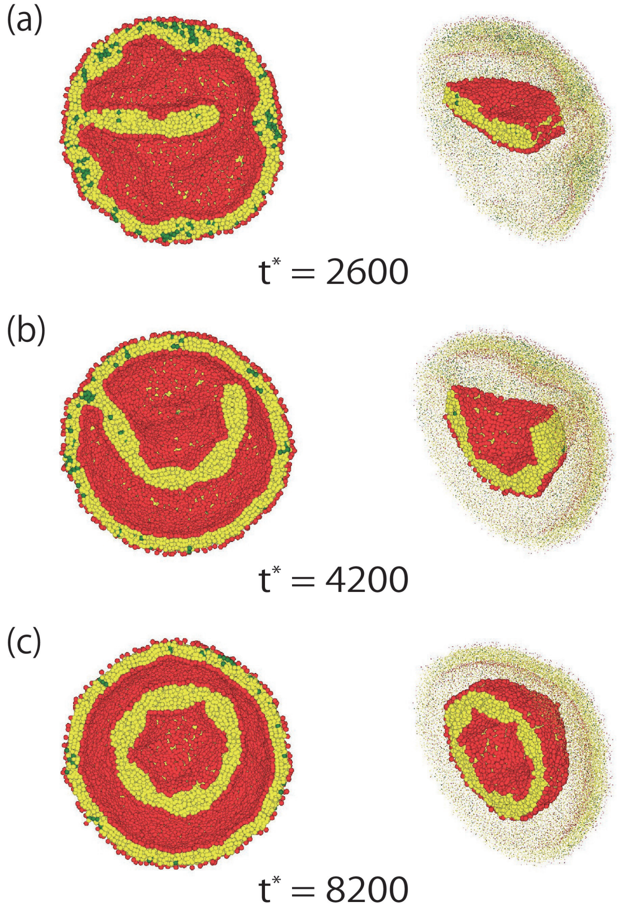

Fig. 3.10: (a–c) Sequential snapshots of shape transformation from the flat BP disk to vesicle at $v \simeq 1$, $p_{\mathrm{f}}^* = 80$, $p_{\mathrm{f}}^* = 160$, $\Delta c^* = 3$, $\gamma_{\mathrm{sol}}^* = 2$, $\gamma_{\mathrm{TT}}^* = 2$. Cross-sectional images (left) and inside views (right) of the vesicle are shown. The number presents the simulation time t^*. The figure is adapted from Fig. 9 in [70].

3.3.3 Morphological changes at $v \simeq 0.5$

Next, we consider the shape transformations at a low reduced volume, $v \simeq 0.5$. The initial shape is discocyte (see Fig. 3.11(a)). The same settings as in Sec. 3.3.2 are considered: the HS concentration is different inside and outside the vesicle. Thus, the hydrolysis and condensation reactions mainly occur on the outer and inner leaflets, respectively.

For the low reduced volume, large low-wavelength fluctuations of the bilayer are permitted unlike for $v \simeq 1$, leading to a different type of shape transformation, budding into a stomatocyte. Figure 3.11 shows the typical shape transformation. As the hydrolysis and condensation reactions proceed, a dimple invagination forms (Fig. 3.11(b)), and eventually the discocyte transforms into a stomatocyte (see Figs. 3.11(c) and (d)). A decrease and increase in the amphiphilic molecular densities of the outer and inner leaflets, respectively, cause an effective negative spontaneous curvature according to the ADE model so that the inner bud is stabilized. After the budding, a further increase of amphiphilic molecular density of the inner leaflet causes BP formation, as in the $v \simeq 1$ case.

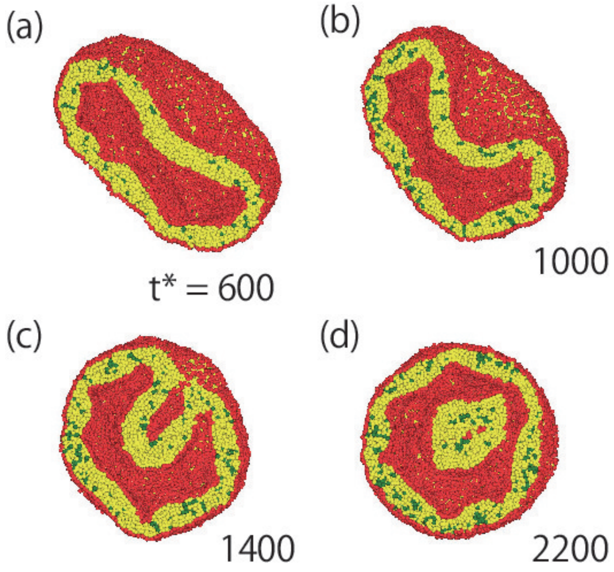

Fig. 3.11: Sequential snapshots of bud formation at $\gamma^*_{\rm sol} = \gamma^*_{\rm TT} = 2$, $p^*_{\rm f} = 20$, $p^*_{\rm r} = 180$, and $\Delta c^* = 3$. Cross-sectional images are shown. The figure is adapted from Fig. 10 in [70].

In order to clarify the relationship between shape transformations and chemical reactions, we calculate the time development of the asphericity $\alpha_{\rm sp}$ [110] (Fig. 3.12(a)), and the amphiphilic molecular number difference, $\Delta N_{\rm amp} = N_{\rm amp,out} - N_{\rm amp,in}$ between the inner and outer leaflets (Fig. 3.12(b)). The asphericity is the degree of deviation from a spherical shape and is defined as $\alpha_{\rm sp} = [(\lambda_1 - \lambda_2)^2 + (\lambda_2 - \lambda_3)^2 + (\lambda_3 - \lambda_1)^2]/2(\lambda_1 + \lambda_2 + \lambda_3)^2$, where λ_1, λ_2, and λ_3 are the eigenvalues of the gyration tensor of the vesicle. It can distinguish the stomatocyte ($\alpha_{\rm sp} \simeq 0$) and the discocyte ($0.15 \lesssim \alpha_{\rm sp} \lesssim 0.25$) [74]. When the chemical reaction process speeds up by increasing $p_{\rm f}$ and $p_{\rm r}$, the shape transformation also speeds up (from $p_{\rm f}^* = 1, p_{\rm r}^* = 9$ to $p_{\rm f}^* = 20, p_{\rm r}^* = 180$ in Fig. 3.12(a)). As the chemical reactions proceed, $\Delta N_{\rm amp}$ linearly decreases in time, but $\alpha_{\rm sp}$ nonlinearly decreases. This rapid change corresponds to the shape transformation from the discocyte to the stomatocyte.

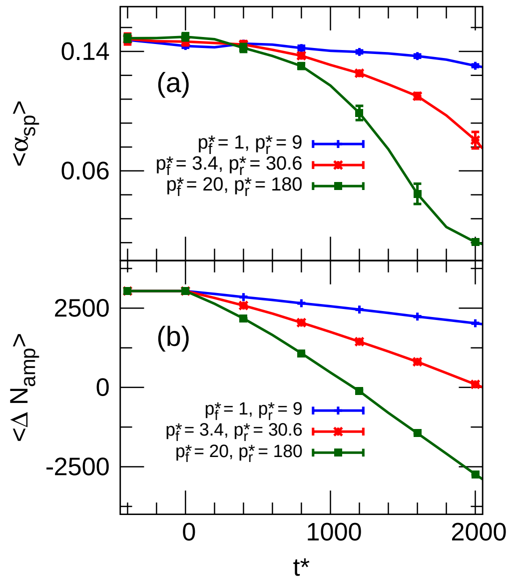

Fig. 3.12: Time development of (a) asphericity $\langle \alpha_{\rm sp} \rangle$, (b) amphiphilic molecular number difference $\langle \Delta N_{\rm amp} \rangle$ between the inner and outer leaflets at $\Delta c^* = 3$, $\gamma_{\rm sol}^* = 24.5$, and $\gamma_{\rm TT}^* = 2$. Symbols are shown for several data points. The error bars are calculated from eight independent runs. The figure is adapted from Fig. 11 in [70].

Interestingly, BP formation without budding occurs when the viscosity $\eta_{\rm sol}$ is increased (see Fig. 3.13). Initially, the bilayer bends inward (Fig. 3.13(b)) as in the budding, but these invaginations transform into BPs (Figs. 3.13(c) and (d)).

In order to distinguish the two types of shape transformations (budding (Fig. 3.11) and BP formation without budding (Fig. 3.13)), we calculate the bilayer thickness inhomogeneous δd during shape transformation from $\alpha_{\rm sp} \simeq 0.14$ to $\alpha_{\rm sp} \simeq 0$ (see Fig. 3.14). For BP formation, δd is diverged when $\alpha_{\rm sp}$ changes from 0.14 to 0.025. For bud formation, δd is not diverged. We set $\delta d_{\rm th} = r_{\rm cut}$ as the threshold value to determine the divergence of the thickness inhomogeneity δd. When $\delta d > \delta d_{\rm th}$

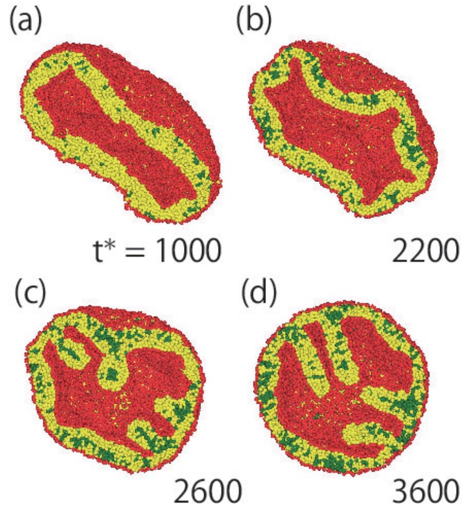

Fig. 3.13: Sequential snapshots of BP formation without budding at $\gamma^*_{\rm sol} = 24.5$, $\gamma^*_{\rm TT} = 2$, $p^*_{\rm f} = 5$, $p^*_{\rm r} = 45$, and $\Delta c^* = 3$. Cross-sectional images are shown. The figure is adapted from Fig. 12 in [70].

is satisfied from $\alpha_{\rm sp} \simeq 0.14$ to $\alpha_{\rm sp} \simeq 0$, this shape transformation is regarded as BP formation.

Using this threshold of δd, we construct the dynamic phase diagram of the shape transformations as shown in Fig. 3.15 for different $\eta_{\rm sol}$ values. At each data point, we carry out eight independent runs. If the number of BP transformations without budding is more than four at one point, the shape transformation is regarded as BP formation without budding.

The shape transformation pathway depends on not only $d\Delta N_{\rm amp}/dt$ but also on $dN_{\rm EO}/dt$ as shown in Fig. 3.15(a). As mentioned in Sec. 3.3.2, BP formation is strongly affected by the spatial distribution of the EOs. If the EOs are not sufficiently synthesized, the resulting shape transformations are budding (low $dN_{\rm EO}/dt$ in Fig. 3.15(a)) because a few EOs do not form clusters in the bilayer. When the EO synthesis rate increases, the EOs self-assemble into clusters in the bilayer, so that BP formation occurs. Thus, EO synthesis dramatically affects the resulting shape transformation.

However, at low viscosity $\eta_{\rm sol}$, BP without budding does not occur, as shown in Fig. 3.15(b). In this case, the bud formation timescale is shorter than the timescale $\tau_{\rm inhomo}$ of the EO cluster formation. The area compressive stress caused by the chemical reactions is released via bud formation before BP formation starts. As pointed out by Sens [95], the surrounding solution that has high viscosity suppresses bud formation. This suppression of bud formation enhances BP formation. As mentioned in Sec. 3.3.1, BP formation is more slowed by the membrane viscosity. Thus, compared to budding, BP formation more frequently occurs at low

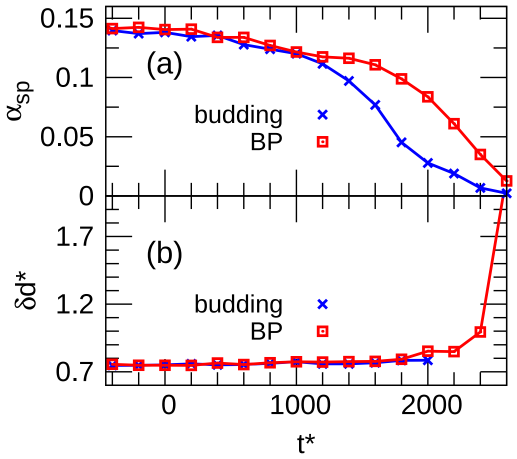

Fig. 3.14: Time development of (a) asphericity α_{sp} and (b) bilayer thickness inhomogeneity δd at $\Delta c^* = 3$, $p_{\mathrm{f}}^* = 5$, $p_{\mathrm{r}}^* = 45$, $\gamma_{\mathrm{sol}}^* = 24.5$, and $\gamma_{\mathrm{TT}}^* = 2$. Blue and red lines represent budding and BP formation without budding, respectively. Symbols are shown for several data points. The figure is adapted from Fig. 13 in [70].

membrane viscosity η_{mb} and high solution viscosity η_{sol}.

3.4 Discussions and Conclusion

In this paper, we have shown the shape transformations of vesicles and flat membranes induced by hydrolysis and condensation reactions. We use the coarse-grained molecular simulation technique in which the hydrolysis and condensation reactions are taken into account explicitly by the bond dissociation and binding. The asymmetric chemical conditions, which are widely observed both *in vitro* and *in vivo*, cause the transport of amphiphiles between outer and inner leaflets, leading to the BP formations. The growth process of BPs strongly depends on the EO density inhomogeneity that is determined by the competition between two different dynamics: diffusion of EOs and synthesis of EOs. At a low reduced volume, budding transformation also occurs. The shape transformation pathway is affected by the EO synthesis rate and the shear viscosity of the surrounding solution. By increasing the solution viscosity η_{sol} while keeping the membrane viscosity η_{mb} constant, bud formation is suppressed so that BP formation is enhanced. In the budding, the membrane mainly moves normal to the membrane surface, but sliding between two leaflets occurs in BP formation. Thus, the viscosity of the surrounding fluids affects budding more than it does BP formation, while the viscosity in the membrane affects BP formation more.

Similar shape transformations in BP formation are observed in the Langmuir

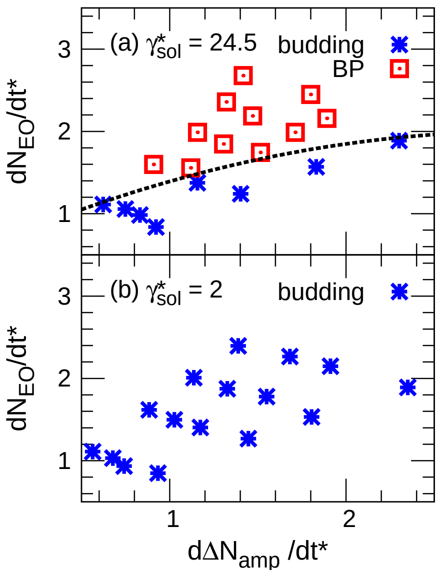

Fig. 3.15: Dynamic phase diagram of shape transformations at (a) $\gamma^*_{\rm sol} = 24.5$ and (b) $\gamma^*_{\rm sol} = 2$ for $\gamma^*_{\rm TT} = 2$. The figure is adapted from Fig. 14 in [70].

monolayer in both experiments [57,62] and simulations [11]. The compression leads to collapse of the Langmuir monolayer into a bilayer sheet. The formed bilayer sheet finally transforms into the spherical vesicle [11, 33], which corresponds to the shape transformation shown in Fig. 3.10. Other experiments, in which bilayer vesicles are composed of SOPC (1-stearoyl-2-oleoyl-sn-glycero-3-phosphocholine), C16:0-SM (N-palmitoyl-sphingomyelin), and Bodipy-sphingomyelin (a fluorescent tracer), show the invagination of vesicle under the injection of the enzyme sphingomyelinase [41]. Ceramide, which is generated by the hydrolysis of SM, segregates into a domain in the membrane and causes the invagination of vesicle. We expect that such a domain helps BP formation in the inner leaflet of the vesicles.

Our results show that the relative viscosity ratio of the membrane and surrounding fluids is significant in determining budding or BP formation. We believe that two competing shape transformations accompanied by lateral and normal membrane motions are generally controlled by the viscosity ratio; the former and latter dynamics are slowed down by increases in viscosities of membrane and surrounding fluids, respectively. Fournier *et al.* [24] reported that higher friction between two leaflets slows down membrane tubulation. Thus, we expect a similar tendency in budding and tubulation. Recently, Fujiwara and Yanagisawa [27, 28] reported that vesicles containing high concentrations of macromolecules undergo bud or tube formation depending on the viscosity of the inner solution; the membrane tube formation appears at the high viscosity, otherwise, bud formation appears. The slow elastic relaxation due to the high viscosity suppresses the bud formations, and enhances the tube formations. We consider that the viscosity ratio of membrane and surrounding fluids is also important in their experiments as well as the viscosity ratio of the inner and outer fluids.

In living cells, lipid droplets are formed on the ER membrane [15]. The hydrophilic segments of the lipids are removed by chemical reactions. These reactions are similar to the hydrolysis reaction in our simulation. The resulting hydrolyzed hydrophobic molecules assemble into clusters in the bilayer membrane. We expect that a similar cluster formation plays a role in the initial lipid droplet formation.

In this work, the rupture of the vesicles is not observed due to the high edge line tension of the bilayer. However, in the experiments conducted by Riske *et al.* [88], the rupture of liposomes occurs as a result of the injection of hydrolase enzyme. The coupling of the asymmetrical amphiphilic molecular density and membrane rupture causes the inside-out inversion [80]. Under low edge tension, competition between ruptures and BP formation may occur.

We only consider amphiphilic molecules that form the bilayer in this dissertation. Hydrolysis reactions removes the hydrophilic head groups of amphiphiles leading to the increase of hydrophobic tail region. This effectively increases the packing parameter of amphiphile. In the experiments by Suzuki *et al.* [107], the molecular assembly changes their shapes from tubular micelles to vesicles due to this packing parameter change by the hydrolysis reactions. In the future, it will be interesting to investigate the molecular mechanism of these shape transformations involving non-bilayer structures.

Appendix

3.A Preparation of vesicles

We prepare the spherical vesicles in the following manner. First, a spherical-cap-shaped bilayer membrane is centered in the simulation box, and water particles are distributed around the bilayer membrane. The system is equilibrated during $500\tau - -2500\tau$. A closed spherical membrane is thus obtained. Some water particles inside the vesicle are then ejected to tune the reduced volume v. After that, the system is equilibrated for 5000τ. For these system equilibrations, we use $\gamma^*_{ij} = 2$ to speed up the equilibration processes. The system is then again equilibrated for 3000τ using the same setting γ_{ij} as for the production runs. After the above-mentioned equilibration processes, we turn on the hydrolysis reaction.

3.B Calculation of thickness of vesicles

We calculate the bilayer thickness d of vesicles from the two layers of the hydrophilic particles. First, we extract the positions of hydrophilic particles in the bilayer membrane. Next, we carry out a clustering analysis using depth-first search with search radius $r_{\mathrm{ds}} = 0.25 r_{\mathrm{cut}}$. Two sets (clusters) of hydrophilic particles are obtained in most cases before the large shape deformations: One is the head-group of the inner leaflet, and the other is the head-group of the outer leaflet. We define the local bilayer thickness as

$$d(i) = \min_{j \in C_{\mathrm{out}}} r_{ij} \, (\mathrm{for}\, i \in C_{\mathrm{in}}), \tag{3.6}$$

where C_{in} and C_{out} are the sets of hydrophilic particles in the inner and outer leaflets, respectively. The membrane thickness d is defined as the mean value of $d(i)$. The thickness inhomogeneity δd defined as

$$\delta d = \sqrt{\frac{1}{n(C_{\mathrm{in}})} \sum_{i \in C_{\mathrm{in}}} (d(i) - d)^2}, \tag{3.7}$$

where $n(C_{\mathrm{in}})$ is the number of particles included in the inner leaflet.

Chapter 4

Nonuniqueness of local pressure of three-body potentials in molecular simulations

In this chapter, we discuss the pressure profile calculation method in molecular simulations and the pressure profile nonuniqueness of the system containing three body potentials.

4.1 Introduction

The stress tensor is a fundamental quantity that connects discrete molecular systems and continuum mechanics. The calculation of the local stress field from molecular simulations has a long history [3–6, 32, 36, 38, 49, 79, 92, 111–113, 118]. Irving and Kirkwood introduced the microscopic stress tensor formula based on non-equilibrium statistical mechanics [49], following which a rigorous mathematical formula was proposed by Noll [79]. In the following, we refer to their procedure as the Irving-Kirkwood-Noll (IKN) procedure, as stated by Admal and Tadmor [6]. Hardy introduced the spatial averaging of the stress tensor using weighting functions to improve statistics [36]. However, these procedures are limited to systems in which interactions consist of pairwise forces.

The method to map the stress of multibody potentials into the continuum space has been debated. Multibody potentials have been frequently used in molecular simulations. Bending and dihedral potentials, which are widely used, are three- and four-body potentials, respectively. The interaction between adjacent dihedrals is represented by five-body correction map (CMAP) potential in the CHARMM force field [65, 112]. A curvature potential in meshless membranes is a function of three rotational invariants of the weighted gyration tensor and produces n-body forces, where n depends on the local density [75]. Since most of the multibody forces are not central forces between particles, the IKN procedure cannot be directly applied to them. Note that multibody hydrophobic potentials as a function of the local hydrophobic particle density for proteins [108] and membranes [75,78] give central forces between particles so that their stress can be calculated directly using the IKN procedure.

Goetz and Lipowsky proposed a decomposition procedure for multibody potentials [32] based on Schofield and Henderson's procedure [92]. Multibody forces are decomposed into pairwise (non-central) forces, and the IKN procedure is applied to each decomposed force pair. We refer to this method as Goetz-Lipowsky decomposition (GLD). However, GLD does not satisfy the strong law of action and reaction, as pointed out by Admal and Tadmor [3,6], while it satisfies the weak law of action and reaction: GLD conserves translational momentum but not angular momentum. Consequently, the stress tensor is not symmetric. To overcome this problem, central force decomposition (CFD) was proposed [3,5,6,112,118]. The forces decomposed using CFD satisfy the strong law of action and reaction so that the stress tensor is symmetric by construction. The original CFD is limited to three- or four-body forces because there exists a unique force decomposition for only up to four-body forces. For n-body forces with $n \geq 5$, the number of degrees of freedom $3n-6$ is less than the number of pairs $n(n-1)/2$ in the three-dimensional (3D) space. Very recently, the generalization to more than four-body forces, which is called a covariant CFD (cCFD), was introduced by Torres-Sánchez *et al.* [112,113]. The application to a structural coiled-coil protein with the five-body CMAP potential was demonstrated [112].

In this chapter, we discuss non-uniqueness in the force decomposition of three-body forces in classical mechanics. Three-body forces can be uniquely decomposed by CFD. However, we will show different decompositions, which also satisfy the strong law of action and reaction. A force center can be uniquely defined for three-body forces, and the forces are decomposed into central force pairs between interacting particles and the force center. To combine this decomposition and CFD, the position of the force center can be arbitrarily taken. This non-uniqueness is related with the non-unique potential-energy extension discussed in Ref. [3,4,6]. It is a specific case of the degeneracy of four-body forces into 2D space. We will discuss the choice of this center position by the stress distribution. Although two-body forces can also similarly be decomposed, the IKN procedure always gives the minimum stress distribution. In contrast, the stress distribution of three-body forces depends on the type of the forces. We will also discuss the influence of the resolution of simulation models.

For an application of the force decomposition, we investigated a bilayer membrane using coarse-grained and atomistic molecular dynamics (MD) simulations. The stress profile along the normal direction has been widely calculated in the molecular simulations of lipid membranes. Two opposing forces, interfacial tension and steric repulsion, produce the inhomogeneous stress inside the bilayers [50]. This inhomogeneity is a key property of the bilayers because it determines the area per lipid molecule [50], spontaneous curvature [46, 82, 83, 89, 119], Gaussian curvature modulus [40, 45, 46, 82, 83, 90, 103, 119], and function of the mechanosensitive channel [105, 116]. Since the stress profile cannot be obtained experimentally [25, 109], estimation using molecular simulations is important. Recently, however, Torres-Sánchez *et al.* reported that the stress profile is strongly dependent on the force decomposition method [112]. The dihedral forces give the largest contribution to the stress profile by CFD. We will show that the stress profile is largely dependent on the decomposition of bending forces.

In Sec. 4.2, we discuss the force decomposition method. After introducing the existing decomposition method, we describe the alternative decomposition method for three-body forces. As an example, we show the decomposition for an area potential and a bending potential. The area potential is one of the simplest three-body potentials and is connected to continuum mechanics in a straightforward manner. The bending potential is the most widely used three-body potential. In Sec. 4.3, the bilayer membrane is examined. The stress profile and Gaussian curvature modulus are calculated for different decomposition methods. The discussion and summary are given in Sec. 4.4 and 4.5, respectively.

4.2 Force Decomposition

4.2.1 Irving-Kirkwood-Noll Procedure

Stress averaged over the entire simulation box is given by the virial as

$$\begin{aligned}
\boldsymbol{\sigma} &= \boldsymbol{\sigma}_{\mathrm{K}} + \boldsymbol{\sigma}_{\mathrm{U}}, && (4.1)\\
\boldsymbol{\sigma}_{\mathrm{K}} &= -\frac{1}{V}\sum_i \langle m_i \mathbf{v}_i \otimes \mathbf{v}_i \rangle, && (4.2)\\
\boldsymbol{\sigma}_{\mathrm{U}} &= -\frac{1}{V}\sum_i \langle \mathbf{f}_i \otimes \mathbf{r}_i \rangle, && (4.3)\\
&= \frac{1}{V}\sum_{n=2}^{N}\sum_{k_n=1}\sum_{i=1}^{n}\langle \frac{\partial U_{k_n}}{\partial \mathbf{r}_{k_n,i}} \otimes (\mathbf{r}_i - \mathbf{r}_{k_n,0})\rangle, && (4.4)
\end{aligned}$$

where m_i, $\mathbf{r}_i$, and $\mathbf{v}_i$ are the mass, position, and velocity of the i-th particle and $\mathbf{f}_i = -\partial U/\partial \mathbf{r}_i$. The symbol $\otimes$ denotes a tensor product and $\langle ... \rangle$ denotes a statistical average. This global stress is uniquely determined even for multibody forces. The potential contribution $\boldsymbol{\sigma}_{\mathrm{U}}$ can be rewritten with Eq. (4.4) using cluster expansion [113] as

$$U(\mathbf{r}_1, ..., \mathbf{r}_N) = \sum_{n=2}^{N} \sum_{k_n=1} U_{k_n}(\mathbf{r}_{k_n,1}, ..., \mathbf{r}_{k_n,n}), \tag{4.5}$$

where each U_{k_n} is an n-body potential that is invariant under translation and rotation. The origin $\mathbf{r}_{k_n,0}$ of the positions can be taken differently for each U_{k_n}, as expressed in Eq. (4.4). Each origin can be arbitrarily chosen but a position close to interacting particles is preferred to reduce numerical errors, particularly for large-scale simulations. When the origin is set to the position of one of the interacting particles, the potential stress of the pairwise potentials takes the well-known form,

$$\boldsymbol{\sigma}_{\mathrm{U,pair}} = -\frac{1}{V} \sum_{i<j} \langle f_{ij} \hat{\mathbf{r}}_{ij} \otimes \mathbf{r}_{ij} \rangle, \tag{4.6}$$

where $f_{ij} = -\partial U_{\mathrm{k}_2}/\partial r_{ij}$, $\mathbf{r}_{ij} = \mathbf{r}_i - \mathbf{r}_j$, $r_{ij} = |\mathbf{r}_{ij}|$, and $\hat{\mathbf{r}}_{ij} = \mathbf{r}_{ij}/r_{ij}$. Under a periodic boundary condition, the periodic image is used instead of the original position when the potential interaction crosses the periodic boundary.

For pairwise interactions, the local stress at a position $\mathbf{x}$ is given by the IKN procedure as [49, 79]

$$\begin{aligned}
\boldsymbol{\sigma}(\mathbf{x}) &= \boldsymbol{\sigma}_{\mathrm{K}}(\mathbf{x}) + \boldsymbol{\sigma}_{\mathrm{U}}(\mathbf{x}), && (4.7)\\
\boldsymbol{\sigma}_{\mathrm{K}}(\mathbf{x}) &= -\sum_{i} \langle m_i \mathbf{v}_i \otimes \mathbf{v}_i \delta(\mathbf{r}_i - \mathbf{x}) \rangle, && (4.8)\\
\boldsymbol{\sigma}_{\mathrm{U}}(\mathbf{x}) &= -\sum_{i<j} \langle f_{ij} \hat{\mathbf{r}}_{ij} \otimes \mathbf{r}_{ij} B_{\mathrm{IKN}}(\mathbf{r}_i, \mathbf{r}_j, \mathbf{x}) \rangle, && (4.9)
\end{aligned}$$

where $B_{\mathrm{IKN}}(\mathbf{r}_i, \mathbf{r}_j, \mathbf{x}) = \int_0^1 \delta[(1-s)\mathbf{r}_i + s\mathbf{r}_j - \mathbf{x}]ds$. The force propagates along the line segment between $\mathbf{r}_i$ and $\mathbf{r}_j$. This local stress tensor is symmetric: $\sigma_{\alpha\beta}(\mathbf{x}) = \sigma_{\beta\alpha}(\mathbf{x})$ for $\alpha, \beta \in \{x, y, z\}$.

4.2.2 Central Force and Geometric-Center Decompositions

When the multibody force is decomposed into pairwise forces between interacting particles, the IKN procedure for pairwise forces is applicable. Therefore, decomposition methods to pairwise forces have been focused upon. Goetz and Lipowsky proposed a decomposition (GLD), $\mathbf{f}_{ij} = (\mathbf{f}_i - \mathbf{f}_j)/n$, for n-body forces [32]. This decomposition conserves the translational momentum but does not conserve the angular momentum, since the force $\mathbf{f}_{ij}$ is not generally parallel to $\mathbf{r}_{ij}$.

In order to satisfy the conservation of the angular momentum as well, Admal and Tadmor proposed the decomposition to central forces between interacting particles (CFD) [3,6]. Three-body forces can be uniquely decomposed by CFD:

$$\begin{aligned} \mathbf{f}_1 &= f_{12}\hat{\mathbf{r}}_{12} + f_{13}\hat{\mathbf{r}}_{13}, \\ \mathbf{f}_2 &= f_{23}\hat{\mathbf{r}}_{23} + f_{12}\hat{\mathbf{r}}_{21}, \\ \mathbf{f}_3 &= f_{13}\hat{\mathbf{r}}_{31} + f_{23}\hat{\mathbf{r}}_{32}. \end{aligned} \tag{4.10}$$

Since the translational and angular momenta are conserved, $\mathbf{f}_1 + \mathbf{f}_2 + \mathbf{f}_3 = \mathbf{0}$ and $\mathbf{f}_1 \times \mathbf{r}_1 + \mathbf{f}_2 \times \mathbf{r}_2 + \mathbf{f}_3 \times \mathbf{r}_3 = \mathbf{0}$. For $f_{12} > 0$, f_{12} is a repulsive force between $\mathbf{r}_1$ and $\mathbf{r}_2$. From Eq. (4.10), f_{12} is given by

$$f_{12} = \frac{\mathbf{f}_1 \cdot \hat{\mathbf{r}}_{12} - (\mathbf{f}_1 \cdot \hat{\mathbf{r}}_{13})(\hat{\mathbf{r}}_{12} \cdot \hat{\mathbf{r}}_{13})}{1 - (\hat{\mathbf{r}}_{12} \cdot \hat{\mathbf{r}}_{13})^2}, \tag{4.11}$$

or

$$f_{12} = \frac{1}{2}\Big(\frac{\mathbf{f}_1 \cdot (\hat{\mathbf{r}}_{12} + \hat{\mathbf{r}}_{13})}{1 + \hat{\mathbf{r}}_{12} \cdot \hat{\mathbf{r}}_{13}} + \frac{\mathbf{f}_2 \cdot (\hat{\mathbf{r}}_{23} + \hat{\mathbf{r}}_{21})}{1 + \hat{\mathbf{r}}_{21} \cdot \hat{\mathbf{r}}_{23}} - \frac{\mathbf{f}_3 \cdot (\hat{\mathbf{r}}_{31} + \hat{\mathbf{r}}_{32})}{1 + \hat{\mathbf{r}}_{31} \cdot \hat{\mathbf{r}}_{32}}\Big). \tag{4.12}$$

Similarly, f_{13} and f_{23} are given. Equation (4.12) is recommended for numerical calculations, since it gives smaller numerical errors when two angles of $\triangle 123$ are close to null and the third is close to π. Alternatively, these force pairs can be derived directly from $f_{12} = -\partial U_{k3}/\partial r_{12}|r_{13}, r_{23}$ [6] as demonstrated for the area and bending potentials in Appendix 4.A and 4.B, respectively. The CFDs of the area expansion and bending forces are shown in Figs. 4.1(b) and 4.2(b), respectively. The three interacting particles form a triangle and lie on a plane so that the forces $\mathbf{f}_1$, $\mathbf{f}_2$, and $\mathbf{f}_3$ are along this plane owing to the conservation of translational and angular momenta. Hence, we can consider the 2D space without loss of generality.

Alternatively, Heinz *et al.* proposed a decomposition method that uses the geometric center, $\sum_i^{n'} \mathbf{r}_i/n'$, of n' interacting particles in a divided cell for an n-body potential ($n' < n$) [38]. In this decomposition, the angular momentum is not conserved. The geometric center is determined only by the positions and has no relation to the force balance. Hence, the geometric center can significantly deviate from the positions where the forces act. For example, when great forces act only on two particles in n-body forces, *i.e.*, $|\mathbf{f}_i| \gg |\mathbf{f}_j|$ ($i = 1$, 2, and $j \geq 3$), the resultant stress should be close to that of the pairwise forces between $\mathbf{r}_1$ and $\mathbf{r}_2$. However, the geometric center can be far from the line segment between $\mathbf{r}_1$ and $\mathbf{r}_2$. Thus, a center position should be determined by the force balance, or a specific force decomposition should be employed for a chosen center position to satisfy the force balance. We consider the center position with the decomposition to satisfy the strong law of the action and reaction in Sec. 4.2.3.

One may consider the center of mass as an alternative candidate for the center position. However, the potential stress term $\boldsymbol{\sigma}_U$ is not dependent on mass distribution in thermal equilibrium. One can calculate $\boldsymbol{\sigma}_U$ using a Monte Carlo simulation, in which the mass distribution is not required at all. Since the values

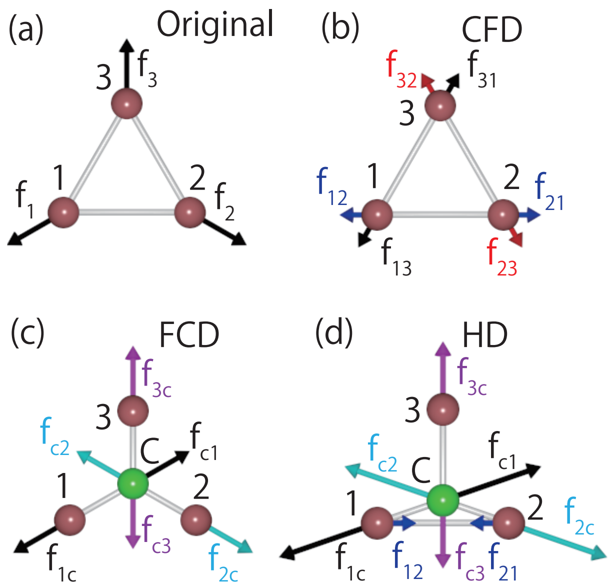

Fig. 4.1: Force decomposition for area expansion forces. (a) Original forces. (b) CFD. (c) FCD. (d) HD. The light gray (green) sphere represents the force center, $\mathbf{r}_c$. The figure is adapted from Fig. 1 in [69].

of the particle masses are arbitrary but positive, the center of mass lies inside the convex polyhedron (triangle for three-body forces) formed by interacting particles. As described below, it is important whether the center position for force decomposition is inside or outside the triangle for three-body forces.

4.2.3 Force Center and Hybrid Decompositions

We consider the alternative decompositions of three-body forces. As mentioned above, the forces are uniquely determined by CFD for three-body forces. However, when one more position is taken into account, the forces are not uniquely determined. For three-body forces, three lines drawn along the force vectors $\mathbf{f}_i$ from the particle positions $\mathbf{r}_i$ ($i \in 1, 2, 3$) always meet at one position owing to the angular-momentum conservation[1]. We refer to this position as the force center, $\mathbf{r}_c$. It is determined as

$$\mathbf{r}_c = \frac{1}{q}\left(\tilde{f}_{12}\tilde{f}_{13}\mathbf{r}_1 + \tilde{f}_{12}\tilde{f}_{23}\mathbf{r}_2 + \tilde{f}_{13}\tilde{f}_{23}\mathbf{r}_3\right) \tag{4.13}$$

$$q = \tilde{f}_{12}\tilde{f}_{13} + \tilde{f}_{12}\tilde{f}_{23} + \tilde{f}_{13}\tilde{f}_{23} \tag{4.14}$$

where $\tilde{f}_{ij} = f_{ij}/r_{ij}$ and f_{ij} are the forces obtained by CFD. The sign of the denominator q determines the region of the force center as described later. Using

---

[1] This is not true for n-body forces ($n \geq 4$).

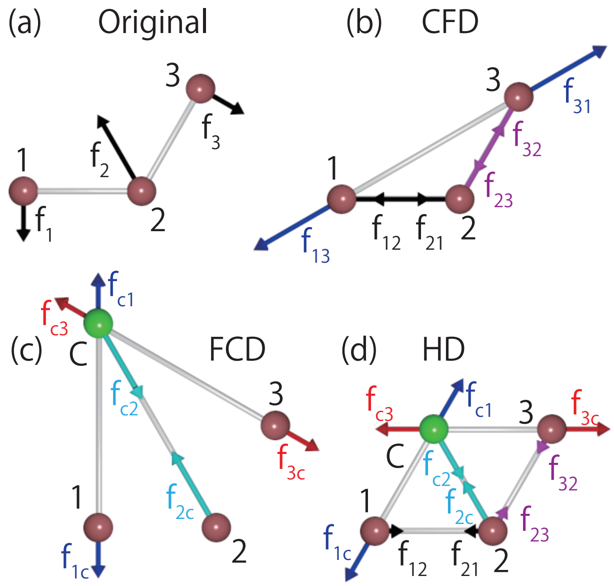

Fig. 4.2: Force decomposition for bending forces on θ_{123}. (a) Original forces. (b) CFD. (c) FCD. (d) HD. The same color notation as Fig. 4.1 is employed. The figure is adapted from Fig. 2 in [69].

the force center, the forces are decomposed into three central force pairs $f_{ic}\hat{\mathbf{r}}_{ic} = \mathbf{f}_i$ between $\mathbf{r}_i$ and $\mathbf{r}_c$ for $i \in \{1, 2, 3\}$ [see Figs. 4.1(c) and 4.2(c)]. We refer to this decomposition as force-center decomposition (FCD). Since these are central forces, the strong law of action and reaction is satisfied and the symmetric local stress tensor is obtained by the IKN procedure for these decomposed forces.

When three force pairs have the same sign ($f_{12} > 0$, $f_{13} > 0$, $f_{23} > 0$ or $f_{12} < 0$, $f_{13} < 0$, $f_{23} < 0$), the force center lies in the interior region of the triangle $\triangle 123$ and $q > 0$. For an expansion force as shown in Fig. 4.1, the decomposed forces in CFD and FCD can be physically interpreted as line (surface) tension on the edge of the triangular region and pressure of the interior region on the particles, respectively.

The exterior region can be divided into six regions as shown in Fig. 4.3. When $f_{12}f_{13} > 0$ and $f_{12}f_{23} < 0$, the force center lies in the region A or D for $q > 0$ or $q < 0$, respectively. For bending potentials as a function of the angle $\theta_{123} = \cos^{-1}(\hat{\mathbf{r}}_{12} \cdot \hat{\mathbf{r}}_{32})$, $\mathbf{r}_c$ always lies outside the triangle and $q < 0$. As θ_{123} becomes closer to π, $\mathbf{f}_1$ and $\mathbf{f}_3$ approach parallel lines so that $\mathbf{r}_c$ becomes further from the particle positions. The details of decomposition for the area and bending potentials are described in Appendix 4.A and 4.B, respectively.

The force center position can be moved by combining FCD with CFD. We refer to this combined decomposition as hybrid decomposition (HD). If necessary to distinguish them, the force center in FCD is called the original force center

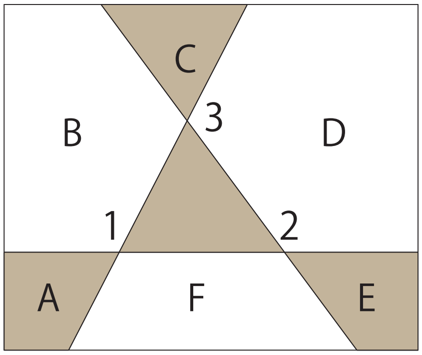

Fig. 4.3: Six exterior regions (A–F) of the triangle △123. Shaded and white regions correspond to $q > 0$ and $q < 0$, respectively. The figure is adapted from Fig. 3 in [69].

$\mathbf{r}_{c0}$. In HD, the force pair of each edge of △123 is divided into FCD and CFD components as $f_{12}^{\mathrm{all}} = f_{12}^{\mathrm{FC}} + f_{12}^{\mathrm{CF}}$. The force center $\mathbf{r}_c$ is determined by Eq. (4.13) with the FCD components $f_{12}^{\mathrm{FC}}, f_{13}^{\mathrm{FC}}$, and f_{23}^{FC}. For example, Fig. 4.1(d) shows the decomposition into three force pairs with $\mathbf{r}_c$ and one force pair along $\mathbf{r}_{12}$. When the contribution of force f_{12} to FCD increases (decreases), the hybrid force center $\mathbf{r}_c$ is further (closer) to $\mathbf{r}_3$ than the original force center $\mathbf{r}_{c0}$ [see Eq. (4.13)]. Figure 4.2(d) shows HD combining FCD with two force pairs along $\mathbf{r}_{12}$ and $\mathbf{r}_{23}$. If the force center lies on the edge of the triangle △123, the resultant decomposition coincides with CFD (if $\mathbf{r}_c$ lies in the middle of the line segment between $\mathbf{r}_2$ and $\mathbf{r}_3$, then $f_{1c} = 0$).

The hybrid decomposition can be applied to two-body forces if two positions, $\mathbf{r}_3$ and $\mathbf{r}_4$, are added as shown in Fig. 4.4. Therefore, the IKN procedure is not a unique solution to obtain the stress tensor even for the two-body forces. However, the total length ($\ell_{\mathrm{sum}} = \sum_{i<j} r_{ij}$) and force norm sum ($f_{\mathrm{sum}} = \sum_{i<j} |f_{ij}|$) become greater than the IKN procedure. Thus, the IKN procedure is the best decomposition method for two-body forces.

4.2.4 Stress Distribution

Although the force center can be set to an arbitrary position in HD, positions that are excessively far away are not physically suitable. Thus, we need a criterion to select the decomposition. We consider the minimization of the stress distribution as a candidate criterion. Hence, we define the stress-distribution magnitude Γ_{SDM} as a summation over the cross norm of the stress,

$$\Gamma_{\mathrm{SDM}} = \sum_{i<j} |f_{ij}| r_{ij}, \tag{4.15}$$

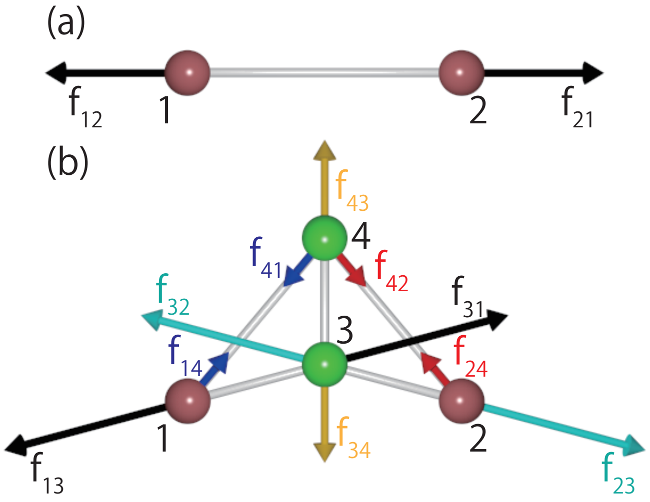

Fig. 4.4: Force decomposition for two-body forces. (a) Original forces. (b) Example of the hybrid decompositions.

where the summation is taken over all pairs ($i, j \in 1, 2, 3, c$ for the three-body forces). For the two-body forces, the IKN procedure always gives the minimum value of Γ_{SDM}. Therefore, Γ_{SDM} can be employed as the criterion for the two-body forces.

In the following, we consider the minimization problem of Γ_{SDM} for three-body forces. For CFD and FCD, $\Gamma_{\mathrm{CFD}} = |f_{12}|r_{12} + |f_{13}|r_{13} + |f_{23}|r_{23}$ and $\Gamma_{\mathrm{FCD}} = |f_{1c}|r_{1c} + |f_{2c}|r_{2c} + |f_{3c}|r_{3c}$, respectively. Interestingly, when the original force center exists in the interior region of the triangle $\triangle 123$, these two magnitudes take the same value: $\Gamma_{\mathrm{CFD}} = \Gamma_{\mathrm{FCD}}$. The force norm sum f_{sum} of CFD is less than that of FCD, while the total length ℓ_{sum} of CFD is greater. For HD with $\mathbf{r}_c$ lying in the interior region of $\triangle 123$,

$$\begin{aligned}
\Gamma_{\mathrm{HD}} &= \Gamma^{\mathrm{FC}}_{\mathrm{HD}} + \Gamma^{\mathrm{CF}}_{\mathrm{HD}} && (4.16)\\
&= (|f^{\mathrm{FC}}_{12}| + |f^{\mathrm{CF}}_{12}|)r_{12} + (|f^{\mathrm{FC}}_{13}| + |f^{\mathrm{CF}}_{13}|)r_{13} \\
&\quad +(|f^{\mathrm{FC}}_{23}| + |f^{\mathrm{CF}}_{23}|)r_{23}. && (4.17)
\end{aligned}$$

When the CFD and FCD components in each force pair have the same sign, *i.e.*, when $f^{\mathrm{CF}}_{12} f^{\mathrm{FC}}_{12} > 0$, $|f^{\mathrm{all}}_{12}| = |f^{\mathrm{CF}}_{12}| + |f^{\mathrm{FC}}_{12}|$ so that $\Gamma_{\mathrm{HD}} = \Gamma_{\mathrm{CFD}}$. When $f^{\mathrm{CF}}_{12} f^{\mathrm{FC}}_{12} < 0$, $|f^{\mathrm{all}}_{12}| < |f^{\mathrm{CF}}_{12}| + |f^{\mathrm{FC}}_{12}|$ so that $\Gamma_{\mathrm{HD}} > \Gamma_{\mathrm{CFD}}$. For the hybrid force center inside the triangle $\triangle 123$, the decomposition with the same sign for each force pair can be chosen. Thus, when $\mathbf{r}_c$ exists inside or on the edge of $\triangle 123$, Γ_{SDM} takes the minimum value $\Gamma_{\mathrm{CFD}} = \Gamma_{\mathrm{FCD}}$. Figure 4.5 shows the minimum value of Γ_{SDM} for each force center position $\mathbf{r}_c$ for an area potential. Here, HD into three FCD force pairs and two CFD force pairs is used ($f^{\mathrm{CF}}_{12} = 0$, $f^{\mathrm{CF}}_{13} = 0$, or $f^{\mathrm{CF}}_{23} = 0$), since

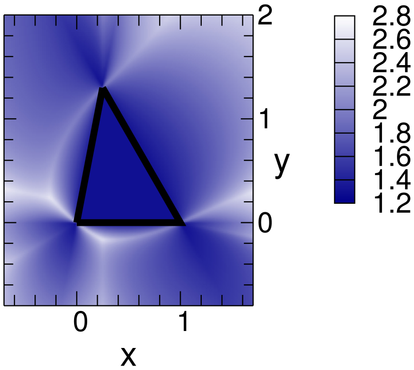

Fig. 4.5: Contour map of the stress distribution magnitude Γ_{SDM} with respect to the force center position $\mathbf{r}_c(x, y)$ for the surface tension $k_{\mathrm{ar}} A_{123}$. The color bar shows the magnitude of $\Gamma_{\mathrm{SDM}}/k_{\mathrm{ar}}$. The figure is adapted from Fig. 5 in [69].

infinitely small values can be taken for all FCD pairs if all six force pairs are allowed. For $\mathbf{r}_c$ lying in the interior region of $\triangle 123$, Γ_{SDM} is constant, while Γ_{SDM} is greater for $\mathbf{r}_c$ lying in the exterior region. Therefore, the Γ_{SDM} minimization implies the restriction on the decomposition choices to the interior region but does not give a unique combination.

When the original force center $\mathbf{r}_{c0}$ exists outside the triangle, Γ_{SDM} typically has the lowest value at a single position of $\mathbf{r}_c$. Figure 4.6 shows a typical example of Γ_{SDM} in the HD of a bending potential on θ_{123} with $f_{13}^{\mathrm{CF}} = 0$. The deepest minimum of Γ_{SDM} appears between $\mathbf{r}_{c0}$ and the triangle $\triangle 123$ and local minima appear in the other exterior regions. We consider the case where $\mathbf{r}_{c0}$ lies in the region B, as shown in Fig. 4.3. We define the position $\mathbf{r}_{\mathrm{m}}$, which is geometrically determined:

$$\begin{aligned} \mathbf{r}_{\mathrm{m}} &= \mathbf{r}_2 + \sqrt{r_{12} r_{23}}\,\hat{\mathbf{r}}_{\mathrm{bv}}, \\ \hat{\mathbf{r}}_{\mathrm{bv}} &= \frac{\hat{\mathbf{r}}_{12} + \hat{\mathbf{r}}_{32}}{|\hat{\mathbf{r}}_{12} + \hat{\mathbf{r}}_{32}|}, \end{aligned} \tag{4.18}$$

where $\hat{\mathbf{r}}_{\mathrm{bv}}$ is a unit vector bisecting the angle θ_{123}. The triangles $\triangle 12\mathrm{m}$ and $\triangle \mathrm{m}23$ are similar. When $\mathbf{r}_{\mathrm{m}}$ is in the interior or on the edges of the triangle $\triangle 13c0$ formed by $\mathbf{r}_1$, $\mathbf{r}_3$, and $\mathbf{r}_{c0}$, Γ_{SDM} has the global minimum at $\mathbf{r}_c = \mathbf{r}_{\mathrm{m}}$, where HD is taken for five force pairs, f_{12}^{CF}, f_{23}^{CF}, f_{1m}, f_{2m}, and f_{3m}. This minimum appears not only for the bending forces but also for the other three-body forces with $\mathbf{r}_{c0}$ lying in the region B. The local minimum in the region E with $f_{13}^{\mathrm{CF}} = 0$ appears at $\mathbf{r}_{\mathrm{lm}} = \mathbf{r}_2 - \sqrt{r_{12} r_{23}}\,\hat{\mathbf{r}}_{\mathrm{bv}}$. The derivations of these global and local minima are described in Appendix 4.C. The stress cross norms are balanced at $\mathbf{r}_{\mathrm{m}}$: $|f_{1m}| r_{1\mathrm{m}} = |f_{2m}| r_{2\mathrm{m}} = |f_{3m}| r_{3\mathrm{m}}$. For the bending forces, the condition for $\mathbf{r}_{\mathrm{m}}$ lying in $\triangle 13c0$ is $r_{12}/r_{23} \geq \cos^2(\theta_{123}/2)$ and $r_{23}/r_{12} \geq \cos^2(\theta_{123}/2)$. This condition is satisfied in

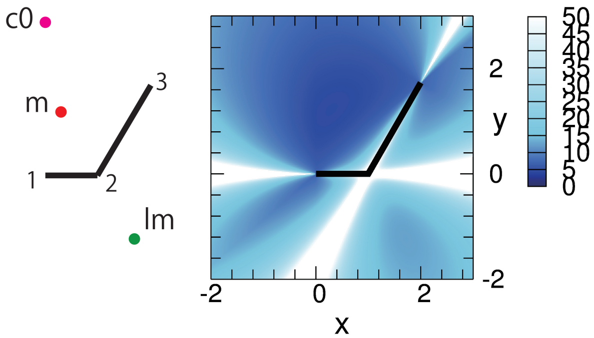

Fig. 4.6: Contour map of the stress distribution magnitude Γ_{SDM} with respect to the force center position $\mathbf{r}_c(x, y)$ for the bending potential in Eq. (4.19). The color bar shows $\Gamma_{\mathrm{SDM}}/k_{\mathrm{bend}}$. The positions of the original force center $\mathbf{r}_{c0}$ and the force centers $\mathbf{r}_{\mathrm{m}}$ and $\mathbf{r}_{\mathrm{lm}}$ of the global and local minima of Γ_{SDM} are shown in the left panel. The figure is adapted from Fig. 6 in [69].

	W	H	T
W	25	25	200
H	25	25	200
T	200	200	25

Table 4.1: Repulsive interaction parameters a_{ij} with unit $k_{\mathrm{B}}T$.

typical simulation conditions including our present simulation. It is violated only when r_{12}/r_{23} significantly deviates from unity and θ_{123} is small.

For general three-body forces, $\mathbf{r}_{\mathrm{m}}$ can be outside $\triangle 13c0$. In this case, we do not have an analytical solution for the Γ_{SDM} minimum, but it can be calculated numerically. In the next section, we investigate how the stress profile of a bilayer membrane depends on the decomposition.

4.3 Bilayer membrane

We simulate a tensionless bilayer membrane with various decompositions of bending forces using coarse-grained and atomistic lipid models. In Sec. 4.3.1, the stress profile and Gaussian curvature modulus are discussed using the dissipative particle dynamics (DPD) method [22, 35, 43, 120]. DPD is one of the widely used coarse-grained lipid models. In Sec. 4.3.2, the stress profile of an atomistic MD of DOPC (1,2-Dioleoyl-sn-glycero-3-phosphocholine) using CHARMM36 force field [52, 53] is discussed. We refer to HD with the global and local minima of Γ_{SDM} in the regions B and E as HD(GM) and HD(LM), respectively. In HD, we examine only the case $f_{13}^{\mathrm{CF}} = 0$, since HD(GM) and HD(LM) are obtained in this condition.

4.3.1 Coarse-grained model

Model description

Basic concepts of DPD is described in Chapter 2. We briefly show the parameter settings of simulation model in the following.

An amphiphilic molecule is represented by a linear chain of four particles: one hydrophilic (H) and three hydrophobic (T) DPD particles. Neighboring DPD particles are connected via the harmonic bond potential, $U_{\mathrm{bond}}(r_{ij}) = (k_{\mathrm{bond}}/2)(1-r_{ij}/\ell_0)^2$, with $k_{\mathrm{bond}} = 150k_{\mathrm{B}}T$, where $k_{\mathrm{B}}T$ is the thermal energy. One of the simplest bending potentials is employed at the second and third particles of the amphiphile:

$$U_{\mathrm{bend}}(\theta_{ijk}) = k_{\mathrm{bend}}(1 - \cos\theta_{ijk}), \tag{4.19}$$

with $k_{\mathrm{bend}} = 30k_{\mathrm{B}}T$. A dihedral potential is not considered. The multi-time-step algorithm [76, 115] is employed with $\Delta t = 0.005\tau$ and $\delta t = 0.05\tau$,where $\tau = r_{\mathrm{cut}}\sqrt{m/k_{\mathrm{B}}T}$.

All particle pairs interact through a soft repulsive potential: $U_{\mathrm{rep}}(r_{ij}) = (a_{ij}/2)(1-r_{ij}/r_{\mathrm{cut}})^2$, which vanishes beyond the cutoff at $r_{ij} = r_{\mathrm{cut}}$. We set $r_{\mathrm{cut}} = 2\ell_0$ in this study. The repulsive interaction parameters, a_{ij}, are listed in Table 4.1. $\gamma = 4.5\sqrt{k_{\mathrm{B}}Tm}/r_{\mathrm{cut}}$, $p = 1$ are used for the dissipative and random force parameters.

The amphiphilic molecules form a bilayer membrane with the bending rigidity $\kappa/k_{\mathrm{B}}T = 18.3 \pm 0.2$, which is a typical value for a bilayer membrane at room temperature [59]. The details of the simulation method are described in Appendix 4.D.1.

Lateral pressure profile

The lateral and normal pressure profiles along the normal (z) direction of the bilayer membrane for different force decomposition methods are shown in Fig. 4.7. The pressure profiles are calculated from the average stress for small slices along the xy plane with a width of $\Delta z = 0.2\ell_0$: $P_{\mathrm{L}}(z) = -(\sigma_{xx}(z) + \sigma_{yy}(z))/2$ and $P_{\mathrm{N}}(z) = -\sigma_{zz}(z)$. The lateral profile $P_{\mathrm{L}}(z)$ strongly depends on the force decomposition methods, while the normal profile $P_{\mathrm{N}}(z)$ is independent of the decompositions and takes a constant value. The contribution of two-body forces to $P_{\mathrm{L}}(z)$ is only slightly dependent on z [see Fig. 4.7(a)].

The contribution $P_{\mathrm{L}}^{\mathrm{bend}}$ of the bending forces to the lateral profile is significantly different for different decomposition methods. The amplitude of $P_{\mathrm{L}}^{\mathrm{bend}}$ of FCD is much larger than those of CFD, HD(GM), and HD(LM), as shown in Fig. 4.7(b).

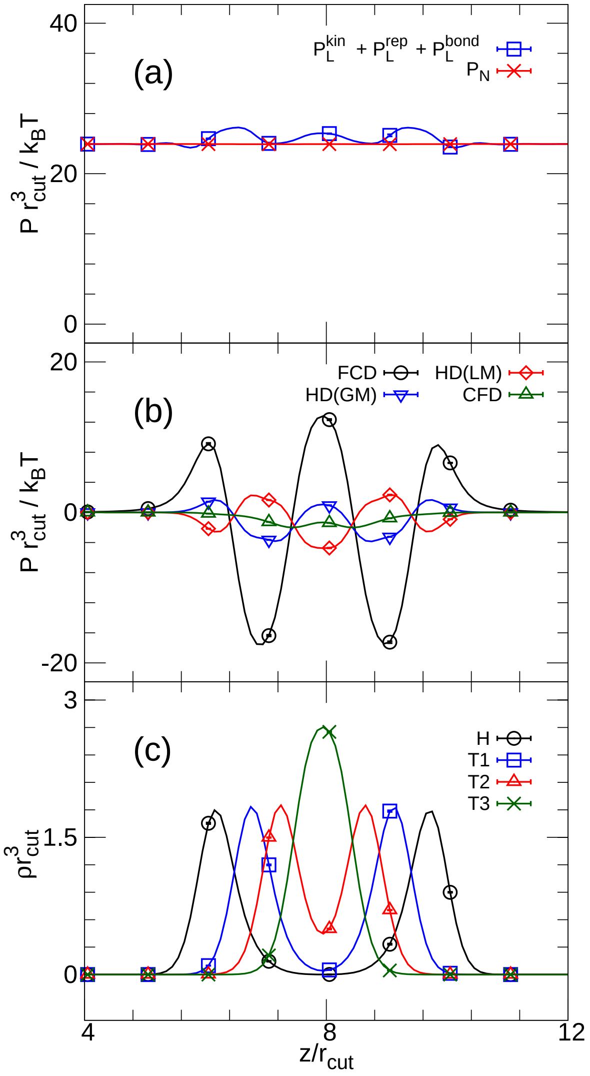

Fig. 4.7: Pressure and density profiles along bilayer normal (z) axis obtained by the DPD simulation. (a) Total normal pressure profile $P_{\mathrm{N}}(z)$ and partial lateral pressure profile $P_{\mathrm{L}}(z)$ given by the sum of three contributions of the kinetic, repulsive, and bond potential components. (b) Lateral pressure profile $P_{\mathrm{L}}^{\mathrm{bend}}(z)$ given by bending potential stress with four decomposition methods. (c) Number density profile of four particles in the amphiphilic molecules. H represents the first (hydrophilic head) particle. T1, T2, and T3 represent three hydrophobic particles. The symbols and error bars are shown at several data points. The figure is adapted from Fig. 7 in [69].

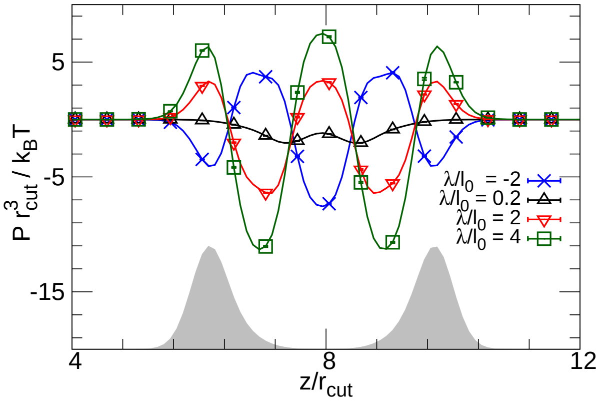

Fig. 4.8: Length λ dependence of the bending potential contribution $P_{\mathrm{L}}^{\mathrm{bend}}$ to the lateral pressure profile. The symbols and error bars are shown at several data points. The density profile of hydrophilic heads [the same data in Fig. 4.7(c)] is shown as the gray-filled curve in arbitrary units. The figure is adapted from Fig. 8 in [69].

Surprisingly, the function shape of P_{L} calculated by HD(LM) has the opposite sign those calculated by the other force decomposition methods. In addition, the pressure peaks of FCD slightly shift to the outside of the position of the head particles of the bilayer [compare Figs. 4.7(b) and (c)]. As mentioned in the previous section, for all force decompositions shown in Fig. 4.7, linear- and angular-momentum conservation are satisfied.

To further examine the dependence of lateral pressure on the force decomposition, we systematically change the force center $\mathbf{r}_c$:

$$\mathbf{r}_c = \mathbf{r}_2 + \lambda \hat{\mathbf{r}}_{\mathrm{bv}}, \tag{4.20}$$

where λ is the distance between $\mathbf{r}_c$ and $\mathbf{r}_2$. For HD(GM) and HD(LM), $\lambda = \sqrt{r_{12}r_{23}}$ and $\lambda = -\sqrt{r_{12}r_{23}}$, respectively. At $\lambda = 2r_{12}r_{23}\cos(\theta_{123}/2)/(r_{12}+r_{23})$, the decomposition corresponds to CFD, since the force center is on the line segment between $\mathbf{r}_1$ and $\mathbf{r}_3$. Figures 4.8 and 4.9 show the dependence of $P_{\mathrm{L}}^{\mathrm{bend}}$ on λ. As λ increases, the lateral pressure increases. A linear relation between λ and $P_{\mathrm{L}}^{\mathrm{bend}}$ (also λ and P_{L}) is found even for negative values of λ.

This linear dependence on λ is analytically derived when $\hat{\mathbf{r}}_{\mathrm{bv}}$ is along the x axis and $\hat{\mathbf{r}}_{12} - \hat{\mathbf{r}}_{32}$ is along the z axis. Since the force pair $\mathbf{f}_{2c}$ contributes to the stress $\sigma_{xx}(z)$ as $f_{2c}\lambda\delta(z - z_2)/A_{xy}$, the lateral stress produced by the bending potential

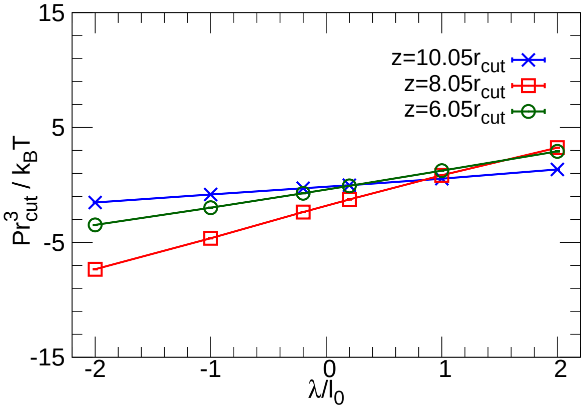

Fig. 4.9: Contribution of bending potential $P_{\mathrm{L}}^{\mathrm{bend}}$ to the lateral pressure at three xy planes with $z/r_{\mathrm{cut}} = 6.05$, 8.05, and 10.05 as a function of λ. The figure is adapted from Fig. 9 in [69].

on θ_{123} is given by

$$\begin{aligned}\sigma_{xx}^{\mathrm{bend}}(z) =& \frac{f_1 r_{12}}{A_{xy}\sin\varphi}\Big[s_{\mathrm{b}1}B(z_1, z_2, z) \\ &+ s_{\mathrm{b}2}\delta(z - z_2) + s_{\mathrm{b}3}B(z_3, z_2, z)\Big], \\ s_{\mathrm{b}1} =& -\frac{\lambda}{r_{12}} + 2\cos\varphi - \cos^3\varphi, \\ s_{\mathrm{b}2} =& \frac{r_{12}+r_{23}}{r_{12}r_{23}}\lambda - 2\cos\varphi, \\ s_{\mathrm{b}3} =& -\frac{\lambda}{r_{23}} + 2\cos\varphi - \cos^3\varphi,\end{aligned} \tag{4.21}$$

where $\varphi = \theta_{123}/2$ and A_{xy} is the area of the xy plane. Equation (4.21) clearly shows that $\sigma_{xx}^{\mathrm{bend}}(z)$ is a linear function of λ for $z_1 < z < z_3$. Our simulation results indicate that this linear relation is approximately satisfied even when averaging the conformations in which $\hat{\mathbf{r}}_{\mathrm{bv}}$ are fluctuated around the xy plane.

Gaussian curvature modulus

The Gaussian curvature modulus $\bar{\kappa}$ can be calculated [40, 46, 90] as

$$\bar{\kappa} = \int \{P_{\mathrm{N}}(z) - P_{\mathrm{L}}(z)\} z^2 dz. \tag{4.22}$$

From elastic theory, $\bar{\kappa}$ is related with κ via [55]

$$\bar{\kappa} = (\nu - 1)\kappa, \tag{4.23}$$

	$\bar{\kappa}/k_{\mathrm{B}}T$	$\bar{\kappa}/\kappa$
CFD	-3.1 ± 0.2	-0.17 ± 0.01
HD(GM)	-6.15 ± 0.09	-0.335 ± 0.006
HD(LM)	0.72 ± 0.07	0.039 ± 0.004
FCD	-32.8 ± 0.1	-1.79 ± 0.02

Table 4.1: Gaussian curvature modulus $\bar{\kappa}$ and its ratio to bending rigidity $\bar{\kappa}/\kappa$ for different force decomposition methods.

where ν is the Poisson's ratio of the bilayer membrane. Though the Poisson's ratio is generally varied in the range of $-1 \leq \nu \leq 1/2$, $\bar{\kappa}/\kappa \simeq -1$ was reported in the simulations by Hu *et al.* [45, 46] and experiments [13, 94]. Hu *et al.* calculated $\bar{\kappa}$ from the shape transition between a disk-shaped bilayer patch and vesicle. They also calculated $\bar{\kappa}$ using the pressure profile with Eq. (4.22) but concluded that the pressure profile yields unphysical results since the resultant $\bar{\kappa}$ is positive or has a small amplitude compared to κ. However, their pressure-profile calculation was performed using GLD; hence, the pressure tensor does not satisfy angular-momentum conservation. Recently, Torres-Sánchez *et al.* calculated $\bar{\kappa}$ using CFD [112]. They reported that the calculated $\bar{\kappa}$ agrees well with experimental values.

As described in Sec. 4.3.1, the lateral pressure profile is strongly dependent on the force decomposition method. Thus, $\bar{\kappa}$ estimated with Eq. (4.22) also varies significantly on changing the force center in HD. Table 4.1 lists $\bar{\kappa}$ and $\bar{\kappa}/\kappa$ for four different decomposition methods. CFD, HD(GM), and HD(LM) give $-\bar{\kappa}/\kappa \ll 1$, and FCD gives $-\bar{\kappa}/\kappa > 1$. None of them satisfy $\bar{\kappa}/\kappa \simeq -1$. To further clarify the dependence of $\bar{\kappa}$ on $\mathbf{r}_c$, we calculated $\bar{\kappa}/\kappa$ as a function of λ. Figure 4.10 shows the linear dependence of $\bar{\kappa}/\kappa$ on λ. This linearity is the consequence of the linearity of the pressure profile on λ. When $\lambda \simeq 4\ell_0$, $\bar{\kappa}/\kappa \simeq -1$ is obtained. However, this position is too far from the positions of the interacting particles. Thus, it does not seem to be physically plausible. Our results support Hu's conclusion that Eq. (4.22) gives an unphysical value of $\bar{\kappa}$ in bilayer membranes.

One may consider $\bar{\kappa}$ is not precisely determined because of the membrane undulation. There is much error in the obtained value of $\bar{\kappa}$. However, this does not strongly affect $\bar{\kappa}$ value as shown by Hu [46] as long as the membrane fluctuation is symmetric along normal direction, which is satisfied for the simulation. Therefore, membrane undulation does not strongly affect $\bar{\kappa}$ obtained from the pressure profile within the bilayer whose patch size is the order of the persistence length.

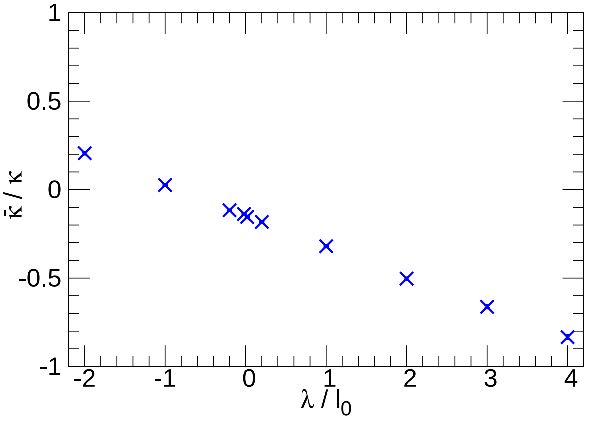

Fig. 4.10: Ratio of Gaussian curvature modulus $\bar{\kappa}$ to bending rigidity κ as a function of λ. The figure is adapted from Fig. 10 in [69].

4.3.2 Atomistic model

Model description

The DOPC molecules are modeled by the recent version of CHARMM all-atom force field (CHARMM36) [52,53], and water molecules are modeled by rigid TIP3P. We apply CFD, FCD, HD(LM), and HD(GM) to the bending potential. The four-body potential contribution to local stress field is calculated using CFD. The details of the simulation method are described in Appendix 4.D.2.

Lateral pressure profile

The lateral pressure profiles along the bilayer normal direction are shown in Fig. 4.11 for four different force decomposition methods. The pressure profiles are calculated for small slices with slice width $\Delta z = 0.1$nm in the same manner as in Sec. 4.3.1. The dependence of lateral pressure profile on the force decompositions is qualitatively similar to that of the DPD model but its amplitude becomes much smaller [see Fig. 4.11(b)]. The differences of force decompositions affect the local pressure at the surface between water and amphiphilic molecules. In the hydrophobic region, there are no significant differences of stress profiles for different force decompositions. Thus, in the higher-resolution model, the decomposition methods of the bending forces modify the pressure profile less than the lower-resolution (coarse-grained) model.

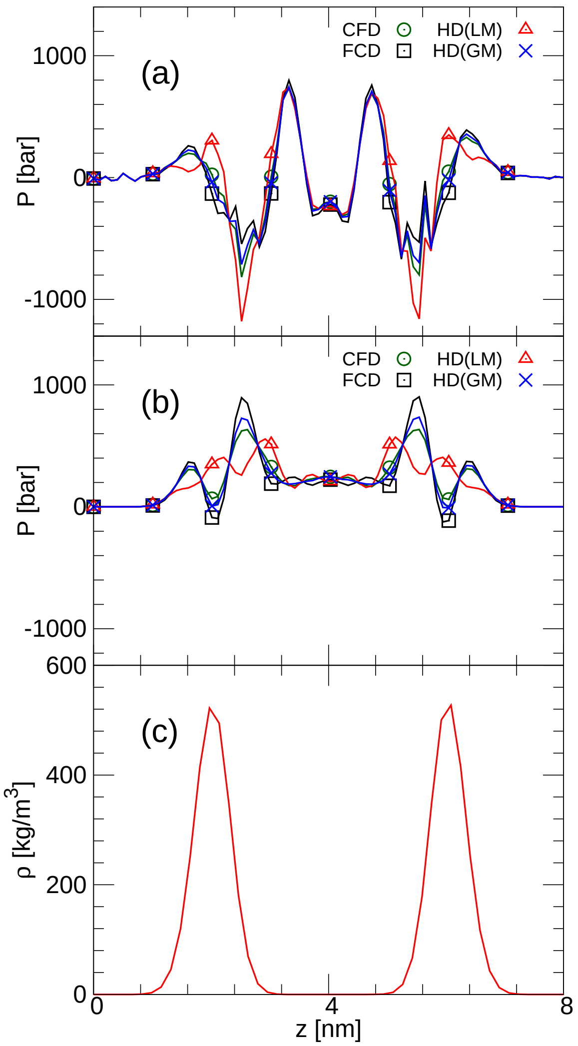

Fig. 4.11: Pressure and density profiles of DOPC membrane along the bilayer normal (z) axis. (a) Total lateral pressure profile for four force decomposition methods. (b) Partial lateral pressure profile given by the bending potential. (c) Mass density profile of hydrophilic head groups (phosphoric acid and choline groups). The figure is adapted from Fig. 11 in [69].

4.4 Discussion

The total stress of each three-body potential is independent of the decomposition method. However, the distribution of this stress in 2D space significantly varies even under the strong law of action and reaction. We introduced the stress distribution magnitude Γ_{SDM} to evaluate the decomposition method. For the area potentials, Γ_{SDM} has the minimum value in the entire triangular region formed by the three particles, whereas Γ_{SDM} has the minimum value at a single position for the bending potentials. Hence, Γ_{SDM} can be used to reduce the candidates for suitable decompositions but the best (unique) decomposition is not determined by Γ_{SDM}, at least for the area potential.

The discrete stress of a molecular simulation can be mapped into the stress field in the continuum space. If the corresponding stress field in the continuum space is known, one can state that the decomposition producing the closest stress is the best choice. In typical simulation conditions, the resultant stress cannot be obtained a priori. However, if a particle potential is constructed as a discretized version of the potential in the continuum space, the corresponding stress field in the continuum space is obtained from the original continuum potential. The surface tension $k_{\mathrm{ar}}A_{123}$ is one of the discretized potentials. When a continuum surface with area A is discretized to acute triangles, the surface tension of $k_{\mathrm{ar}}A$ is discretized to $k_{\mathrm{ar}}\sum_k A_k$, where A_k is the area of the k-th triangle. When the triangle is on the xy plane, $\sigma_{xx}(\mathbf{x}) = \sigma_{yy}(\mathbf{x}) = k_{\mathrm{ar}}/L_z$ and $\sigma_{xy}(\mathbf{x}) = 0$ are given in the continuum description, where L_z is the side length of the simulation box in the z direction. Both CFD and FCD distribute the stress into line segments so that they deviate from the constant stress field. If HD with multiple force centers distributed on the triangle is employed, a nearly constant stress field can be constructed. Alternatively, Hardy's spatial average with a weighting function [36] also helps CFD and FCD to approach the constant field.

For surface tension or other discretized potentials, the resultant stress field becomes closer to the original continuum field as the surface is discretized into smaller triangles. Thus, it is related with the resolution of the simulation. For classical molecular simulations, local interactions in a length scale smaller than the diameter of atoms or particles are not typically taken into account for coarse-graining. For all-atom simulations, the force fields between atoms are constructed from ab initio quantum mechanical calculations [19, 64, 66]. Even from the viewpoint of classical mechanics, each particle has a finite size. For a pairwise interaction such as chemical bonds, the stress is distributed not only in the line segment between two particle centers but also in a cylindrical region with the diameter equal to the particle size. Thus, one may have to determine the decomposition method for multibody forces through comparison with the underlying high-resolution potential interactions. For lipid membranes, the pressure profile of the higher-resolution atomistic model has much smaller dependence on the decomposition than that of the lower-resolution (four-particle) DPD model. This also supports our hypothesis on the resolution.

Let us go back to the discussion on the stress field of the bending forces on θ_{123}. CFD and HD(GM) of the bending forces give the stress distribution on the edge of $\mathbf{r}_{13}$ or close to the edge, respectively. If these positions are within the interaction radius of the atom (or particle) at $\mathbf{r}_1$ or $\mathbf{r}_3$, they can be employed as a force-acting point. However, FCD and HD(LM) are unphysical since their force centers are far from the triangle $\triangle 123$ in most of the case. For real bending potentials, the stress distribution may strongly depend on the molecules, but it is likely approximated to the interaction between two chemical bonds (the middle points of $\mathbf{r}_{12}$ and $\mathbf{r}_{23}$). Thus, HD with the force center $\mathbf{r}_c$ lying in the middle of $\triangle 123$ may be a physically reasonable decomposition, where $\Gamma_{\rm SDM}$ is greater than those of HD(GM) and CFD but the stress profile of the bilayer membranes is flatter.

A coarse-grained model often does not have a specific underlying higher-resolution model. In such a case, one may have to calculate the stress field without the higher-resolution information. We describe our speculative consideration on the choice of the decomposition when the force center $\mathbf{r}_{c0}$ lies in the interior region of the triangle of three interacting particles like in the area potential. In this case, FCD, CFD, and HD which force center lying in the interior of the triangle has the minimum value of $\Gamma_{\rm SDM}$. Among of them, FCD gives the minimum of the total length $\ell_{\rm sum}$, *i.e.*, the minimum propagation path of the stress. Therefore, the minimum total length may be employed as an additional criterion so that FCD can be chosen.

For n-body forces with $n \geq 4$, all of the extrapolations of the force vectors $\mathbf{f}_i$ from $\mathbf{r}_i$ do not typically meet at a single position. Thus, FCD is not generally available for $n \geq 4$. However, FCD can be performed for specific potentials for which all $\mathbf{f}_i$ meet a single position. Let us consider potentials $U_{\rm rg}(r_{\rm gw}^2)$ on a weighted radius of gyration $r_{\rm gw}^2 = \sum_i^n w_i(\mathbf{r}_i - \mathbf{r}_{\rm Gw})^2$ for a center position $\mathbf{r}_{\rm Gw} = \sum_i^n w_i\mathbf{r}_i$, where the weight w_i is normalized as $\sum_i^n w_i = 1$. Since all of $\mathbf{f}_i$ meet at $\mathbf{r}_{\rm Gw}$, these forces are decomposed by FCD with the force center $\mathbf{r}_c = \mathbf{r}_{\rm Gw}$. If the force center $\mathbf{r}_c = \mathbf{r}_{\rm Gw}$ or a force center for three of the forces is used, HD is applicable for any n-body force. The center position $\mathbf{r}_c$ can be arbitrarily set by adjusting w_i in $\mathbf{r}_{\rm Gw}$. Multiple center positions may be useful. However, it has many choices of the force decomposition for $n \geq 4$, and it is currently unclear how the force decomposition can be tuned.

4.5 Summary

We have proposed a decomposition method (FCD) of three-body forces using the position, where three force extrapolations from the particle positions meet, and combined it with CFD, which decomposes the forces into force pairs between interacting particles. Our study has revealed that the local stress field of three-body forces is strongly dependent on these decomposition methods. We have discussed the choice of the decomposition using the stress distribution magnitude Γ_{SDM} and comparison with the stress fields in continuum fields and in higher resolutions of discretization. We have not reached a concrete conclusion for the best decomposition but rather considered that it depends on the underlying higher-resolution potential.

Appendix

4.A Area Potential

Here, we describe the force decomposition of the general form of area potentials, $U_{\mathrm{ar}}(A_{123})$, for the triangle $\triangle 123$. The area is given by $A_{123} = |\mathbf{r}_{12} \times \mathbf{r}_{13}|/2$. The force $\mathbf{f}_1$ is given as

$$\mathbf{f}_1 = -\frac{\partial U_{\mathrm{ar}}}{\partial \mathbf{r}_1} = -\frac{U'_{\mathrm{ar}}}{4A_{123}}[r_{23}^2\mathbf{r}_{13} - (\mathbf{r}_{13}\cdot\mathbf{r}_{23})\mathbf{r}_{23}], \tag{4.24}$$

where $U'_{\mathrm{ar}} = \partial U_{\mathrm{ar}}/\partial A_{123}$. This force $\mathbf{f}_1$ is perpendicular to $\mathbf{r}_{23}$, since the area does not change if $\mathbf{r}_1$ moves parallel to $\mathbf{r}_{23}$. For the potential of the surface tension $U_{\mathrm{ar}}(A_{123}) = k_{\mathrm{ar}}A_{123}$, $U'_{\mathrm{ar}} = k_{\mathrm{ar}}$.

The force f_{12} in CFD is obtained by the decomposition of $\mathbf{f}_1$ into components along $\hat{\mathbf{r}}_{12}$ and $\hat{\mathbf{r}}_{13}$ or directly by using $f_{12} = -\partial U_{\mathrm{ar}}/\partial r_{12}|r_{13}, r_{23}$ with Heron's formula $A_{123} = \sqrt{b(b-r_{12})(b-r_{13})(b-r_{23})}$, where $b = (r_{12}+r_{13}+r_{23})/2$:

$$f_{12} = -\frac{U'_{\mathrm{ar}}}{4A_{123}}(\mathbf{r}_{13}\cdot\mathbf{r}_{23})r_{12}. \tag{4.25}$$

The other forces $\mathbf{f}_2$, $\mathbf{f}_3$, f_{13}, and f_{23} are similarly obtained. The original force center $\mathbf{r}_{c0}$ is the orthocenter of $\triangle 123$. Since $q = 1/4{U'_{\mathrm{ar}}}^2 > 0$, $\mathbf{r}_{c0}$ lies in the interior region or exterior region A, C, or E of $\triangle 123$ depicted in Fig. 4.3. When $\triangle 123$ is an acute triangle, $\mathbf{r}_{c0}$ lies in the interior region. When the angle θ_{123} is obtuse ($\mathbf{r}_{12}\cdot\mathbf{r}_{32} < 0$), $\mathbf{r}_{c0}$ lies in the exterior region E.

4.B Bending Potential

Next, we describe the force decomposition of the general form of bending potentials, $U_{\mathrm{bendg}}(\hat{\mathbf{r}}_{12}\cdot\hat{\mathbf{r}}_{32})$, for the angle $\theta_{123} = \cos^{-1}(\hat{\mathbf{r}}_{12}\cdot\hat{\mathbf{r}}_{32})$ of three particle positions

$\mathbf{r}_1$, $\mathbf{r}_2$, and $\mathbf{r}_3$. The forces on the three particles are given by

$$
\begin{aligned}
\mathbf{f}_1 &= -\frac{U'_{\mathrm{bendg}}}{r_{12}}[\hat{\mathbf{r}}_{32} - (\hat{\mathbf{r}}_{12}\cdot\hat{\mathbf{r}}_{32})\hat{\mathbf{r}}_{12}], \\
\mathbf{f}_2 &= -\frac{U'_{\mathrm{bendg}}}{r_{12}r_{32}}\left[\frac{(\mathbf{r}_{12}\cdot\mathbf{r}_{32} - r_{12}^2)\hat{\mathbf{r}}_{12}}{r_{12}} + \frac{(\mathbf{r}_{12}\cdot\mathbf{r}_{32} - r_{32}^2)\hat{\mathbf{r}}_{32}}{r_{32}}\right], \\
\mathbf{f}_3 &= -\frac{U'_{\mathrm{bendg}}}{r_{32}}[\hat{\mathbf{r}}_{12} - (\hat{\mathbf{r}}_{12}\cdot\hat{\mathbf{r}}_{32})\hat{\mathbf{r}}_{32}].
\end{aligned}
\tag{4.26}
$$

The forces $\mathbf{f}_1$ and $\mathbf{f}_3$ are perpendicular to $\mathbf{r}_{12}$ and $\mathbf{r}_{32}$, respectively, since θ_{123} is independent of the lengths r_{12} and r_{32}. For the bending potential of Eq. (4.19), $U'_{\mathrm{bend}} = -k_{\mathrm{b}}$.

In CFD, these forces are decomposed into the following force pairs:

$$
\begin{aligned}
f_{12} &= -U'_{\mathrm{bendg}}\frac{\mathbf{r}_{12}\cdot\mathbf{r}_{13}}{r_{12}^2 r_{23}}, \\
f_{13} &= U'_{\mathrm{bendg}}\frac{r_{13}}{r_{12}r_{23}}, \\
f_{23} &= -U'_{\mathrm{bendg}}\frac{\mathbf{r}_{23}\cdot\mathbf{r}_{13}}{r_{12}r_{23}^2}.
\end{aligned}
\tag{4.27}
$$

These force pairs can be obtained from Eqs. (4.26) and (4.11) or directly from $f_{12} = -\partial U_{\mathrm{bendg}}/\partial r_{12}|r_{13}, r_{23}$ with $\hat{\mathbf{r}}_{12}\cdot\hat{\mathbf{r}}_{32} = (r_{12}^2 + r_{23}^2 - r_{13}^2)/2r_{12}r_{23}$. The original force center $\mathbf{r}_{c0}$ always lies in the exterior region of $\triangle 123$, since $q = -4A_{123}^2/r_{12}^4 r_{23}^4 {U'_{\mathrm{bendg}}}^2 < 0$. When the angles $\theta_{312} < \pi/2$ and $\theta_{231} < \pi/2$, $f_{12}f_{23} > 0$ and $f_{12}f_{13} < 0$ so that $\mathbf{r}_{c0}$ lies in the exterior region B depicted in Fig. 4.3. For $\theta_{312} > \pi/2$ or $\theta_{231} > \pi/2$, $\mathbf{r}_{c0}$ lies in the region D or F, respectively. The stress distribution magnitudes Γ_{SDM} for FCD and CFD take the same value for the bending potentials: $\Gamma_{\mathrm{FCD}} = \Gamma_{\mathrm{CFD}} = 2r_{13}^2|U'_{\mathrm{bendg}}|/r_{12}r_{23}$ for $\theta_{312} < \pi/2$ and $\theta_{231} < \pi/2$, and $\Gamma_{\mathrm{FCD}} = \Gamma_{\mathrm{CFD}} = 2\mathbf{r}_{12}\cdot\mathbf{r}_{13}|U'_{\mathrm{bendg}}|/r_{12}r_{23}$ for $\theta_{231} > \pi/2$. For the typical simulation conditions including our present simulation, θ_{312} and θ_{231} are small. Thus, we consider only the case of $\mathbf{r}_{c0}$ lying in region B in this paper.

4.C Minimization of Stress Distribution Magnitude for Exterior Force Center

Here, we consider the force center $\mathbf{r}_c$ for the minimum of the stress distribution magnitude Γ_{SDM}, when $\mathbf{r}_{c0}$ lies in the exterior region B, where $f_{12}f_{13} < 0$, $f_{12}f_{23} > 0$, and $q < 0$. As mentioned in Sec. 4.2.3, Γ_{SDM} takes the lowest value at the position $\mathbf{r}_{\mathrm{m}}$ given in Eq. (4.18) for HD with $f_{13}^{\mathrm{CFD}} = 0$, if $\mathbf{r}_{\mathrm{m}}$ is in the interior region surrounded by three positions $\mathbf{r}_1$, $\mathbf{r}_3$, and $\mathbf{r}_{c0}$. This position is derived as follows. We consider the minimization of the difference $\Gamma_{\mathrm{dif}} = \Gamma_{\mathrm{SDM}} - \Gamma_{\mathrm{CFD}} = \Gamma_{\mathrm{HD}}^{\mathrm{FC}} - (|f_{12}^{\mathrm{FC}}|r_{12} + |f_{13}^{\mathrm{FC}}|r_{13} + |f_{23}^{\mathrm{FC}}|r_{23})$, since the contribution of the CFD force pairs does not explicitly appear in Γ_{dif}.

$$\begin{aligned}
\Gamma_{\mathrm{dif}} &= \frac{2\tilde{f}_{12}^{\mathrm{FC}}\tilde{f}_{23}^{\mathrm{FC}}}{|q|}(|\tilde{f}_{12}^{\mathrm{FC}}|r_{12}^2 + |\tilde{f}_{23}^{\mathrm{FC}}|r_{23}^2 - |\tilde{f}_{13}^{\mathrm{FC}}|r_{13}^2) \\
&= 2|\tilde{f}_{13}^{\mathrm{FC}}|r_{13}^2 g(x,y), \qquad (4.28)
\end{aligned}$$

where

$$\begin{aligned}
g(x,y) &= \frac{xy\left\{\left(\frac{r_{12}}{r_{13}}\right)^2 x + \left(\frac{r_{23}}{r_{13}}\right)^2 y - 1\right\}}{x+y-xy}, \qquad (4.29) \\
x &= -\frac{\tilde{f}_{12}^{\mathrm{FC}}}{\tilde{f}_{13}^{\mathrm{FC}}} \quad \text{and} \quad y = -\frac{\tilde{f}_{23}^{\mathrm{FC}}}{\tilde{f}_{13}^{\mathrm{FC}}}. \qquad (4.30)
\end{aligned}$$

The force ratios x and y for the minimum of g are obtained from $\partial g/\partial x = 0$ and $\partial g/\partial y = 0$ as

$$g(x_{\mathrm{GM}}, y_{\mathrm{GM}}) = -\frac{r_{12} + r_{23} - \sqrt{(r_{12}+r_{23})^2 - r_{13}^2}}{r_{12} + r_{23} + \sqrt{(r_{12}+r_{23})^2 - r_{13}^2}} < 0 \qquad (4.31)$$

with

$$\begin{aligned}
x_{\mathrm{GM}} &= \frac{r_{12} + r_{23} - \sqrt{(r_{12}+r_{23})^2 - r_{13}^2}}{r_{12}}, \qquad (4.32) \\
y_{\mathrm{GM}} &= \frac{r_{12} + r_{23} - \sqrt{(r_{12}+r_{23})^2 - r_{13}^2}}{r_{23}}. \qquad (4.33)
\end{aligned}$$

The position $\mathbf{r}_{\mathrm{m}}$ in Eq. (4.18) is given by x_{GM} and y_{GM}. To minimize Γ_{dif}, the factor $|f_{13}^{\mathrm{FC}}|$ in Eq. (4.28) is taken as the maximum value while maintaining $|f_{13}^{\mathrm{FC}}| + |f_{13}^{\mathrm{CF}}| = |f_{13}^{\mathrm{all}}|$, *i.e.*, $f_{13}^{\mathrm{CF}} = 0$. Hence, the lowest value of Γ_{SDM} is obtained for HD with the force center of $\mathbf{r}_{\mathrm{m}}$ and $f_{13}^{\mathrm{CF}} = 0$.

The local minimum in the region E (LM) is derived from the minimization of $\Gamma_{\mathrm{SDM}} + \Gamma_{\mathrm{CFD}} = -2|\tilde{f}_{13}^{\mathrm{FC}}|r_{13}^2 g(x,y)$, since $f_{12}^{\mathrm{CF}} f_{12}^{\mathrm{FC}} < 0$, $f_{23}^{\mathrm{CF}} f_{23}^{\mathrm{FC}} < 0$, and $f_{13}^{\mathrm{CF}} = 0$. The maximum of g is given at

$$\begin{aligned}
x_{\mathrm{LM}} &= \frac{r_{12} + r_{23} + \sqrt{(r_{12}+r_{23})^2 - r_{13}^2}}{r_{12}}, \qquad (4.34) \\
y_{\mathrm{LM}} &= \frac{r_{12} + r_{23} + \sqrt{(r_{12}+r_{23})^2 - r_{13}^2}}{r_{23}}. \qquad (4.35)
\end{aligned}$$

Hence, the local-minimum position is determined as $\mathbf{r}_{\mathrm{lm}} = \mathbf{r}_2 - \sqrt{r_{12}r_{23}}\hat{\mathbf{r}}_{\mathrm{bv}}$ from x_{LM} and y_{LM}.

4.D Simulation Method

4.D.1 Coarse-grained model

All simulations are carried out under the NVT ensemble at the particle density $N/V = 3/r_{\text{cut}}^3$ with a periodic boundary condition. The pressure profiles are calculated for a tensionless membrane at $N_{\text{amp}} = 738$, $N_{\text{w}} = 9336$, and the side lengths of the simulation box $L_x = L_y = L_z = 16r_{\text{cut}}$ by using the IKN procedure with the decomposition described in Sec. 4.2, where N_{amp} and N_{w} are the numbers of amphiphilic molecules and water particles, respectively. Amphiphilic molecules are pre-formed into a flat bilayer to reduce the equilibration time. After the equilibration time $\tau_{\text{eq}} = 10000\tau$ or 15000τ, production runs are carried out during 5000τ. The bending rigidity κ of the bilayer membrane is estimated at $N_{\text{amp}} = 2950$ and $N_{\text{w}} = 86504$ by using the undulation mode of a nearly planar tensionless membrane [31,37,58], $\langle |h(|\mathbf{k}|)|^2 \rangle = k_{\text{B}}T/\kappa|\mathbf{k}|^4$, with the extrapolation of the cutoff wavelength, $k_{\text{cut}} \to 0$ [99], where $h(|\mathbf{k}|)$ is the Fourier transformation of bilayer height $h(x, y)$. Error bars are calculated from five independent runs.

4.D.2 Atomistic model

MD simulations are carried out in the NPT ensemble using the standard version of GROMACS 5.1 simulation packages [2, 84]. Bilayer membranes consisting of 400 DOPC molecules surrounded by 20000 water molecules are simulated under $T = 303.15°\text{C}$ and $P = 1\text{bar}$. The temperature and pressure are controlled by the Nosé-Hoover and Parrinello-Rahman method, respectively. Newton's equation is integrated using the leap-frog algorithm with MD time step $\Delta t = 2$ fs. A bond constraint is applied to the bonds with hydrogens using LINCS algorithm. Long-range electrostatic interactions are calculated via Particle Mesh Ewald (PME) method. All initial configurations and input parameters are generated using CHARMM-GUI Membrane Builder [51, 56]. The total simulation time is 600 ns, and the first 360 ns is taken as the equilibration time.

The obtained MD trajectories are fed into a customized version of GROMACS-LS [117] to calculate the local stress profiles. The dihedral contribution to local stress is calculated using CFD. The electrostatic contribution is calculated using the IKN procedure with cutoff length $r_{\text{cut}}^{\text{el}} = 2.2\text{nm}$. Venegas *et al.* examined the electrostatic contributions to the local pressure profile using the IKN procedure with finite cutoff by changing $r_{\text{cut}}^{\text{el}}$ and reported that the local stress profile shows little difference at $r_{\text{cut}}^{\text{el}} > 2.2\text{nm}$ [118].

Chapter 5

Conclusion and Perspective

In this dissertation, we studied the two topics regarding the bilayer membranes. We summarize the central results and show the future perspectives.

First, we investigated the shape transformations of bilayer membranes induced by the hydrolysis and condensation reactions of amphiphilic molecules using CG molecular simulations. The hydrolysis and condensation reactions are treated explicitly by the bond dissociation and binding, whereas these chemical reactions are taken into account implicitly by the change of the amphiphilic molecular density difference in the previous works. The asymmetric chemical conditions, which are widely observed both *in vitro* and *in vivo*, cause the asymmetric amphiphilic molecular densities between inner and outer leaflets, leading to the BP formations. We examine the effects of EOs (hydrolyzed hydrophobic molecules embedded in the bilayer) on the BP formation; the density inhomogeneity of EOs enhances the growth of BPs. We also show that the density inhomogeneity of EOs is determined by the competition between two different dynamics: diffusion of EOs and synthesis of EOs. Although only BPs formations occur at high reduced volume, buds formations also occur at low reduced. At low reduced volume, resulting shape transformations are affected by the viscosity ration of the membrane to the bulk solution and the synthesis rates of EOs. The higher bulk viscosity compared with membrane viscosity enhances the BPs formations.

The shape transformations of vesicles induced by the chemical reactions have been reported by the several researchers, but the theoretical analyses of these shape transformations were carried out phenomenologically based on the ADE model. The effects of resultant reaction products on the bilayer membrane morphologies were not taken into account. Our work reveals the role of these reaction products. We hope our work will advance the study of vesicle morphology induced by the chemical reactions from the theoretical point of view.

Next, we studied the pressure profile calculation methods in molecular simulations and point out the severe problem of conventional method regarding the multibody forces. The conventional method to calculate the stress fields which containing the multibody forces is based on CFD, in which the multibody forces are decomposed into the pairwise forces, and IKN procedure is applied to these decomposed pairwise forces. However, we propose the different force decomposition called FCD and HD by adding a force center, and show that the pressure profile of CG and atomistic bilayer membrane strongly depends on the force decompositions; the position of force center changes the resulting pressure profile. In this dissertation, we only consider the case for the three body forces, but similar problems exist even for four or higher multibody forces. To remove this ambiguity, we introduce SDM as an candidate criterion and consider the minimization problem of SDM. We derive the analytical expression of the local minimum and global minimum of SDM. To check the validity of SDM as an appropriate criterion, we calculate Gaussian curvature modulus $\bar{\kappa}$ from the pressure profile within the bilayer for CFD, FCD, HD at local minimum of SDM, and HD at the global minimum of SDM as shown in Table. 4.1. The ratio of $\bar{\kappa}$ to κ is in the range of -2–-0.5 according to the classical theory of elasticity, but only $\bar{\kappa}/\kappa$ calculated using FCD agrees well with the results of elasticity theory although the force decomposition point of FCD is far from three interacting particles. The physically plausible force decomposition point should not be far from three interacting particles. However, as far as $\bar{\kappa}/\kappa$ is employed to verify the pressure profile within the bilayer, the position of force center point should be far from three interacting points.

There are two possibilities to explain the result. The first possibility is that the stress distribution magnitude is not a suitable criterion to remove the ambiguity of the force decompositions. The second possibility is that the equation (4.22) is not applicable to calculate the Gaussian curvature modulus. In any case, an alternative criterion to remove the ambiguity should be developed in future works.

Lastly, in this dissertation, we investigated the bilayer membrane using molecular simulations. In the future, the improvement of computational power will broaden the accessible length and time scale of molecular simulations. We can perform the large-scale molecular simulations of atomistic bilayer membrane model. We expect that the large-scale molecular simulations enable the direct bridging between the macroscopic and microscopic description and reveal new aspects of bilayer membranes.

References

[1] Biological membrane (Nov. 30, 2017, 09:02 UTC). in *Wikipedia: The Free Encyclopedia*. `https://en.wikipedia.org/wiki/Biological_membrane`.

[2] M. J. Abraham, T. Murtola, R. Schulz, S. Páll, J. C. Smith, B. Hess, and E. Lindahl. GROMACS: high performance molecular simulations through multi-level parallelism from laptops to supercomputers. *SoftwareX*, 1:19–25, 2015.

[3] N. C. Admal. *Results on the interaction between atomistic and continuum models*. PhD thesis, The University of Minnesota, 2014.

[4] N. C. Admal and E. Tadmor. Stress and heat flux for arbitrary multibody potentials: A unified framework. *The Journal of Chemical Physics*, 134(18):184106, 2011.

[5] N. C. Admal and E. Tadmor. The non-uniqueness of the atomistic stress tensor and its relationship to the generalized beltrami representation. *Journal of the Mechanics and Physics of Solids*, 93:72–92, 2016.

[6] N. C. Admal and E. B. Tadmor. A unified interpretation of stress in molecular systems. *Journal of Elasticity*, 100(1-2):63–143, 2010.

[7] D. Allan, M. G. Low, J. B. Finean, and R. H. Michell. Changes in lipid metabolism and cell morphology following attack by phospholipase C (clostridium perfringens) on red cells or lymphocytes. *Biochimica et Biophysica Acta*, 413(2):309–316, 1975.

[8] D. Allan, P. Thomas, and R. H. Michell. Rapid transbilayer diffusion of 1, 2-diacylglycerol and its relevance to control of membrane curvature. *Nature*, 276(5685):289–290, 1978.

[9] M. P. Allen and D. J. Tildesley. *Computer simulation of liquids*. Oxford university press, Oxford, 1989.

[10] B. Alverts, A. Johnson, J. Lewis, M. Raff, K. Roberts, P. Walter, J. Wilson, and T. Hunt. *Molecular Biology of the Cell.* Garland Science, New York, 5th edition, 2007.

[11] S. Baoukina, L. Monticelli, H. J. Risselada, S. J. Marrink, and D. P. Tieleman. The molecular mechanism of lipid monolayer collapse. *Proceedings of the National Academy of Sciences of the United States of America*, 105(31):10803–10808, 2008.

[12] G. Basanez, M. B. Ruiz-Argüello, A. Alonso, F. M. Goni, G. Karlsson, and K. Edwards. Morphological changes induced by phospholipase C and by sphingomyelinase on large unilamellar vesicles: a cryo-transmission electron microscopy study of liposome fusion. *Biophysical Journal*, 72(6):2630–2637, 1997.

[13] T. Baumgart, S. Das, W. Webb, and J. Jenkins. Membrane elasticity in giant vesicles with fluid phase coexistence. *Biophysical Journal*, 89(2):1067–1080, 2005.

[14] R. M. Bell. Protein kinase C activation by diacylglycerol second messengers. *Cell*, 45(5):631–632, 1986.

[15] R. M. Bell, L. M. Ballas, and R. A. Coleman. Lipid topogenesis. *The Journal of Lipid Research*, 22(3):391–403, 1981.

[16] D. Boal. *Mechanics of the Cell.* Cambridge University Press, Cambridge, 2nd edition, 2012.

[17] I. R. Cooke and M. Deserno. Solvent-free model for self-assembling fluid bilayer membranes: stabilization of the fluid phase based on broad attractive tail potentials. *The Journal of Chemical Physics*, 123(22):224710, 2005.

[18] I. R. Cooke, K. Kremer, and M. Deserno. Tunable generic model for fluid bilayer membranes. *Physical Review E*, 72(1):011506, 2005.

[19] W. D. Cornell, P. Cieplak, C. I. Bayly, I. R. Gould, K. M. Merz, D. M. Ferguson, D. C. Spellmeyer, T. Fox, J. W. Caldwell, and P. A. Kollman. A second generation force field for the simulation of proteins, nucleic acids, and organic molecules. *Journal of the American Chemical Society*, 117(19):5179–5197, 1995.

[20] S. Das and R. P. Rand. Modification by diacylglycerol of the structure and interaction of various phospholipid bilayer membranes. *Biochemistry*, 25(10):2882–2889, 1986.

[21] W. K. den Otter and S. A. Shkulipa. Intermonolayer friction and surface shear viscosity of lipid bilayer membranes. *Biophysical Journal*, 93(2):423–433, 2007.

[22] P. Espanol and P. Warren. Statistical mechanics of dissipative particle dynamics. *EPL (Europhysics Letters)*, 30(4):191–196, 1995.

[23] X. Fan, N. Phan-Thien, S. Chen, X. Wu, and T. Y. Ng. Simulating flow of DNA suspension using dissipative particle dynamics. *Physics of Fluids*, 18(6):063102, 2006.

[24] J.-B. Fournier, N. Khalifat, N. Puff, and M. Angelova. Chemically triggered ejection of membrane tubules controlled by intermonolayer friction. *Physical Review Letters*, 102(1):018102, 2009.

[25] M. D. Fraňová, I. Vattulainen, and O. H. S. Ollila. Can pyrene probes be used to measure lateral pressure profiles of lipid membranes? perspective through atomistic simulations. *Biochimica et Biophysica Acta*, 1838(5):1406–1411, 2014.

[26] P. Fromherz. Lipid-vesicle structure: size control by edge-active agents. *Chemical Physics Letters*, 94(3):259–266, 1983.

[27] K. Fujiwara and M. Yanagisawa. Generation of giant unilamellar liposomes containing biomacromolecules at physiological intracellular concentrations using hypertonic conditions. *ACS Synthetic Biology*, 3(12):870–874, 2014.

[28] K. Fujiwara and M. Yanagisawa. Liposomal internal viscosity affects the fate of membrane deformation induced by hypertonic treatment. *Soft Matter*, 13(48):9192–9198, 2017.

[29] L. Gao, R. Lipowsky, and J. Shillcock. Tension-induced vesicle fusion: pathways and pore dynamics. *Soft Matter*, 4(6):1208–1214, 2008.

[30] L. Gao, J. Shillcock, and R. Lipowsky. Improved dissipative particle dynamics simulations of lipid bilayers. *The Journal of Chemical Physics*, 126(1):01B602, 2007.

[31] R. Goetz, G. Gompper, and R. Lipowsky. Mobility and elasticity of self-assembled membranes. *Physical Review Letters*, 82(1):221–224, 1999.

[32] R. Goetz and R. Lipowsky. Computer simulations of bilayer membranes: self-assembly and interfacial tension. *The Journal of Chemical Physics*, 108(17):7397–7409, 1998.

[33] A. Gopal and K. Y. C. Lee. Morphology and collapse transitions in binary phospholipid monolayers. *The Journal of Physical Chemistry B*, 105(42):10348–10354, 2001.

[34] R. D. Groot and K. L. Rabone. Mesoscopic simulation of cell membrane damage, morphology change and rupture by nonionic surfactants. *Biophysical Journal*, 81(2):725–736, 2001.

[35] R. D. Groot and P. B. Warren. Dissipative particle dynamics: Bridging the gap between atomistic and mesoscopic simulation. *The Journal of Chemical Physics*, 107(11):4423–4435, 1997.

[36] R. J. Hardy. Formulas for determining local properties in molecular-dynamics simulations: Shock waves. *The Journal of Chemical Physics*, 76(1):622–628, 1982.

[37] V. A. Harmandaris and M. Deserno. A novel method for measuring the bending rigidity of model lipid membranes by simulating tethers. *The Journal of Chemical Physics*, 125(20):204905, 2006.

[38] H. Heinz, W. Paul, and K. Binder. Calculation of local pressure tensors in systems with many-body interactions. *Physical Review E*, 72(6):066704, 2005.

[39] W. Helfrich. Elastic properties of lipid bilayers: theory and possible experiments. *Zeitschrift für Naturforschung*, 28(11-12):693–703, 1973.

[40] W. Helfrich. Lyotropic lamellar phases. *Journal of Physics: Condensed Matter*, 6(23A):A79–A92, 1994.

[41] J. M. Holopainen, M. I. Angelova, and P. K. J. Kinnunen. Vectorial budding of vesicles by asymmetrical enzymatic formation of ceramide in giant liposomes. *Biophysical Journal*, 78(2):830–838, 2000.

[42] M. Hömberg and M. Müller. Main phase transition in lipid bilayers: phase coexistence and line tension in a soft, solvent-free, coarse-grained model. *The Journal of Chemical Physics*, 132(15):04B609, 2010.

[43] P. J. Hoogerbrugge and J. M. V. A. Koelman. Simulating microscopic hydrodynamic phenomena with dissipative particle dynamics. *EPL (Europhysics Letters)*, 19(3):155–160, 1992.

[44] H. Hotani, F. Nomura, and Y. Suzuki. Giant liposomes: from membrane dynamics to cell morphogenesis. *Current opinion in colloid & interface science*, 4(5):358–368, 1999.

[45] M. Hu, J. J. Briguglio, and M. Deserno. Determining the gaussian curvature modulus of lipid membranes in simulations. *Biophysical Journal*, 102(6):1403–1410, 2012.

[46] M. Hu, D. H. de Jong, S. J. Marrink, and M. Deserno. Gaussian curvature elasticity determined from global shape transformations and local stress distributions: a comparative study using the martini model. *Faraday Discussions*, 161:365–382, 2013.

[47] F. Huang, Y. Lv, L. Wang, P. Xu, J. Lin, and S. Lin. An insight into polymerization-induced self-assembly by dissipative particle dynamics simulation. *Soft Matter*, 12(30):6422–6429, 2016.

[48] M. Ibarguren, J. Sot, L.-R. Montes, A. I. Vasil, M. L. Vasil, F. M. Goñi, and A. Alonso. Recruitment of a phospholipase C/sphingomyelinase into nonlamellar lipid droplets during hydrolysis of lipid bilayers. *Chemistry and Physics of Lipids*, 166:12–17, 2013.

[49] J. H. Irving and J. G. Kirkwood. The statistical mechanical theory of transport processes. IV. the equations of hydrodynamics. *The Journal of Chemical Physics*, 18(6):817–829, 1950.

[50] J. N. Israelachvili. *Intermolecular and surface forces.* Academic Press, Burlington, MA, 3rd edition, 2011.

[51] S. Jo, T. Kim, V. G. Iyer, and W. Im. CHARMM-GUI: a web-based graphical user interface for CHARMM. *Journal of Computational Chemistry*, 29(11):1859–1865, 2008.

[52] J. B. Klauda, V. Monje, T. Kim, and W. Im. Improving the CHARMM force field for polyunsaturated fatty acid chains. *The Journal of Physical Chemistry B*, 116(31):9424–9431, 2012.

[53] J. B. Klauda, R. M. Venable, J. A. Freites, J. W. O'Connor, D. J. Tobias, C. Mondragon-Ramirez, I. Vorobyov, A. D. MacKerell Jr, and R. W. Pastor. Update of the CHARMM all-atom additive force field for lipids: validation on six lipid types. *The Journal of Physical Chemistry B*, 114(23):7830–7843, 2010.

[54] J. M. V. A. Koelman and P. J. Hoogerbrugge. Dynamic simulations of hard-sphere suspensions under steady shear. *EPL (Europhysics Letters)*, 21(3):363–368, 1993.

[55] L. D. Landau, E. M. Lifshitz, A. M. Kosevich, and L. P. Pitaevski. *Theory of Elasticity.* Elsevier, New York, 3rd edition, 1986.

[56] J. Lee, X. Cheng, J. M. Swails, M. S. Yeom, P. K. Eastman, J. A. Lemkul, S. Wei, J. Buckner, J. C. Jeong, Y. Qi, et al. CHARMM-GUI input generator for NAMD, GROMACS, AMBER, OpenMM, and CHARMM/OpenMM simulations using the CHARMM36 additive force field. *Journal of Chemical Theory and Computation*, 12(1):405–413, 2015.

[57] K. Y. C. Lee. Collapse mechanisms of langmuir monolayers. *Annual Review of Physical Chemistry*, 59:771–791, 2008.

[58] E. Lindahl and O. Edholm. Mesoscopic undulations and thickness fluctuations in lipid bilayers from molecular dynamics simulations. *Biophysical Journal*, 79(1):426–433, 2000.

[59] R. Lipowsky and E. Sackmann. *Structure and dynamics of membranes: I. from cells to vesicles/II. generic and specific interactions.* Elsevier, Amsterdam, 1995.

[60] M. Lísal, J. K. Brennan, and W. R. Smith. Mesoscale simulation of polymer reaction equilibrium: Combining dissipative particle dynamics with reaction ensemble monte carlo. I. polydispersed polymer systems. *The Journal of Chemical Physics*, 125(16):164905, 2006.

[61] M. Lísal, J. K. Brennan, and W. R. Smith. Mesoscale simulation of polymer reaction equilibrium: Combining dissipative particle dynamics with reaction ensemble monte carlo. II. supramolecular diblock copolymers. *The Journal of Chemical Physics*, 130(10):104902, 2009.

[62] W. Lu, C. M. Knobler, R. F. Bruinsma, M. Twardos, and M. Dennin. Folding langmuir monolayers. *Physical Review Letters*, 89(14):146107, 2002.

[63] H. V. Ly and M. L. Longo. The influence of short-chain alcohols on interfacial tension, mechanical properties, area/molecule, and permeability of fluid lipid bilayers. *Biophysical Journal*, 87(2):1013–1033, 2004.

[64] A. D. Mackerell. Empirical force fields for biological macromolecules: overview and issues. *Journal of Computational Chemistry*, 25(13):1584–1604, 2004.

[65] A. D. MacKerell, M. Feig, and C. L. Brooks. Extending the treatment of backbone energetics in protein force fields: Limitations of gas-phase quantum mechanics in reproducing protein conformational distributions in molecular dynamics simulations. *Journal of Computational Chemistry*, 25(11):1400–1415, 2004.

[66] A. D. MacKerell Jr, D. Bashford, M. Bellott, R. L. Dunbrack Jr, J. D. Evanseck, M. J. Field, S. Fischer, J. Gao, H. Guo, S. Ha, et al. All-atom empirical potential for molecular modeling and dynamics studies of proteins. *The Journal of Physical Chemistry B*, 102(18):3586–3616, 1998.

[67] M. Müller, K. Katsov, and M. Schick. Biological and synthetic membranes: what can be learned from a coarse-grained description? *Physics Reports*, 434(5):113–176, 2006.

[68] K. M. Nakagawa and H. Noguchi. Morphological changes of amphiphilic molecular assemblies induced by chemical reactions. *Soft Matter*, 11(7):1403–1411, 2015.

[69] K. M. Nakagawa and H. Noguchi. Nonuniqueness of local stress of three-body potentials in molecular simulations. *Physical Review E*, 94(5):053304, 2016.

[70] K. M. Nakagawa and H. Noguchi. Bilayer sheet protrusions and budding from bilayer membranes induced by hydrolysis and condensation reactions. *Soft Matter*, DOI: 10.1039/C7SM02326J, 2018.

[71] Y. Nishizuka. The role of protein kinase C in cell surface signal transduction and tumour promotion. *Nature*, 308(5961):693–698, 1984.

[72] Y. Nishizuka. Intracellular signaling by hydrolysis of phospholipids and activation of protein kinase C. *Science*, 258(5082):607–615, 1992.

[73] H. Noguchi. Membrane simulation models from nanometer to micrometer scale. *Journal of the Physical Society of Japan*, 78(4):041007, 2009.

[74] H. Noguchi and G. Gompper. Dynamics of fluid vesicles in shear flow: Effect of membrane viscosity and thermal fluctuations. *Physical Review E*, 72(1):011901, 2005.

[75] H. Noguchi and G. Gompper. Meshless membrane model based on the moving least-squares method. *Physical Review E*, 73(2):021903, 2006.

[76] H. Noguchi and G. Gompper. Transport coefficients of dissipative particle dynamics with finite time step. *EPL (Europhysics Letters)*, 79(3):36002, 2007.

[77] H. Noguchi and M. Takasu. Fusion pathways of vesicles: a brownian dynamics simulation. *The Journal of Chemical Physics*, 115(20):9547–9551, 2001.

[78] H. Noguchi and M. Takasu. Self-assembly of amphiphiles into vesicles: a brownian dynamics simulation. *Physical Review E*, 64(4):041913, 2001.

[79] W. Noll. Die herleitung der grundgleichungen der thermomechanik der kontinua aus der statistischen mechanik. *Journal of Rational Mechanics and Analysis*, 4:627–646, 1955.

[80] F. Nomura, M. Nagata, T. Inaba, H. Hiramatsu, H. Hotani, and K. Takiguchi. Capabilities of liposomes for topological transformation. *Proceedings of the National Academy of Sciences of the United States of America*, 98(5):2340–2345, 2001.

[81] S. Ohnishi. *Dynamic structure of biomembranes*. University of Tokyo Press, Tokyo, 2nd edition, 1993.

[82] M. Orsi and J. W. Essex. The ELBA force field for coarse-grain modeling of lipid membranes. *PLoS One*, 6(12):e28637, 2011.

[83] M. Orsi, D. Y. Haubertin, W. E. Sanderson, and J. W. Essex. A quantitative coarse-grain model for lipid bilayers. *The Journal of Physical Chemistry B*, 112(3):802–815, 2008.

[84] S. Pall, M. J. Abraham, C. Kutzner, B. Hess, and E. Lindahl. Tackling exascale software challenges in molecular dynamics simulations with GROMACS. In *International Conference on Exascale Applications and Software*, pages 3–27. Springer, 2014.

[85] S. J. Pennycook, C. J. Hughes, M. Smelyanskiy, and S. A. Jarvis. Exploring simd for molecular dynamics, using Intel® Xeon® processors and Intel® Xeon Phi™ coprocessors. In *Parallel & Distributed Processing (IPDPS), 2013 IEEE 27th International Symposium on*, pages 1085–1097. IEEE, 2013.

[86] E. A. J. F. Peters. Elimination of time step effects in DPD. *EPL (Europhysics Letters)*, 66(3):311–317, 2004.

[87] B. Quentrec and C. Brot. New method for searching for neighbors in molecular dynamics computations. *Journal of Computational Physics*, 13(3):430–432, 1973.

[88] K. A. Riske and H.-G. Döbereiner. Diacylglycerol-rich domain formation in giant stearoyl-oleoyl phosphatidylcholine vesicles driven by phospholipase C activity. *Biophysical Journal*, 85(4):2351–2362, 2003.

[89] B. Różycki and R. Lipowsky. Spontaneous curvature of bilayer membranes from molecular simulations: Asymmetric lipid densities and asymmetric adsorption. *The Journal of Chemical Physics*, 142(5):054101, 2015.

[90] S. Safran. *Statistical thermodynamics on surfaces and interfaces*. Westview Press, Oxford, 2003.

[91] A. Sakashita, N. Urakami, P. Ziherl, and M. Imai. Three-dimensional analysis of lipid vesicle transformations. *Soft Matter*, 8(33):8569–8581, 2012.

[92] P. Schofield and J. R. Henderson. Statistical mechanics of inhomogeneous fluids. *Proceedings of the Royal Society of London A: Mathematical, Physical and Engineering Sciences*, 379(1776):231–246, 1982.

[93] U. Seifert. Configurations of fluid membranes and vesicles. *Advances in Physics*, 46(1):13–137, 1997.

[94] S. Semrau, T. Idema, L. Holtzer, T. Schmidt, and C. Storm. Accurate determination of elastic parameters for multicomponent membranes. *Physical Review Letters*, 100(8):088101, 2008.

[95] P. Sens. Dynamics of nonequilibrium membrane bud formation. *Physical Review Letters*, 93(10):108103, 2004.

[96] T. Shardlow. Splitting for dissipative particle dynamics. *SIAM Journal of Scientific Computing*, 24(4):1267–1282, 2003.

[97] M. P. Sheetz and S. J. Singer. Biological membranes as bilayer couples. a molecular mechanism of drug-erythrocyte interactions. *Proceedings of the National Academy of Sciences of the United States of America*, 71(11):4457–4461, 1974.

[98] J. C. Shelley, M. Y. Shelley, R. C. Reeder, S. Bandyopadhyay, and M. L. Klein. A coarse grain model for phospholipid simulations. *The Journal of Physical Chemistry B*, 105(19):4464–4470, 2001.

[99] H. Shiba and H. Noguchi. Estimation of the bending rigidity and spontaneous curvature of fluid membranes in simulations. *Physical Review E*, 84(3):031926, 2011.

[100] H. Shiba, H. Noguchi, and G. Gompper. Structure formation of surfactant membranes under shear flow. *The Journal of Chemical Physics*, 139(1):014702, 2013.

[101] J. C. Shillcock and R. Lipowsky. Equilibrium structure and lateral stress distribution of amphiphilic bilayers from dissipative particle dynamics simulations. *The Journal of Chemical Physics*, 117(10):5048–5061, 2002.

[102] J. C. Shillcock and R. Lipowsky. Tension-induced fusion of bilayer membranes and vesicles. *Nature Materials*, 4(3):225–228, 2005.

[103] W. Shinoda, T. Nakamura, and S. O. Nielsen. Free energy analysis of vesicle-to-bicelle transformation. *Soft Matter*, 7(19):9012–9020, 2011.

[104] S. A. Shkulipa, W. K. den Otter, and W. J. Briels. Surface viscosity, diffusion, and intermonolayer friction: simulating sheared amphiphilic bilayers. *Biophysical Journal*, 89(2):823–829, 2005.

[105] M. Sotomayor and K. Schulten. Molecular dynamics study of gating in the mechanosensitive channel of small conductance mscs. *Biophysical Journal*, 87(5):3050–3065, 2004.

[106] N. A. Spenley. Scaling laws for polymers in dissipative particle dynamics. *EPL (Europhysics Letters)*, 49(4):534–540, 2000.

[107] K. Suzuki, T. Toyota, K. Takakura, and T. Sugawara. Sparkling morphological changes and spontaneous movements of self-assemblies in water induced by chemical reactions. *Chemistry Letters*, 38(11):1010–1015, 2009.

[108] S. Takada, Z. Luthey-Schulten, and P. G. Wolynes. Folding dynamics with nonadditive forces: a simulation study of a designed helical protein and a random heteropolymer. *The Journal of Chemical Physics*, 110(23):11616–11629, 1999.

[109] R. H. Templer, S. J. Castle, A. R. Curran, G. Rumbles, and D. R. Klug. Sensing isothermal changes in the lateral pressure in model membranes using di-pyrenyl phosphatidylcholine. *Faraday Discussions*, 111:41–53, 1999.

[110] D. N. Theodorou and U. W. Suter. Shape of unperturbed linear polymers: polypropylene. *Macromolecules*, 18(6):1206–1214, 1985.

[111] B. D. Todd, D. J. Evans, and P. J. Daivis. Pressure tensor for inhomogeneous fluids. *Physical Review E*, 52(2):1627, 1995.

[112] A. Torres-Sánchez, J. M. Vanegas, and M. Arroyo. Examining the mechanical equilibrium of microscopic stresses in molecular simulations. *Physical Review Letters*, 114(25):258102, 2015.

[113] A. Torres-Sánchez, J. M. Vanegas, and M. Arroyo. Geometric derivation of the microscopic stress: A covariant central force decomposition. *Journal of the Mechanics and Physics of Solids*, 93:224–239, 2016.

[114] T. Toyota, K. Takakura, J. Kose, and T. Sugawara. Hierarchical dynamics in the morphological evolution from micelles to giant vesicles induced by hydrolysis of an amphiphile. *ChemPhysChem*, 7(7):1425–1427, 2006.

[115] M. Tuckerman, B. J. Berne, and G. J. Martyna. Reversible multiple time scale molecular dynamics. *The Journal of Chemical Physics*, 97(3):1990–2001, 1992.

[116] J. M. Vanegas and M. Arroyo. Force transduction and lipid binding in MscL: A continuum-molecular approach. *PLoS One*, 9(12):e113947, 2014.

[117] J. M. Vanegas, A. Torres-Sánchez, and M. Arroyo. Computing the local stress tensor in classical MD simulations. `http://www.lacan.upc.edu/LocalStressFromMD/`.

[118] J. M. Vanegas, A. Torres-Sánchez, and M. Arroyo. Importance of force decomposition for local stress calculations in biomembrane molecular simulations. *Journal of Chemical Theory and Computation*, 10(2):691–702, 2014.

[119] R. M. Venable, F. L. H. Brown, and R. W. Pastor. Mechanical properties of lipid bilayers from molecular dynamics simulation. *Chemistry and Physics of Lipids*, 192:60–74, 2015.

[120] M. Venturoli, M. M. Sperotto, M. Kranenburg, and B. Smit. Mesoscopic models of biological membranes. *Physics Reports*, 437(1):1–54, 2006.

[121] L. Verlet. Computer ”experiments” on classical fluids. I. thermodynamical properties of lennard-jones molecules. *Physical Review*, 159(1):98, 1967.

[122] D. C. Visser, H. C. J. Hoefsloot, and P. D. Iedema. Modelling multi-viscosity systems with dissipative particle dynamics. *Journal of Computational Physics*, 214(2):491–504, 2006.

[123] H. Watanabe, M. Suzuki, and N. Ito. Efficient implementations of molecular dynamics simulations for Lennard-Jones systems. *Progress of Theoretical Physics*, 126(2):203–235, 2011.

[124] M. Yanagisawa, M. Imai, and T. Taniguchi. Shape deformation of ternary vesicles coupled with phase separation. *Physical Review Letters*, 100(14):148102, 2008.

[125] P. Ziherl and S. Svetina. Nonaxisymmetric phospholipid vesicles: Rackets, boomerangs, and starfish. *EPL (Europhysics Letters)*, 70(5):690–696, 2005.

List of Publications

Refereed papers

- K. M. Nakagawa and H. Noguchi, *Bilayer sheet protrusions and budding from bilayer membranes induced by hydrolysis and condensation reactions* (Main results are included in Chapter 3. Reproduced with permission from the Royal Society of Chemistry.)

- K. M. Nakagawa and H. Noguchi, *Nonuniqueness of local stress of three-body potentials in molecular simulations* Physical Review E 94, 053304/1–11 (2016). (Main results are included in Chapter 4. Copyright (2016) by the American Physical Society.)

Acknowledgments

I would like to thank my supervisor Prof. Hiroshi Noguchi for his invaluable support and comments on my dissertation work. He has a deep insight into the physics of biomembrane and coarse-grained simulation techniques and gave me comments on simulation results. Without his support, my dissertation work cannot be achieved.

I also would like to thank Prof. Hayato Shiba for his kind advice for developing simulation codes. He has much experience in numerical calculations and advised me basic implementations of molecular dynamics simulation code.

I would like to express my gratitude to Prof. Hiroshi Watanabe for comments on the acceleration technique of molecular dynamics simulation. I learned the parallelization techniques of molecular dynamics simulation code from his open source code. Additionally, his excellent lectures in the program developing and debugging helped me to implement the readable, maintainable, and bugless code.

Furthermore, I am grateful to Prof. Yuji Higuchi for the comments for manuscripts. His constructive and critical comments on my dissertation works were helpful.

I thank all the current and former members of Noguchi lab. I could not list up all the people whom I would like to thank. I was pleased in Noguchi lab for five years.

Finally, I appreciate my family from physical and mental aspects.